BEst (Biomarker Estimation): Health Biomarker Estimation Non-invasively and Ubiquitously

Md Kamrul Hasan
Marquette University

BEst (Biomarker Estimation):
Health Biomarker Estimation Non-invasively and Ubiquitously

by
Md Kamrul Hasan

A Dissertation Submitted to the Faculty of the Graduate School,
Marquette University,
in Partial Fulfillment of the Requirements for
the Degree of Doctor of Philosophy

Milwaukee, Wisconsin
May, 2019

ABSTRACT
BEst (Biomarker Estimation):
Health Biomarker Estimation Non-invasively and Ubiquitously

Md Kamrul Hasan, B.S., M.S.

Marquette University, 2019

This dissertation focuses on the non-invasive assessment of blood-hemoglobin levels. The primary goal of this research is to investigate a reliable, affordable, and user-friendly point-of-care solution for hemoglobin-level determination using fingertip videos captured by a smartphone. I evaluated videos obtained from five patient groups, three from the United States and two from Bangladesh, under two sets of lighting conditions. In the last group, based on human tissue optical transmission modeling data, I used near-infrared light-emitting diode sources of three wavelengths. I developed novel image processing techniques for fingertip video analysis to estimate hemoglobin levels. I studied video images creating image histogram and subdividing each image into multiple blocks. I determined the region of interest in a video and created photoplethysmogram signals. I created features from image histograms and PPG signals. I used the Partial Least Squares Regression and Support Vector Machine Regression tools to analyze input features and to build hemoglobin prediction models. Using data from the last and largest group of patients studied, I was able to develop a model with a strong linear correlation between estimated and clinically-measured hemoglobin levels. With further data and methodological refinements, the approach I have developed may be able to define a clinically accurate public health applicable tool for hemoglobin level and other blood constituent assessment.

ACKNOWLEDGMENTS

Md Kamrul Hasan, B.S., M.S.

I would express my gratitude and thank my supervisor Dr. Sheikh Iqbal Ahamed for his continuous support, encouragement, and guidance for my work. I also thank Dr. Richard Love, Dr. Young L. Kim, Dr. Gary Krenz, Dr. Henry Medeiros, and Dr. M Munirul Haque for taking their valuable time for serving as committee members. I am grateful to Dr. Richard Love for his continual inspiration and brilliant ideas to solve health care problems. His critical thinking about the protocol design, working principle, and clinical methodologies helped me to keep the focus on my research work. His passion for building a low-cost, reliable, and portable solution for people encouraged me to work in the healthcare area. I also want to thank Dr. Young L. Kim for his excellent guidelines from the biomedical perspective. From his supervision, I learned several things including how to do research considering biological foundation and solve a problem scientifically. His focus on scientific literature and critical analysis regarding the validity of the approach helped me to study this research and lead me to the next steps. I firmly believe that these explicit guidelines helped me significantly to build a low-cost smartphone-based point-of-care tool. I want to express my gratitude to Dr. Gary Krenz for his invaluable help and mentorship which allowed me to explore the domain knowledge in the mathematical and computational sciences area. I learned about many things from Dr. Krenz on how to do research and present a solution scientifically. Special thanks to Dr. Henry Medeiros and Dr. M Munirul Haque for their forward direction with a deep understanding of image processing, machine learning, and mobile health application design. I want to thank Dr. MMA Hashem, Professor of Khulna University of Engineering and Technology (KUET), Bangladesh for his constant support in the implementation of the data collection protocol and tools development. I would also take the opportunity to thank Dr. Joshua Field, Dr. Stephen Hargarten, and Reza

Salim for their consistent support in the data collection process. I also like to thank our senior graduate students Mohammad Adibuzzaman, Duc Do, Regis Rutarindwa, and GM Tanim, and friends Masabho Milali, Manzur Rahman, Nazmus Sakib, and Hasan Aziz for supporting me in every possible way. And last but not least, I thank my wife, daughter, parents, and lab colleagues for their unconditional help.

TABLE OF CONTENTS

LIST OF TABLES

LIST OF FIGURES

Chapter 1

Introduction

Hemoglobin (Hb) related diseases are a major global public health problem [1]. Hb is the principal constituent in red blood cells that carry oxygen to body tissues. The commonest hemoglobin diseases are anemia consequent to blood loss and inadequate red cell production. Approximately 25% of the global population [2] and 5.6% of the US population are anemic [3]. Anemia enhances the risk of cognitive development impairment in children and increases the mortality rate in pregnant women. Most people suffering from anemia live in developing countries where clinical Hb diagnosis capacities are limited. Another common hemoglobin disorder is sickle cell disease (SCD). Individuals with SCD have abnormal sickle-shaped red blood cells, the fraction of which increases under stress and causes acute and severe musculoskeletal pain. In the United States, SCD disproportionately affects the minority populations. According to the Centers for Disease Control and Prevention (CDC), about 100,000 African Americans and Latinos have SCD in the US [4].

1.1 Hemoglobin Assessment Tools

The need for hemoglobin level assessment in about 2 billion anemic people worldwide puts significant pressure on blood diagnostic processes. The current clinical diagnostic method for hemoglobin measurement is a clinical laboratory analysis of a blood sample, which is subject to affordability and reliability constraints in many settings. The most common way to assess hematologic disease is a laboratory plasma hemoglobin test, which measures the concentration of hemoglobin in the blood. In these tests, the patients provide venous or capillary blood specimens. Drawing blood from a vein involves insertion of a needle associated with which patients may feel discomfort, pain, numbness, or a shocking sensation, and afterwards itching or burning at the collection

site. These procedures are often traumatic for children and mentally disabled persons. Additionally, patients require travel to a medical facility which can be time-consuming and involve some expense. A non-invasive, easy-to-use measure of hemoglobin level could facilitate the safe management of patients with anemia and SCD at home and revolutionize their care.

There are some commercial non-invasive point-of-care (POC) tools for hemoglobin assessment. In Figure 1.1, we present a number of recent non-invasive solutions for estimating hemoglobin levels where different data collection (add-on) devices are used. In addition, several commercial non-invasive POC tools are available for hemoglobin (Hb) measurement (Figure 1.2). Most of these solutions suffer from one or more of the following limitations: 1) challenging data collection processes; 2) complex data analysis and feature extraction processes; 3) affordability and portability; and 4) lack of user-friendliness and costly external modules [5]. In sum, commonly used technologies for hemoglobin measurement are costly, uncomfortable, and inconvenient. Since current smartphones have high-resolution cameras, light-emitting diode (LED) white lights, infrared sensors, and computing abilities, smartphones might be used for such vital health parameter monitoring. By 2020, the number of smartphone users in the world is expected to be 2.9 billion. Considering the urgent clinical needs in low and middle-income countries, a smartphone-based solution would be a beneficial technology for non-invasive Hb assessment.

1.2 Dissertation Focus

Recently, smartphone-based non-invasive solutions have been considered for Hb level assessment. Some of these technologies use images of the lower eyelid because of the visibility of conjunctival mucosa and underlying micro-vessels. Eyelid-based images, as well as a color chart, are used together to calculate the hemoglobin level. Estimation of hemoglobin levels with these systems is presently unreliable. A nonin-

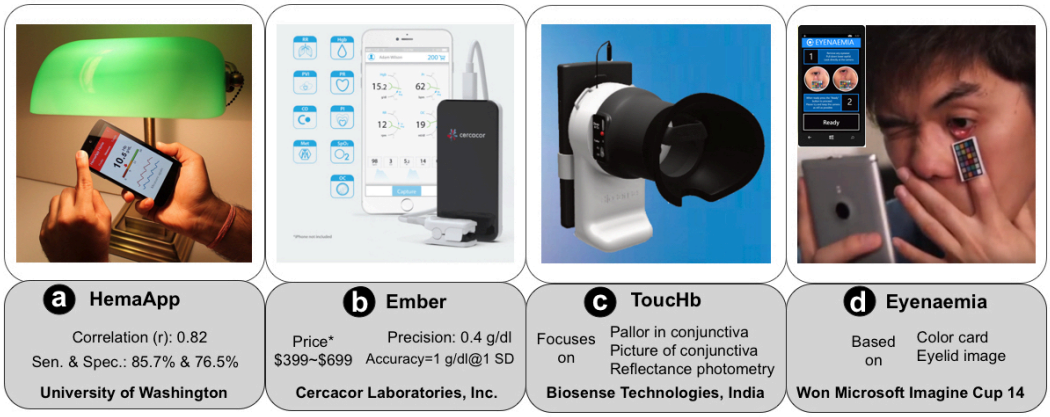

Figure 1.1: Smartphone-based POC tools for non-invasive hemoglobin measurement. a) HemaApp [6], b) Ember [7], c) TouchHB [8], and d) Eyenaemia [9]. The images are from respective references. *denotes the system's approximte price.

Figure 1.2: Commercial POC tools for non-invasive hemoglobin measurement. a) Smart-Hb [10], b) Masimo SpHb [11], c) NBM 200 [12], and d) Astrim-Fit [13]. The images are from respective references. *denotes the system's approximte price.

vasive, easy-to-use, inexpensive measure of hemoglobin levels is desirable to enhance access to hemoglobin measurement and to manage patients with hematologic diseases efficiently. A smartphone-based hemoglobin estimation tool may also measure critical physiologic data to provide a "snapshot" of the condition of a patient with a hemoglobin disorder at home.

The data in this dissertation suggest that smartphone-based fingertip videos captured under near-infrared light, together with image processing techniques and machine learning algorithms, can estimate blood hemoglobin levels non-invasively with near

clinically acceptable accuracy. We employ video-image processing towards the generation of time-series information, high-quality photoplethysmogram (PPG) signals with features that can be trained and optimized on large scale fingertip videos. This approach has several advantages. A smartphone-camera can capture a fingertip video under low-cost near-infrared (NIR) LED lights which eleminates need for additional POC tools enhances affordability. We have developed a POC solution to estimate hemoglobin levels non-invasively using widely-available devices.

In the first clinical study (Chapter 3 of this dissertation), we investigated the variation of image pixel intensities. We showed that the histogram shape and values of red, green, and blue (RGB) color pixel intensities correlate highly with hemoglobin levels. To create an adequately accurate clinical hemoglobin level estimation model, we explored the biologically motivated foundations for a non-invasive hemoglobin measurement system, improved the data collection protocol, introduced novel image processing techniques, generated PPG features of fingertip videos, and then employed Support Vector Machine Regression (SVR) to the feature vectors of selected subjects to build a non-invasive hemoglobin level estimation model. Blood hemoglobin and plasma responses are implicitly captured in PPG features, which allow us to build the estimation model. Regression algorithms open opportunities for the development of prediction models, that can adapt to a new user's fingertip videos and, update the model from their PPG features. Finally, the fingertip video recording and the feedback process can be optimized by uploading the video to a cloud server automatically. Prediction model significantly outperforms previously reported work using smartphones to measure Hb. We believe our smartphone-based solution will lead to the development of a useful non-invasive hemoglobin estimation process as well as to new opportunities for remote health monitoring.

1.3 Fingertip Anatomy

A smartphone camera can capture data from different body sites. As a body site of investigation, fingertip [6], nailbed [14], eye conjunctiva (i.e., eyelid) [15], tongue [16], and palm [17] have been studied in seeking to build an affordable non-invasive solution for hemoglobin assessment. Among body sites, the fingertip has several advantages. Fingertips are is easily accessible, less sensitive to minor manipulations, and generally easy to control. In Figure 1.3, the different parts of a finger are considered. The approximate thickness of a fingernail of the average adult male is 1 millimeter (mm); the epidermis is 1.5 mm; the dermis is 3 mm; the finger bone is 6 mm; and the total thickness from the dorsal to the ventral pad side of a finger is about 14 mm. The fingernail is comprised of a hard protein called keratin, which is translucent [18]. Based on these characteristics and light responses from the fingertip, we surmised that it would be possible to use fingertip-videos in developing a non-invasive solution for hemoglobin level assessment.

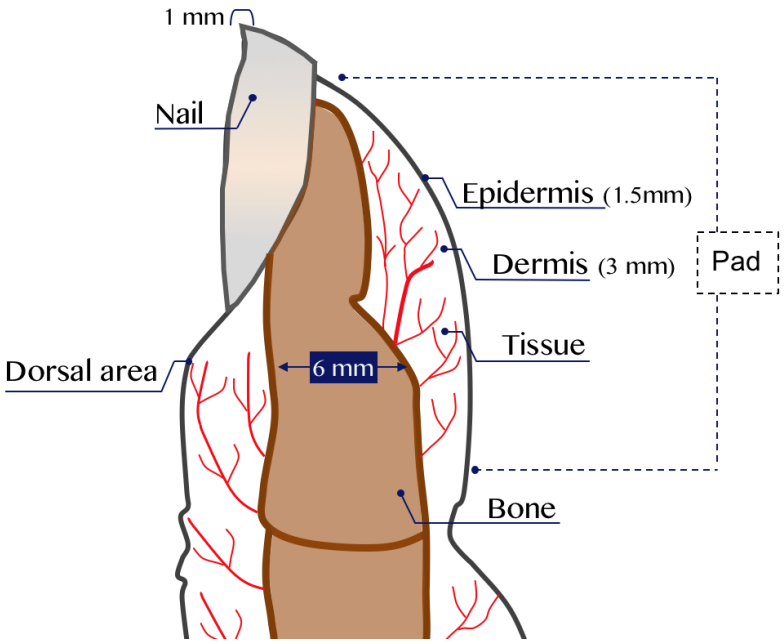

Figure 1.3: Different parts of the finger and their thickness.

1.4 Light Response in Living Tissues

The smartphone flashlight (camera light) or an external light source can be used to illuminate tissue and the smartphone camera can be used as a photodetector. Whether illuminated via reflective or transmissive modes, light does not propagate directly in living tissues. In tissues, light is scattered and absorbed by cells or different molecules. The absorption occurs with hemoglobin and other chromophores. Scattering is found in tissues with a refractive index of the aqueous-lipid membrane interfaces of cells [19]. Light photons transmit in three different ways through living tissue media and generate three paths. The first path is called ballistic, where photons traverse directly over a short time. The second one is snake, where photons move indirectly in forward scattering. The last one is called diffuse, where each photon travels a long path since it experiences many scattering processes (Figure 1.4(a)). In the near-infrared (NIR) range, the scattering cross-section of biological tissue is small. Thus, the diffused scattered light can penetrate from 10mm to 20mm or more. Since NIR light has a penetration depth of 5-6 cm in living tissues, we can receive the response of a NIR light (sent through the dorsal side of a finger) from the pad or ventral side of the finger (Figure 1.3) [20, 21]. In the reflective mode, photons are coming from a light source, and a photodetector captures the reflected light (Figure 1.4(b)). Smartphone-captured video of illuminated tissue, such as a fingertip, result in photoplethysmography (PPG) signals which can be examined for clinically relevant physiological parameter.

1.5 Photoplethysmography (PPG)

Photoplethysmography is an optical technique which can be used to determine blood volume changes non-invasively. This optical technique is cost-effective and straightforward in observing blood volume changes in the microvascular beds of tissues [22]. A PPG system requires a light source and a photodetector where the light source illumi-

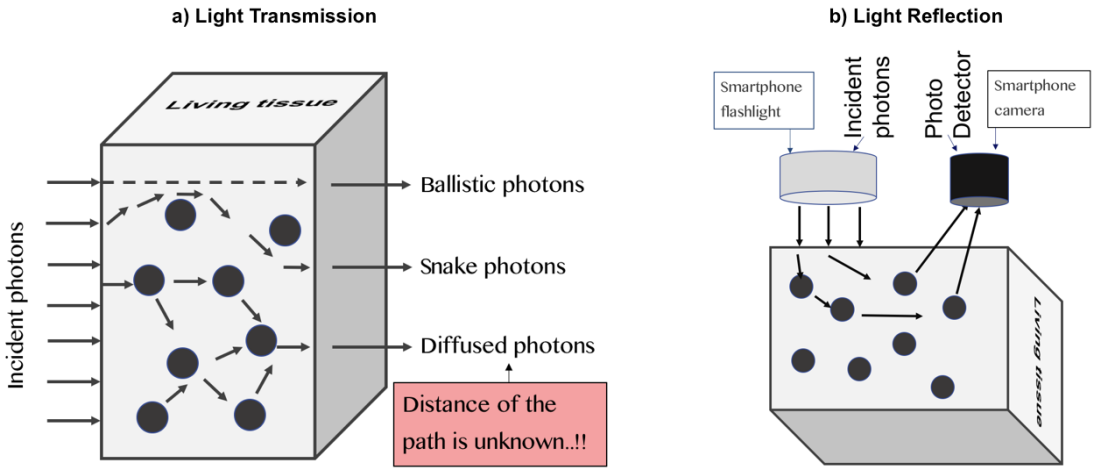

Figure 1.4: Light transmission processes in living tissues. a) There are three types of transmissive light paths: ballistic, snake, and diffused scattered light. b) Reflective light transmission in living tissues.

nates the tissue area (e.g., finger), and the photodetector captures the variations of light intensity. The intensity variations are seen because of the pulsatile action of the heart. So, the PPG signal represents the difference of light intensity that changes with the peripheral pulse (synchronized to heartbeat). PPG signals are typically acquired using one of two illumination modes: transmission or reflection. In the transmission mode, PPG sensors are attached on the body site where the body part is thin (e.g., fingertip, earlobe, etc.). On the other hand, reflection PPG can be used on any location of a body site [23].

1.6 AC and DC Component

The principles of photoplethysmography have been described in several studies [24, 25, 26]. Light penetration (absorbance) through living tissues depends on their various components-skin pigments, bone, and arterial and venous blood. Changes in PPG signals due to blood flow are seen in arteries and arterioles. Since the systolic phase of the cardiac cycle creates blood volume changes in the arteries, PPG sensors can detect these changes. This signal is captured by calculating the blood flow volume changes from the detected light intensities which are reflected or transmitted from the tissues.

A photoplethysmogram (PPG) waveform has two main components. First, the direct current (DC) which is generated by the transmitted or reflected signal from the tissues and the average blood volume of both arterial and venous blood, as presented in Figure 1.5. These components are stable since the DC component does not change significantly with respiration. The second part is the alternating current (AC), which changes with blood volume changes associated with cardiac systole and diastole [26]. A finger has arterial and venous blood as the light absorbing components. As an example of a PPG-based system, a pulse oximeter isolates the signals coming from arterial and venous blood and takes the absorption ratio of different lighting sources to calculate the oxygen saturation in the blood.

In arterial blood, the dynamic time changing component of the fingertip video of the signal will be denoted as an AC signal and the static part will be denoted as a DC signal, as shown in Figure 1.5. The DC component of a PPG signal relates to the average blood content in the tissue between two heartbeats.

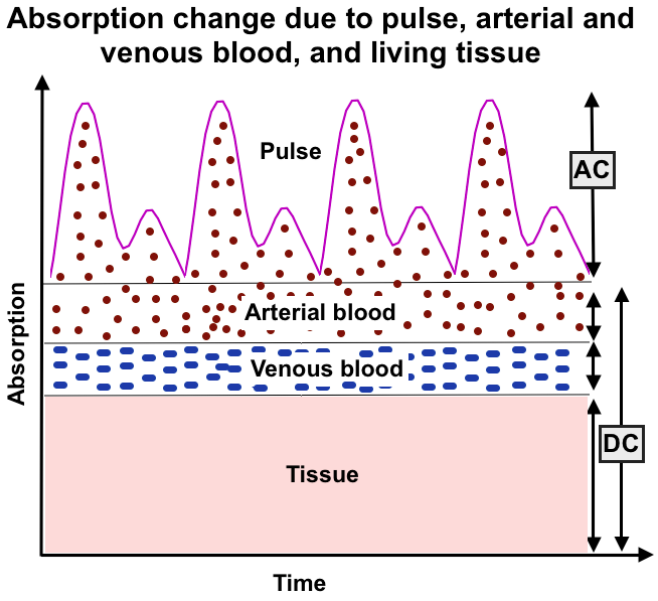

Figure 1.5: A PPG signal is generated from a finger (living tissue). "Arterial blood" denotes the portion of the PPG that is due to the average arterial blood volume. "Venous blood" denotes a portion of the PPG that is due to the average venous blood volume.

In tissue, absorbed light is modulated by the change in arterial blood volume due to the contraction of the heart. Figure 1.5 is a plot of the PPG intensity calculated for one light source over time or across video frames. When the heart pumps, and more blood is present in the body tissue during systolic phase and more light will be absorbed, which means that less light will be received by a smartphone camera. Likewise in the diastolic phase, less blood present in the tissue, less light is absorbed and a smartphone camera captures a higher level of light intensity. The relative magnitude of the fluctuating signal, which is presented as the AC signal in Figure 1.5 of the PPG waveform, is formed by the increased amount of blood in systolic phase and the decreased amount of blood in the diastolic phase of the cardiac cycle. In Figure 1.5, the AC and DC magnitudes are inverted to present as a standard PPG signal. Based on the light source used to illuminate a finger, the magnitude of AC and DC is changed.

1.7 Critical Physiology and Biology of Hemoglobin

The blood volume, blood vessel wall movement and the orientation of red blood cells (RBC) can influence light absorbance captured by a photodetector [27]. Since blood absorbs more light than tissue, a change in the blood volume can be calculated using the intensity of the increased (absorbed) light. Green light is commonly used for blood flow measurement in the skin and green-yellow region (500-600nm) of the visible spectrum can capture the more in-depth response from the pulsatile blood [26]. If we use IR or near-IR wavelengths, then we can estimate the blood flow in deep-tissues, such as fingers and muscles

A pulse oximeter measures the relative concentration of oxyhemoglobin level, but it cannot measure the absolute hemoglobin concentration due to the effective path length of light (the distance occupied by arterial blood). Studies have shown that the response from tissue and venous blood are quite stable (no pulsation), also known as the DC component of a PPG. Only arterial blood causes pulsation, the AC component, of a

PPG signal. If we record the pulsatile changes (arterial) by illuminating a finger under two different wavelengths of NIR lights and find the ratio between two PPGs' features (responses), then we can build a non-invasive POC tool.

A pulse oximeter uses a photodetector for photoplethysmogram (PPG) generation, but the charge-coupled device (CCD) camera sensors can capture signals in a NIR range where the light wavelength is around 1000nm [28]. Modern smartphone cameras have strong sensing capabilities for PPG imaging [29]. In our smartphone-based PPG system, a finger covers the smartphone camera lens without additional pressure and the volumetric changes in arterial blood can be captured calculating the light absorption. Since the video captures frames continuously, a continuous PPG signal can be calculated from the video frame. PPG signal can be created in visible to near infrared region because water in tissue absorbs ultraviolet (UV) light as well as the longer infrared wavelengths (close to 1000 nm). Skin melanin and fat have significant responses with the shorter wavelengths of light [30]. Light with a wavelength less than 650 nm is absorbed by hemoglobin, whereas the light absorption by oxyhemoglobin and deoxyhemoglobin has an isosbestic wavelength in this region [31]. Since water has a significant response around 1000 nm wavelength of light, plasma response can be detected in this NIR light range because the amount of water in plasma is 93% (Figure 1.6).

1.8 Research Questions

This dissertation presents smartphone-video-based non-invasive blood hemoglobin assessment techniques. The approach involves smartphone-based measurement of blood hemoglobin content using two optical absorption signals captured under infrared lights during blood volume changes. The blood volume changes are obtained with the PPG signal generated using the infrared lights. This research includes fingertip video recording-protocol design and the development of a hemoglobin prediction model. The main research question in this dissertation is: Is it possible to build a reliable and affordable

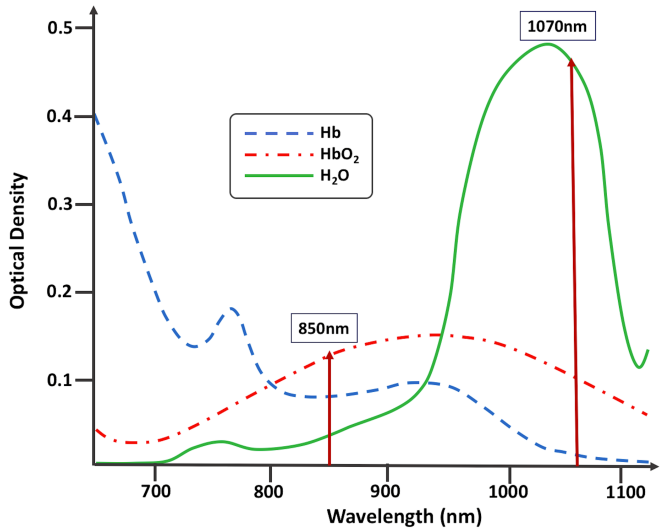

Figure 1.6: NIR response of blood oxygenated, deoxygenated hemoglobin, and plasma in living tissue. The image is redrawn from [32].

non-invasive POC tool for blood hemoglobin levels estimation? To answer this question, we considered the following:

1. How can we obtain a hemoglobin response from a smartphone-captured video of a body site?

2. What is the relationship between image pixel intensities and clinically measured hemoglobin levels?

3. How can we process a fingertip video to extract features and to build a prediction model?

Considering these initial research questions, we investigated the following:

- Design of a data collection protocol to record a fingertip video using a smartphone

- Exploration of the relationship between pixel intensities of a fingertip video image and gold standard laboratory hemoglobin levels

- Development of image processing techniques to analyze fingertip videos and build a prediction model for hemoglobin assessment

1.9 Dissertation Organization

We first present a review of currently published literature on smartphone-based diagnostic tools, image-based hemoglobin level estimation processes, photoplethysmogram-based hemoglobin measurement solutions, spectra-based applications, sensors, signal processing techniques, machine learning algorithms, and a brief summary of error measurement methods in Chapter 2. In Chapter 3, we give a detailed description of the protocol for first clinical study in four populations and the details of these populations. In Chapter 4, we show the analysis of data from the first clinical study for red, green, and blue pixel intensities, and histograms. We present further analyses of data from the first clinical study seeking to identify an optimal region of interest in the video images in Chapter 5. We describe the protocol for a second clinical study and details of this study population in Chapter 6. Photoplethysmogram analysis of data from the second clinical study to build a non-invasive hemoglobin prediction model is illustrated in Chapter 7. In Chapter 8, we describe our principal findings, the limitations of our methods, next steps with this work, and our concept of a framework for assessments of blood constituents generally.

Chapter 2

Review of Current Published Literature

In this chapter, we provide an overview of current published literature relevant to noninvasive hemoglobin level assessment. Literature about non-invasive hemoglobin measurement processes, mathematical tools, sensors, and machine learning algorithms are also considered here. Similar reported work related to specific contributions is discussed in each chapter.

2.1 Smartphone-based Techniques

The smartphone is a portable, affordable, and convenient platform for developing POC tools. More than 50% of cellular phones sold today are smartphones. At least one-third of the world's population (about 2.6 billion) owns a smartphone. Smartphones are ubiquitous devices and are increasingly being employed in research as tools in many areas including physiological parameter estimation [33, 34], medical diagnosis [35, 36, 37], and other research fields [38].

Table 2.1 presents a number of biomedical applications where a smartphone and camera plays a key role in the assessments of blood oxygenation, and hemoglobin, glucose, cholesterol, and antibody levels. In these applications, the most frequently used smartphones are from Apple, Samsung, Motorola, Google, HTC, Sony, and Asus where the camera sensor is used to capture videos or images. The accuracy level is presented as reliable in most of these studies, as shown in Table 2.1. We chose a Google Nexus 4 smartphone for our data collection processes in the first clinical study in 2014 based on the portability, camera sensor, computing power, battery hours, display size, and availability.

Optical responses captured by smartphones under multiple wavelengths of light

Table 2.1: Tabular summary of published literature on smartphone-based diagnostic tools.

Reference	Purpose	Smartphone	Data	Result
Peng et al. [34]		HTC S510e		R>0.7
Wang et al. [37]		Nexus 6p		R^2=0.62
Soni et al. [39]		Samsung Galaxy		R=0.94
Scully et al. [40]		Motorola Droid		R=92.2±5.3
Anggraeni et al.[41]		Asus Zenfone 2		R^2=0.81
Singhal et al. [42]		Sony Xperia		R^2=0.98
Dantu et al. [43]		HTC One X		P-value=0.005
Wu et al. [44]		iPhone 4		R^2=0.99
Devadhasan et al. [45]		Samsung		R^2=0.97
Oncescu et al. [46]		iPhone		E<5.5%
Zhu et al. [47]		Samsung Galaxy		R^2=0.92, E<5%

R=Correlation coefficients, E=Relative Error

=Heart rate, =Video, =Glucose, =Hemoglobin

=Respiratory rate, =SpO_2, =Cholesterol, =Red/white blood cells

have been used to build non-invasive hemoglobin prediction models. Wang et al. developed HemaApp, a smartphone-based mobile application, to non-invasively measure hemoglobin levels [6]. Users put their finger on the camera lens, where the fingertip was illuminated by three different wavelengths of light. HemaApp was run on a Nexus 5 smartphone and each light source remained active for 15 seconds continuously. The investigators extracted pixel values of each video frame and calculated the peak and valley heights of signals for each light source. They used a high pass filter to remove fluctuations due to breathing, applied a Fast Fourier Transform (FFT) on the filtered waveform to get the dominant peak, and applied Support Vector Machine Regression (SVR) to train a prediction model. Their prediction model showed 0.82 rank order correlation with gold standard hemoglobin levels and had sensitivity and precision of 85.7% and 76.5% respectively. The system was tested on a small population, and the linear correlation between estimated and gold standard hemoglobin must be judged low.

Edwards et al. developed a spectrometer that attaches to a smartphone [48]. The spectrometer operates in the wavelength ranges from visible to near-infrared using G-Fresnel.

For their smartphone-based spectrometer resolution was approximately 5 nm, where the wavelength range was selected from 400 nm to 1000 nm. These investigators studied tissue phantoms to measure the performance of the mobile spectrometer. They used 16 different Hb levels and took data in the wavelength range from 430 nm to 630nm. The absorption error was 9.2%, and the error for reduced scattering coefficients was 8.1%. The limitation of this study is that they did not apply their method to estimate hemoglobin levels.

Bui et al. developed a smartphone-based application called PhO2 for blood oxygenation level measurement [5]. These investigators evaluated the performance of PhO2 by collecting data from six subjects using a customized filter as an add-on. The add-on produced two light beams from a single light source (a flashlight) where the first beam's wavelength was selected from the range 670 nm to 690nm. The second beam's wavelength was chosen between 700nm and 779nm. Under these light sources, they captured fingertip videos using multiple smartphone cameras and high-quality PPG signals. They calculated the ratio (R_{red}) of AC and DC signal captured under red light and the ratio (R_{nir}) of AC and DC signal captured under NIR light. Calculating the ratio of R_{red} and R_{nir}, they generated features that were fed into a regression-based optimization model to estimate the SpO2 (peripheral capillary oxygen saturation) level. They evaluated the performance of PhO2: PhO2 estimated the oxygen saturation within 3.5% error rate, with 80% of confidence compared to FDA-approved pulse oximetry standards. The PhO2 system has limitations including long initialization time, region of interest (ROI) approximation, pressure measurement, and SpO2 measurement accuracy. In this small study, they did not include a wide range of smartphone devices.

2.2 Histogram-based Image Processing

Image-based blood-research is the focus of many blood constituent assessment efforts, but most processing techniques remain complex to implement and unable to manage large size images. To accelerate image processing, histogram-based image processing has become popular since it is straightforward, and easy to implement and understand.

Previous studies present histogram-based solutions to assess hemoglobin levels. For instance, Kim et al. introduced the LED and CMOS image sensor-based hemoglobin level assessment technique where a commercial RGB LED light was used to illuminate a cuvette which contained a blood specimen [49]. A CMOS image sensor captured images of specimens containing different hemoglobin levels. The region of interest (ROI) of each image was studied, generating a histogram of the ROI area. Their research used color pixel information with changes in color intensity captured by a CMOS image sensor. In their study, they measured hemoglobin concentration from an invasively obtained liquid blood samples. We believe, however, that a non-invasive solution for hemoglobin assessment from a living tissue is needed where light does not follow the Beer-Lambert law.

Ishihara et al. considered a region containing a blood vessel present in a living body. They used an external light source and captured the reflected light from the detection region using a CCD image sensor [50]. A histogram of frequency of pixel intensities of a predetermined region was calculated, where the lower and the higher intensity values were used as the light intensity of blood and tissue respectively for developing an apparatus to measure the concentration of hemoglobin. In their study, light intensity of body tissue and light intensity of blood were detected by analyzing the captured image, and a ratio of the light intensity of the body tissue with respect to the light intensity of blood was calculated for hemoglobin concentration estimation.

Rice et al. used a retinal image to estimate hemoglobin concentration. They applied histogram values to identify the rate of change in local intensity and applied these values as inputs to an artificial neural network [51]. Histogram-based approaches have also sought to facilitate the implementation of blood flow monitoring [52, 53] and to demonstrate heterogeneous morphologic features of tumor vascularity [54]. Our first image analysis process builds upon this idea by calculating a histogram value and extracting image frames from a video captured using a smartphone.

2.3 Spectra-based Non-invasive Systems

Spectroscopy techniques with near-infrared spectroscopy (NIRS) have received considerable attention for the non-invasive measurement of blood hemoglobin, oxygenation, pH, hematocrit, and glucose levels. Here, we discuss several spectra-based hemoglobin measurement techniques to investigate wavelength values and the response at those wavelengths from blood constituents, including hemoglobin and plasma.

Features extracted from multiple wavelengths of light have been employed to estimate blood hemoglobin levels. For example, Edwards et al. developed a non-invasive method of measuring hemoglobin flow through an organ by NIRS [20]. They monitored variations in the absorption of near-infrared light in the organ and calculated the changes in deoxyhemoglobin and oxyhemoglobin concentrations. They used laser diodes at six wavelengths 797.5, 802.5, 831.2, 848.7, 866.5, and 907.8 nm in their data collection. They applied NIR lights to capture the spectral response to estimate hemoglobin flow in the forearms of six healthy young adults. Finally, they calculated forearm blood flow by venous occlusion plethysmography using least-squares linear regression. The linear correlation between the calculated by NIRS and plethysmography was excellent with R^2=0.95. However, the number of observations in their study was only six.

Xiaoqing et al. also applied spectroscopy methods for non-invasive hemoglobin (Hb) measurement using eight laser diodes (wavelength range from 600 nm to 1100

nm) to record photoplethysmogram signals in 220 subjects [55]. They extracted dynamic spectrum from the pulsatile arterial blood using photoplethysmography (PPG) to enhance the signal-to-noise ratio (SNR) of measuring instruments and to remove the influences of individual differences. Using a machine calibration model, they observed R=0.86 and RMSE=8.48 g/L. However, their instrument set up was not portable or affordable for the noninvasive measurement of hemoglobin.

Hennig et al. developed a non-invasive fluorescence-based method that can determine iron status in the microcirculation of the lower lip [56]. In this study, they did the tissue fluorescence measurements using dual-wavelength excitation. They superimposed light from two laser diodes emitting at 407 nm and 425 nm, respectively, into a single optical fiber for fluorophore excitation to quantitatively extract the zinc protoporphyrin fluorescence. An optical fiber probe was placed on the lower lip for data collection and the generated fluorescence was measured by a spectrometer. The 425 nm wavelength was selected to measure fluorescence from red blood cell zinc protoporphyrin and a second wavelength, 407 nm, was selected to get additional fluorescence spectra to quantitatively extract the zinc protoporphyrin. They collected data from 56 women who recently delivered babies, where 35 women out of 56 were known to be iron-deficient. The result showed that the sensitivity and specificity of optical noninvasive detection of iron deficiency were 97% and 90%, respectively.

Table 2.2 presents other spectra-based hemoglobin level measurement processes where a different range of wavelength, input signal, and acquisition devices are listed. In most cases, investigators used an expensive spectrometer during the data collection processes. Analyzing the spectra-based studies (Table 2.2), we observe that the most commonly used spectral wavelengths were 850nm, 940nm, and 1070nm for noninvasive hemoglobin level assessment. Investigators also employed specialized devices to captured PPG signals from the data collection site (e.g., finger, hand, and earlobe). In the work reported here, we used regular smartphone devices for the fingertip video

recording to generate PPG signals.

Table 2.2: Summary of spectra-based techniques proposed for non-invasive hemoglobin measurement

Reference	**WL (nm)**	**Compared with**	**Signal**	**#Sub**
Nirupa [57]	624, 850	Prototype	IR PPG	69
Ding et al. [58]	600-1050	LED & Photodiode	Spectra	119
Bremmer et al. [59]	350-1050	Ocean Optics DH-2000	Spectra	8
Timm et al. [60]	600-1000	LED	PPG	48
Fuksis et al. [61]	760-940	IR LEDS	Spectra	-
Pothisarn et al. [62]	660, 940	Analyzer oximetry	Light	-
Nguyen et al. [63]	940	Radical 7, XE-2100	Pulse	41
Timm et al. [64]	600-1400	OxyTrue Hb	Spectra	1008
Wang et al. [65]	500-700, 1300	Masimo Pronto 7, RGB CMOS camera	PPG	32
Rochmanto et al. [66]	670, 940	Sysmex-KN21	PPG	78
Desai et al. [67]	530	Pronto-7, HemoCue Hematology analyzer	PPG	10

WL=Wavelength, #Sub=Number of subject, -=Not given

2.4 Sensors

Optical sensors are photometric devices that capture the optical signal from an external source where the source can be an LED, laser, or lights of different spectra [68]. Photodiodes are primarily used as optical sensors and are made of InGaAs and Indium-phosphor. Sometimes optical sensors contain an embedded amplifier that can select different wavelengths (500nm-1600nm) of the signal. We discuss several sensors that are commonly used for PPG signal generation including CMOS, CCD, InGaAs sensor, and a specialized PPG sensor.

CMOS sensor

Complementary Metal Oxide Semiconductor (CMOS) converts photons to electrons for digital processing. In general, CMOS sensors are used in smartphone, digital video, and

digital CCTV cameras. CMOS-based sensors also found in astronomical telescopes, scanners and barcode readers, robots, and optical character recognition (OCR) systems. CMOS chips have photolithography-light-capturing cells that pick up the photons at different wavelengths and translate them into electrons. A digital-to-analog converter changes the electrons into pixels of various colors. High-end digital cameras are the result of advances in CMOS technology [69].

The RGB imaging device can be used for mapping and monitoring hemoglobin distribution in the skin. Dainis et al. designed an RGB imaging sensing device using a commercial RGB CMOS sensor, RGB LED ring-light illuminator, and orthogonally orientated polarizers [70]. Here, an RGB camera captured three spectral images at a time in three different spectral ranges (600-700 nm, 500-600 nm, and 400-500 nm). They converted the pixel intensity of red, green, and blue (I_R, I_G, I_B) values into optical density (absorption) changes and used these to map skin hemoglobin distribution. A CMOS image sensor (MP9P031, Micron Technology) was used near the back side of a cuvette to measure blood hemoglobin.

CCD sensor

A CCD is a light-sensitive integrated circuit (IC) where each pixel is converted into an electrical charge that is related to color. CCDs are commonly used in digital still and video cameras, astronomical telescopes, scanners, and barcode readers. CCD cameras have a high degree of sensitivity and can generate an image in low-light conditions. The image quality is not significantly hampered, even if the illumination level is low [71].

InGaAs photodetector

Indium Gallium Arsenide (InGaAs) is an alloy of indium arsenide and gallium arsenide. InGaAs is used in photodiodes as an infrared light detector. The spectral response of an InGaAs photodiode is preferred since these photodiodes have faster response, higher quantum efficiency, and lower dark current [72]. Jeon et al. used an InGaAs photode-

tector for non-invasively monitoring hemoglobin concentration and oxygen saturation from a predetermined site of the body [73]. The sensor received a signal on the other side of the body and converted the received light beams into electrical signals. They calculated the light attenuation variation for a respective wavelength and obtained a ratio of the light attenuation variation between two wavelengths. Finally, they estimated the hemoglobin concentration in blood using the proportion of the light attenuation variation and reported that the hemoglobin concentration measured by this system nearly approximated the reference hemoglobin values.

PPG Sensor

Most commonly, a photoplethysmogram (PPG) signal is captured using an optical response from the microvascular bed of a fingertip. Uguz et al. developed a SmartPPG that works on more than one wavelength and included a motion sensor [23]. The SmartPPG system has two independent LEDs at different wavelengths and two photodetector units. The authors built the SmartPPG prototype and tested to validate its applicability for arterial, venous and respiratory measurements. They used the SmartPPG prototype to collect pulse rate (PR) from 170 subjects and compared with the heart rate (HR) values derived from ECG. They obtained a goodness of fit R^2= 0.93 between SmartPPG measurements and HR derived from ECG.

2.5 Signal Processing

PPG signals are widely used for physiologic and blood constituent assessment in wearable devices. The device generated PPG signal from has motion artifacts, which is a critical problem. In this section, we discuss several signal processing strategies that are frequently used for PPG signal analysis to identify finger movement, signal noise, and motion artifact and statistical tools used for the data analysis.

Fourier analysis

The PPG signal is non-stationary and quasi-periodic. We can apply Fourier series to periodic signals and analyze them cycle-by-cycle. To remove high-frequency noise of a PPG signal, we can filter the data using a Savitzky-Golay (SG) smoothing filter. Later, the cycle-by-cycle Fourier series (CFS) analysis can be carried out. Studies showed that this method reduced the measurement error of the PPG signal from 37% to 3% [74].

Savitzky-Golay smoothing filter

Savitzky-Golay developed a data smoothing filter using a least-squares polynomial approximation. They fitted a polynomial to a set of input data and evaluated the resulting polynomial at a single point maintaining the shape and magnitude of the waveform peaks while smoothing the waveform. Building a low pass filter using this approach is known as Savitzky-Golay smoothing filter [75].

2.6 Machine Learning Algorithms

A machine learning algorithm trains a machine to learn and apply acquired knowledge in predictions. Most of the current hemoglobin prediction models use machine learning algorithms. Here, we present a list of machine learning algorithms that we have used in the work reported here to assess hemoglobin levels non-invasively. In our first study, we used ordinary least squares (OLS) and multiple linear regression (MLR) to build a prediction model, estimated hemoglobin level, and compared with invasively measured Hb level. Later, we generated features of a video using the histogram and applied the Partial Least Squares Regression (PLSR) because there were more variables than the number of observations and the independent variables are highly correlated. For ROI investigation, we obtained 100 time-series data (from 100 blocks) for each video, which was applied as individual observations to a machine learning algorithm. Then, we reduced the number of observations to identify the important block location.

Later, we developed image processing techniques for a second data set obtained under a revised protocol and applied a Support Vector Machine Regression (SVR), where we chose "Gaussian" kernel in our hemoglobin prediction model development.

Ordinary least squares (OLS)

Ordinary least squares (OLS) is a method for determining the coefficients of a linear model. OLS takes features as input matrix X and predicts an output Y. In order to predict $\hat{Y}$, we must first determine weights β_i. OLS is used in many general applications. A linear model is given here.

$$Y_i = \beta_0 + \beta X_i + \epsilon_i \Rightarrow \epsilon_i = Y_i - \beta_0 - \beta X_i, \tag{2.1}$$

$$\hat{Y_i} = \hat{\beta}_0 + \hat{\beta} X_i + \hat{\epsilon}_i, \tag{2.2}$$

where Y_i is a target value of Y matrix (dependent variable), X_i is an observation of X matrix (independent variable), β and $\hat{\beta}$ are the coefficients and ϵ and $\hat{\epsilon}$ are the error, and $\hat{Y_i}$ denotes the estimated value of Y_i. The error for each estimation will be $Y_i - \hat{Y_i}$. A training set of n observations are fed into OLS and OLS tries to minimize this error by calculating the coefficient values. The cost function is calculated using the Residual Sum Squares (RSS) method. The RSS is given by:

$$RSS\left(\beta\right) = \sum_{i}^{n} \left(Y_i - \hat{\beta}_0 - \hat{\beta} X_i\right)^2, \tag{2.3}$$

Multiple linear regression

Multiple linear regression (MLR) aims to model the relationship between two or more explanatory variables and a target variable. In simple linear regression (SLR), the model estimates the relationship between a dependent variable, Y, and an explanatory variable, X.

$$Y_i = \beta_0 + \beta_1 X_i + \epsilon_i, \tag{2.4}$$

Here, β_0 is the intercept and β_1 is the slope of the line and the error ϵ_i is considered to have a mean value of 0.

In MLR, there are p explanatory variables. In this case, the relationship between Y and X is represented by the following equation.

$$Y_i = \beta_0 + \beta_1 X_{1i} + \beta_2 X_{2i} + \beta_3 X_{3i} + \cdots + \beta_p X_{pi} + e_i, \tag{2.5}$$

where β_1 to β_p are the coefficients. In this way, multiple linear regression can be written as an extension of simple linear regression, and Y is considered as directly related to a linear combination of the explanatory variables.

Partial least squares regression (PLSR)

The Partial Least Squares Regression (PLSR) has been used in our work to design predictive models during the calculation of correlation and region of interest identification. PLS is used when the number of factors are more than the number of observations. PLS is useful when we have no limit for the number of measured factors. With a large number of factors, a few underlying or latent factors may be responsible for most of the variation in the response. PLS can extract these potential factors during data modeling. To use the elements in the prediction process, PLS extracts latent variables T from the sampled factors and U from the responses. The extracted factors T are known as X-scores, which are used to predict the Y-scores U. The predicted Y-scores are used to estimate the expected value. The X-scores explains the factor variation in the PLS algorithm. In addition, X-scores also provide informative directions in the factor space, though the information may not be related to the estimated value. The Y-scores illustrate the predicted Y variation and provide data regarding change in the responses. PLS uses both X and Y-scores to determine a reliable relationship between successive pairs of scores [76].

Support vector machine regression (SVR)

The Support Vector Regression (SVR) algorithm overcomes the dimensionality problem in regression. In support vector classification, the model finds the best hyperplane that separates the class/group with maximum distance. It finds the maximum margin in the case of classification using support vectors (called critical points of the dataset). The optimization function is given as follows [77]:

$$\frac{1}{2}||w||^2 \tag{2.6}$$

Subject to,

$$y_i - (w, x_i) - b \leq \epsilon \tag{2.7}$$

$$(w, x_i) + b - y_i \leq \epsilon \tag{2.8}$$

Different kernels are used in Support Vector Machines. One example is the linear kernel, and the other is the radial basis function (RBF) which is a popular kernel function. SVM uses kernels to create a hyperplane that preserves maximum margin among the data.

$$k_{linear}\left(x_i, x_j\right) = x_i^T x_j, \tag{2.9}$$

$$k_{Gaussian}\left(x_i, x_j\right) = exp^{-\gamma\|x_i - x_j\|^2}, \tag{2.10}$$

where x_i is the normalized feature, x_j is the support vector and γ is the degree of non-linearity.

Error measurement techniques

To present our result and the performance of a model, we calculated the goodness of fit (R^2), mean absolute percentage error (MAPE), correlation coefficient (R), and the Bland-Altman plot, mean squared error (MSE) in this dissertation.

Mean absolute percentage error (MAPE)

The Mean Absolute Percent Error (MAPE) is a commonly used metric to describe the error level in the data. MAPE is calculated as the following equation.

$$M = \frac{100\%}{n} \sum_{t=1}^{n} \frac{|A_t - E_t|}{|A_t|}, \tag{2.11}$$

where A_t=Actual value or gold standard measurement, E_t=estimated value, and n=number of measurements or observations. MAPE is used because it is easy to explain and understand and MAPE does not depend on scale.

Mean squared error (MSE)

Mean squared error measures the performance of an estimator. An attractive property of MSE is that it is easy to compute its gradient. For the more significant errors, MSE is very useful. Let, Y_i denotes the i-th target value and $\hat{Y}_i$ denotes the estimated value of Y_i. If we consider that the depenedant variable Y has n elements, then the formula for the mean squared error is:

$$MSE = \frac{1}{n} \sum_{i=1}^{n} \left(\hat{Y}_i - Y_i \right)^2, \tag{2.12}$$

Correlation coefficient (R)

The correlation coefficient (R) shows how strongly two measurement methods are linearly related. R is computed as the ratio of covariance between the variables to the product of their standard deviations. The value of R is between -1.0 and +1.0. If the value of R is +1.0 or -1.0, then we found a strong linear relationship. The formula for Pearson's correlation is given by [78],

$$R = \frac{\sum_{i=1}^{n} (x_i - \bar{x})(y_i - \bar{y})}{\sqrt{\left[\sum_{i=1}^{n} (x_i - \bar{x})^2\right] \left[\sum_{i=1}^{n} (y_i - \bar{y})^2\right]}}, \tag{2.13}$$

where n is the sample size, x_i, y_i are the individual sample points indexed with i, $\bar{x} = \frac{1}{n}\sum_{i=1}^{n} x_i$ is the sample mean, and $\bar{y} = \frac{1}{n}\sum_{i=1}^{n} y_i$ is the target mean value.

Although a correlation coefficient gives us an indication of the strength of linear relationship between the two estimation methods, we need to assess the agreement between two measurement processes [79].So, we used the Bland-Altman plot to assess the agreement between two measurements.

Bland-Altman plot

The Bland-Altman plot is used to estimate a limit of agreement (LOA) between two quantitative measurements. In general, it is common to compute 95% LOA between two measurement processes. The Bland-Altman graph plot represents the difference between the two measurement methods against the mean value of the two measurements.

Chapter 3

Protocol for First Clinical Study in Four Populations

3.1 Protocol

We collected initial data under a protocol used with patients at the Froedtert Hospital, Blood Center of Wisconsin, and Amader Gram, Bangladesh. The use of this protocol in each specific population was pursued after appropriate institutional approvals and with individual written informed consent. Specifically, in three American populations, the data collection protocol was approved by the Medical College of Wisconsin/Froedtert Hospital Institutional Review Board under the project number: PRO00020317 entitled "Monitoring of Physiological Parameters using the Camera of a Smartphone". To collect data from one population in Bangladesh, the same protocol was approved by the Institutional Review Board (IRB) at Marquette University and by the Bangladesh Medical Research Council.

Objective

The primary goal of this study was to investigate the relationship between pixel intensities of fingertip video images and gold standard laboratory determined hemoglobin levels.

Eligibility criteria

The following eligibility criteria were followed to recruit the subjects.

1. Subject's age should be at least 18 years

2. Subject is able to sign the informed consent

3. There is no skin infection on the data collection site (ventral bed of the fingertip)

4. Patient has no history of Raynaud's phenomenon

The following protocols were followed during the data collection.

1. The fingertip videos were obtained using a Google Nexus 4 smartphone
2. Normal finger-tip pressure was sought while recording the video
3. Fingertip videos were recorded before blood sample collection
4. Patients' fingers should cover both smartphone camera and light so that no ambient light could penetrate
5. Subjects' index finger of the right hand will be preferred; otherwise, if the condition of this finger does not meet the eligibility criteria, the middle finger will be used for the video data collection
6. After the informed consent, fingertip videos and blood samples by venipuncture should be collected from patients

Methods

A research coordinator (RC) captured a single 10-15 seconds fingertip video using a Galaxy Nexus 4 phone with Android 4.1 Jelly Bean operating system. The primary camera of the cell phone was used with camera light on. The patients were instructed to press gently on the camera using the ventral bed of the index finger of the right hand (Figure 3.1). The Nexus smartphone captured each video using 1280×720 pixels resolution at a frame rate of 30 frames per second (FPS). The smartphone's built-in camera light was turned on for the full duration of video recording. The RC used an identification (ID) number with the video file name to save the fingertip video in the local memory of the smartphone. The laboratory determined hemoglobin level information was provided to the research coordinator later. This clinically-measured hemoglobin (CHb) levels were treated as the gold standard hemoglobin levels in this study.

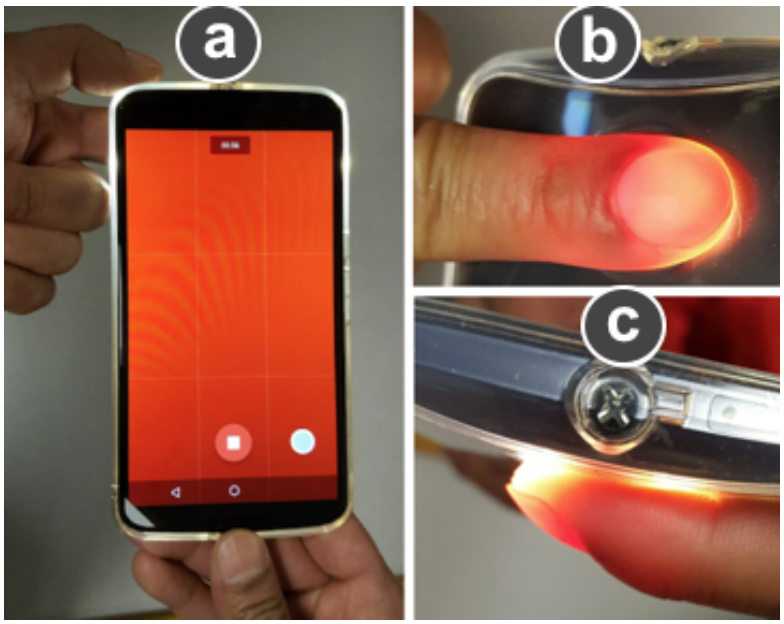

Figure 3.1: Fingertip video recording process: a) get the finger and smartphone camera ready. b) turn the built-in camera light on. c) record a video.

3.2 Demography

We collected datasets from four populations.

Froedtert Hospital

Data were collected from 17 sickle cell patients presenting to the Emergency room of the Froedtert Hospital of Medical College of Wisconsin. These data are referred to as the `FDT-17`. These data consists of fingertip video data from 11 males and six females with hemoglobin levels between 4.8 $g\ dL^{-1}$ and 15.9 $g\ dL^{-1}$ and age range was between 21 and 73.

Blood Center of Wisconsin

We collected data under this same protocol at the Blood Center of Wisconsin (BCW) from five sickle cell patients who received a blood transfusion. During these data collections, two individuals had significant hand and finger tremulousness while capturing the fingertip videos. Because of this, we recorded three fingertip videos for each blood transfused subject (BTS). Since each subject provided three videos, we stored 15 finger-

tip videos recorded before they received their blood transfusions. Two weeks following the blood transfusions, all five patients returned to provide additional subsequent fingertip videos and blood samples for a complete blood count (CBC). This final dataset included 30 videos. Each fingertip video was treated as an individual observation, so we had a total of thirty observations from this patient-group. We refer this dataset as the `BTS-30` dataset in the following sections. The hemoglobin levels before and after the blood transfusion process are presented in Table 3.1. We did not gather age or gender information for this `BTS-30` dataset.

Table 3.1: Hemoglobin level of blood transfused subjects at the BCW

Sub ID	**Before** ($g\ dL^{-1}$)	**After** ($g\ dL^{-1}$)
BTS-01	7.5	10.0
BTS-02	7.2	10.3
BTS-03	8.7	11.6
BTS-04	7.2	10.6
BTS-05	10.1	10.4

Following this, at the BCW, we collected a second data set from a group of 30 sickle cell patients where the group was comprised of 19 females and 11 male participants. The age range of this patient group was from 19 years to 60 years, where the average age was 33 years. Only four patients were older than 50 years. This dataset is named `SCD-30`.

Amader Gram, Bangladesh (AGB)

Finally, under this same protocol we collected fingertip videos and CHb levels through a collaboration with Amader Gram, a Non-Governmental Organization (NGO) operating a Breast Care Clinic in Khulna, Bangladesh. There women patients and male accompanying visitors were recruited. We collected subjects' age and gender. The subjects were all believed to have normal blood oxygenation (SpO2) levels. The skin tones of all subjects were similar. Overall, we collected data from 75 healthy volunteer subjects

with an age range from 20 years to 56 years. In this patient group, there are fifty-five women and twenty men. The laboratory hemoglobin levels ranged between 7.6 $g\ dL^{-1}$ and 13.5 $g\ dL^{-1}$. We named this dataset as `AGB-75` in our data analysis.

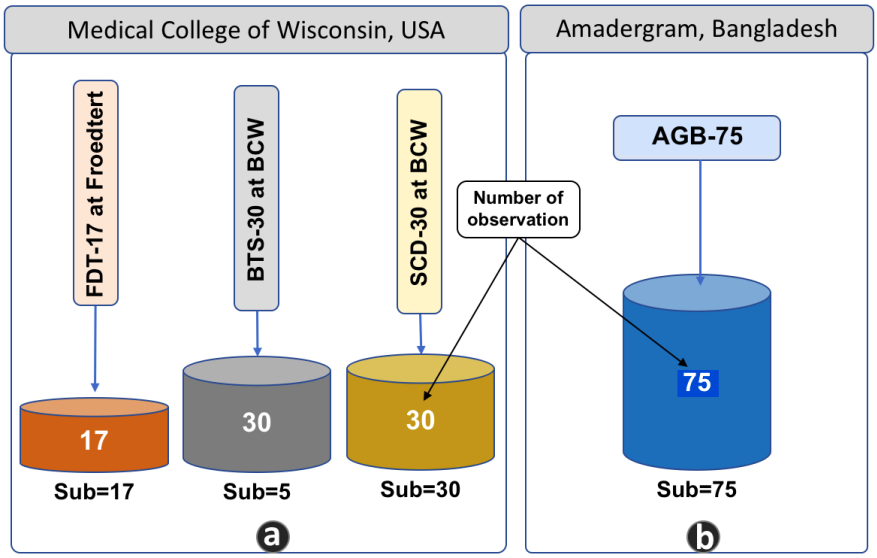

Figure 3.2: Summary of four populations from whom data were acquired under our first clinical protocol. The summary consists of dataset name, capture location, number of subjects, and number of observations. Sub=X means X subjects at the particular location. At most one observation per subject except for six observations per subject in the `BTS-30` dataset.

Chapter 4

Pixel Intensities Analyses of Fingertip Videos Collected Under First Clinical Protocol

In this chapter, we examined the red pixel intensities from fingertip videos and studies linear correlation with Hb levels of patients' (`FDT-17`) dataset. For each video, we converted the sequence of video frames to three time series: average of the red, green and blue pixels for each frame. We calculated mean pixel intensities for all frames and conducted the regression analyses. We compared the average of the red pixel intensities over all the frames and the corresponding hemoglobin levels. We found significant correlation between the red pixel intensity from the videos and the hemoglobin levels by gold standard venipuncture laboratory testing. Applying linear least squared regression, we found a correlation coefficient (R) of 0.68 [80].

Subsequently, we analyzed each of the four datasets (captured in the first clinical study) to study the pixel intensity variations with different CHb levels. In this work, we selected fingertip video that satisfied these selection criteria:

1. Each 10-15 second-video is X megabytes (MB) where X might be around 30 to 35 MB.

2. The video file is not corrupted.

3. The dataset has a CHb levels for each video.

4. Each video plays without any flickering or issues.

After selecting fingertip videos, we processed each video using these following steps as shown in Figure 4.1.

1. Extract each frame of a video (Figure 4.1(b)).

2. Separate red, green, and blue pixel intensities from each frame (Figure 4.1(b)).

3. Generate histogram values for each pixel's frame (Figure 4.1(c)).

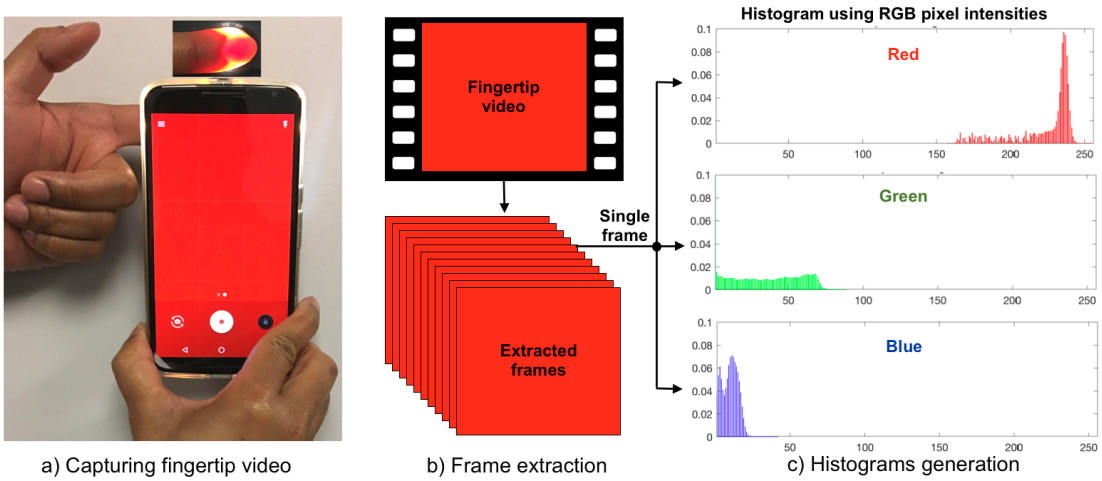

Figure 4.1: Flowchart of RGB image analysis process a) Fingertip video recording with a smartphone having camera light on (10-second video) b) Frame extraction from a video c) Histogram generation for each frame's red, green, and blue pixel intensities.

4.1 RGB Pixel Intensity Analysis

We extracted frames from a video and analyzed each frame for different color pixel intensities. Here, we illustrate the pixel intensities of images for red, green, and blue pixels.

An image pixel has three dimensions: height, width, and channels. Channel value tells us how many different color pixels are used to show the image. For example, if the channel value is 3, then the image frame is presented as RGB, HSV or any other three channel pixel values. If the channel value is one, then the image is a grayscale image. In general, the pixel intensity value for each color ranged from 0 to 255. If we extract the individual red color pixel of a frame and plot the pixel intensities using a color map, then Figure 4.2 (a) is an example of that frame. The color map of green and blue pixel intensities of the same frame is presented in Figure 4.2 (b) and Figure 4.2

(c). In Figure 4.2, we observe that the red pixel intensity values are between 184 and 248, the green pixel intensity values are between 10 and 45, and the blue pixel intensity values are between 0 and 20. To understand an image pixel intensity distribution, we create a histogram for each color of a frame.

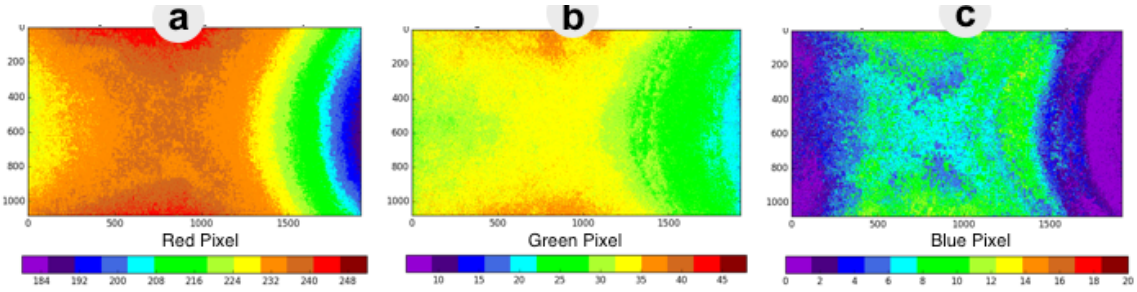

Figure 4.2: A colormap presentation of a) red, b) green and c) blue pixel intensities of a single frame separately.

4.2 RGB Histogram

A color histogram is a bar-graph-illustration of each pixel intensity of an image that shows the complete color description of a particular image [81]. Statistically, a color histogram gives the distribution of different colors, regardless of their spatial description. We know that pixel intensity values for each red, green, and blue color pixel vary from 0 to 255. For each individual color (red, green, and blue) we make a histogram with 256 bins (bin number values denoting intensity values from 0 to 255), then the histogram shows each pixel's frequency in an image. Although the color-pixel histogram of an image has some limitations, a color histogram was used because it is an indicator of a picture in the domain of computer vision and image processing. The histogram-based approach is used in the feature space identification since the frequency of each color pixel represents different pixel contributions in a picture. For example, the peak of a histogram can change based on the intensity and brightness of an image. Figure 4.3 (a) shows histograms for two different images of a subject having hemoglobin levels of 7.2 $g\ dL^{-1}$ and 10.6 $g\ dL^{-1}$. The histogram using red color pixel intensities of the

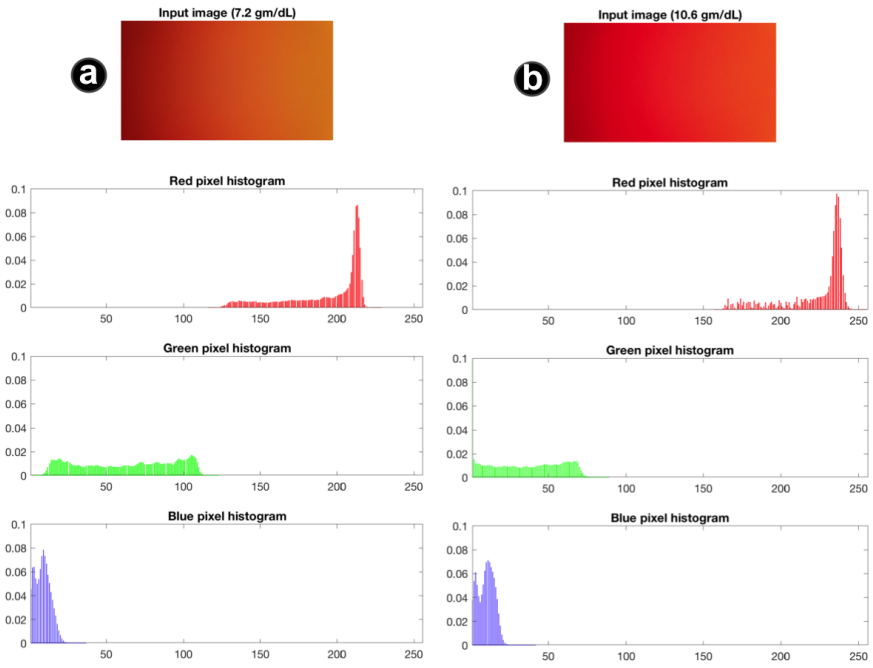

Figure 4.3: The histogram of red, green, and blue pixels of an image frame. Horizontal axis are the intensities of each color, the vertical axis is the relative frequency of the intensity occured in the frame. a) In this case, an image frame is extracted from a fingertip video of an individual before he received a blood transfusion, blood drawn determind Hb level was 7.2 $g\ dL^{-1}$. b) Another image frame is extracted from a fingertip video of the same individual two weeks later following a blood transfusion, blood drawn determind Hb level was 10.6 $g\ dL^{-1}$.

image (7.2 $g\ dL^{-1}$) shows that the red pixel intensities are between 120 and 220.

The red-intensities of a histogram of the 10.6 $g\ dL^{-1}$ images are are between 170 and 245 compared to the range 120 to 220 where Hb was 7.2 $g\ dL^{-1}$. (b)). The histogram values for green pixel intensities also change from low and high levels of hemoglobin. For these two Hb levels, we observe very minimal changes in the histogram values for blue color pixel intensities.

To understand the pixel variations with hemoglobin levels, we analyzed the fingertip videos using an image mask based on a threshold value. In Figure 4.4, the regular fingertip image, and respective masked images are shown. Here, we observe that the masked image pixels vary for the lower and higher-level of Hb. Figure 4.3 and Figure 4.4 present a significant change in the histograms and masked images, which are

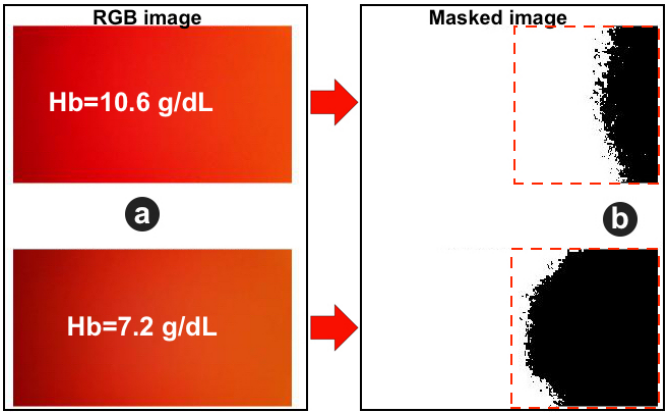

Figure 4.4: RGB image versus masked image. a) The RGB image was extracted from two different videos of a person who received a blood transfusion. The top image was taken from a video which was captured when a person had higher-level of hemoglobin two weeks following a blood transfusion. The bottom image was taken from a video which was recorded from the same subject before they received the blood transfusion. b) The masked images are presented on the right side (the original RGB images are on the left side).

created using the pixel intensities of images captured under lower and higher-levels of Hb.

Histogram value analysis

While checking the fingertip videos, we observed random and wide intensity fluctuations in the early frames of most of videos. These fluctuations may have come from several sources. For example, photobleaching can affect the recorded video signals for the first few seconds. In addition, the auto-fluorescence intensity is reduced over time [82]. Movement while putting the finger on the smartphone camera and releasing the finger might also cause variable pixel intensities. Since the fingertip videos were often a little longer than 10 seconds taken at 30 fps, we had more than 300 frames in most videos. Because of these observations, we chose to use the frame numbers from 201 to 300 to create our histogram values and input feature matrices. After histogram generation, we averaged 100 histogram values generated by 100 frames of a video and selected a single observation of a video for one color pixel. We calculated three histogram values based

on the selected frames for red, green, and blue color pixel intensities, which provided three feature vectors from one video. We used Python OpenCV, Matlab, and R for video and image processing.

We calculated three histogram values for each frame: first histogram values were calculated for red pixels, the second one was created using green pixels, and third values were obtained from blue pixels (Figure 4.3). If we consider 100 frames per video, then we will obtain 100 histogram values for each red, green, and blue pixel intensities. For the red color, averaging the 100 histogram values, we calculated a feature vector for the red pixel intensities in a video. We defined this feature vector as Red Averaged Histogram (RAH). Similarly, we obtained Green Averaged Histogram (GAH) for green pixel intensities and Blue Averaged Histogram (BAH) for blue pixel intensities. A combined feature vector (observation) was generated concatenating the RAH, GAH, and BAH values of a video where the RAH is followed by the GAH and BAH values sequentially. The total length an observation is (256+256+256)=768, since each averaged histogram had 256 values. A feature matrix can be generated using a dataset with several fingertip videos. In the `FDT-17` dataset, we obtained 17 fingertip videos which produced a feature matrix with a dimension of 17×768. Applying similar techniques, we calculated feature matrices for the other datasets. The `SCD-30` dataset has a dimension size 30×768, the `BTS-30` dataset has a dimension size 30×768, and the `AGB-75` dataset has input feature matrix size 75×768. From the dimensions of each dataset, we observed that each input feature matrix was high-dimensional since it contained more variables than observations.

Traditional multivariate techniques are not applicable to high-dimensional data analysis, e.g., predicting a hemoglobin response of a subject from the spectral (high-dimensional) data of a fingertip is a difficult and challenging task which requires various methods (variable selection or dimension reduction). Partial Least Squares Regression (PLSR), however, is a powerful approach for analyzing high-dimensional data. PLSR can work

well for a dataset comprised of small sample sizes where the dataset has more parameters than the number of observations. In PLSR, both dimension reduction and regression are performed simultaneously. In the PLSR method, the response matrix Y is considered for the construction of the PLS components where the PLS components have high covariance with the response [83]. The PLSR has been used to build prediction models for many regression problems including gene expression [84], missing values imputation [85], and prediction of the protein structure [86]. Because of these reports, we select PLSR in our prediction model work. The correlations between estimated hemoglobin levels using fingertip videos and the clinically measured (gold standard) hemoglobin levels are calculated to present the association level (R) of pixel intensities. The percentage of errors are shown using the mean absolute percentage error (MAPE) where a lower MAPE indicates a better model.

To build a prediction model, PLSR generates orthogonal PLS components that are calculated by maximizing the covariance between linear combinations of the columns of the input feature matrix (X) and the response (output) matrix (Y) [87]. In PLSR, the optimal number of PLS components selection is critical. Choosing a less-than-optimal number of PLS components leads to a loss of relevant information. On the other hand, selecting a more-than-optimal number of PLS components provides poor predictive performance because the model over-fits the input data [88]. In our study, we used four values for PLS components based on the sizes of input feature matrices. Before applying PLSR, we standardized to have mean 0 and standard deviation 1. Then, we applied 2, 5, 7, and 10 as a value of PLS components to the standardized datasets. We chose 2 PLS components for the `FDT-17` dataset, 5 PLS components for the `SCD-30` and `BTS-30` datasets, and 10 PLS components for the `AGB-75` dataset and compared the results. The MAPE and linear correlation coefficient (R) show the performance from each dataset. In addition, we created combined datasets, and PLSR was applied on each of these. We used 10-fold cross-validation (CV) in all of the hemoglobin prediction

model development processes.

4.3 Results and Discussion

Applying the PLSR with 2 PLS component to the FDT−17 datasets, we observed that the MAPE was 17.12% and the correlation coefficient, R=0.74. Using five PLS components in the analysis of BTS−30 dataset, a 3.73% MAPE was observed where the value of R was 0.96 (Figure 4.5a and Figure 4.5b). We acquired a MAPE=6.26% and R=0.92 analyzing the SCD−30 dataset (Figure 4.6a) and a MAPE=4.84% and R=0.80 for the AGB−75 dataset (Figure 4.6b).

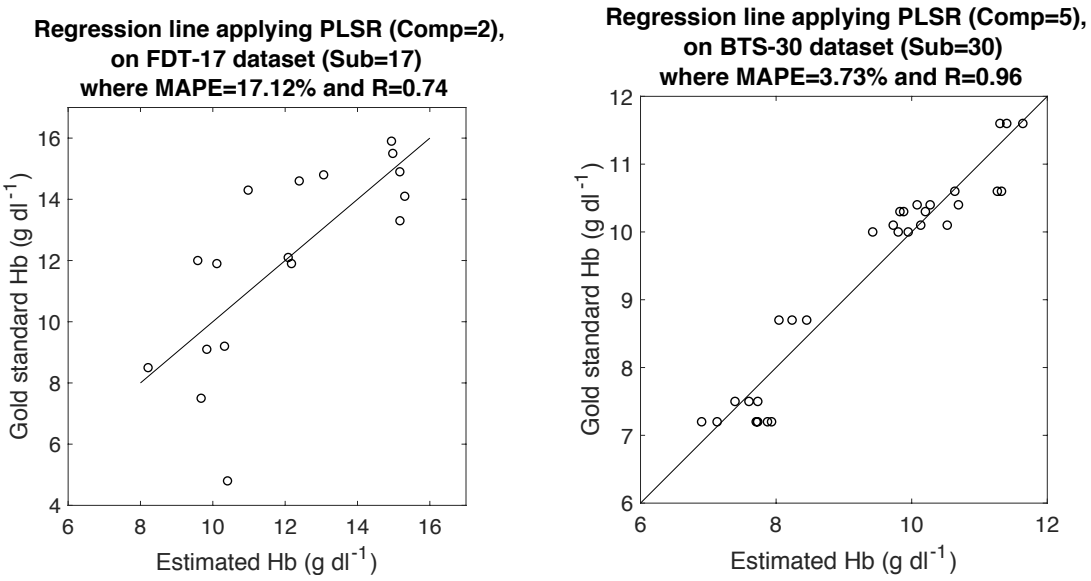

(a) FDT−17 dataset. (b) BTS−30 dataset.

Figure 4.5: Applying the PLSR, a regression line is generated for each dataset a) the FDT−17 dataset using 2 PLS components b) the BTS−30 dataset using 5 PLS components.

We then combined four standardized datasets (FDT−17, BTS−30, SCD−30, and AGB−75) where the number of observations was 152. Then, we used the PLSR to build a hemoglobin prediction model using 10 PLS components, since the number of individuals was greater than the individual sample size. The prediction model pro-

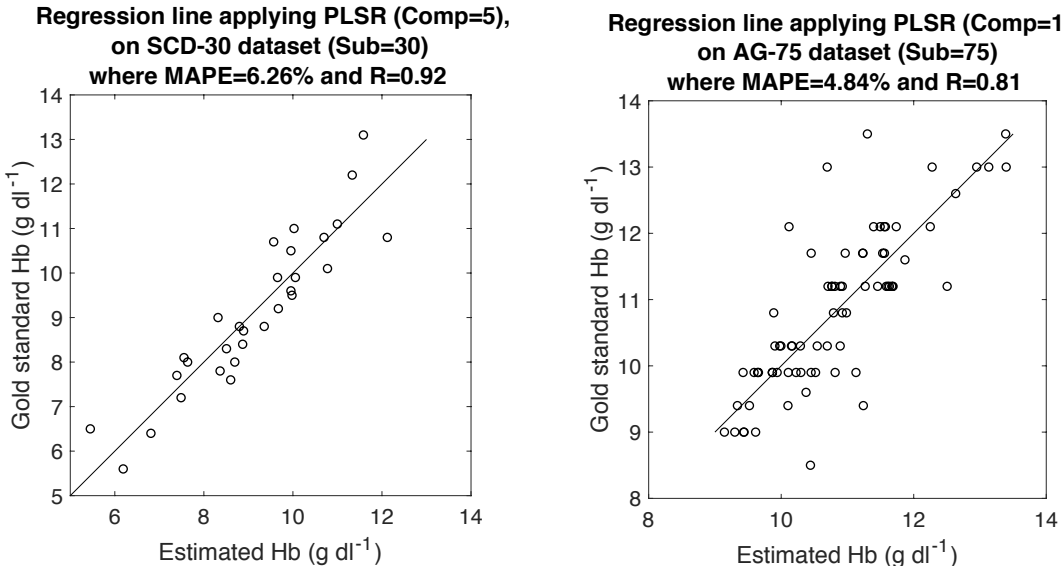

(a) SCD−30 dataset. (b) AGB−75 dataset.

Figure 4.6: Applying the PLSR, the regression line is generated for the SCD−30 dataset using 5 PLS components and AGB−75 dataset using 10 PLS components.

duced MAPE=8.99% and R=0.79 for this sample size (Figure 4.7). We also checked the MAPE and R for a combination of two or more datasets where we changed the number of PLS components (e.g., 2, 5, 7, and 10). We present the calculated MAPE and R in Table 4.1.

In this analysis, we observed significant changes in red and green pixel histograms (Figure 4.3). Since each histogram has 256 values for each color, a concatanation of three histograms leads to a high-dimensional feature vector of size of 768. To analyze this high-dimensional dataset, we chose the PLSR algorithm where variable numbers of PLS components (2, 5, 7, and 10) were applied and the calculated results are presented in the Table 4.1. In our approach, we see that a prediction model built applying PLSR on the FDT−17 dataset shows a higher correlation (R=0.74) using only 2 PLS components. The correlation coefficient is higher for each dataset when we increase the number of PLS components. However, an increased number of PLS components builds a prediction model that may over-fit the input data.

As described in Chapter 3, the demographics of the four studied population groups

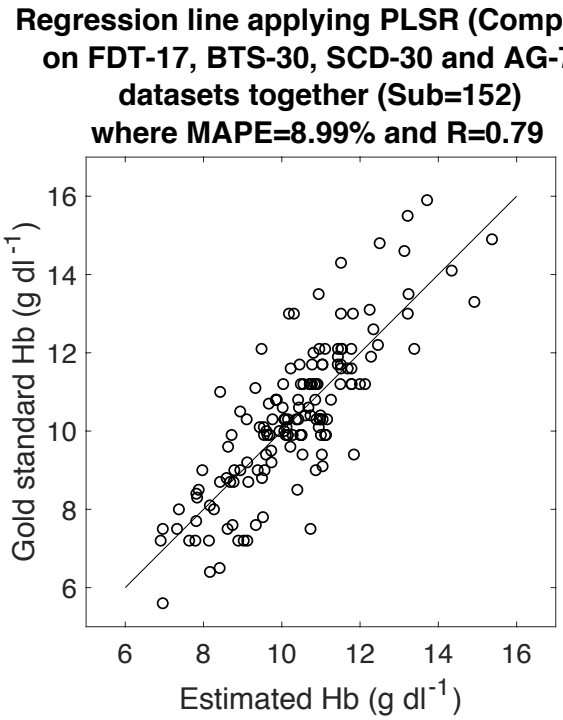

Figure 4.7: Applying the PLSR on the combined FDT−17, BTS−30, SCD−30, and AGB−75 datasets, a regression line is presented, where the prediction model is built using 10 PLS components for 152 observations.

differed. To investigate the changes in the correlation coefficient (R) analyzing the datasets collected by country locations, we combined three datasets that were collected in the USA. Combining these three datasets, we obtained 77 observations where we applied PLSR using 10 PLS components (Table 4.1). The prediction model built using 77 subjects' fingertip video data gave MAPE=8.18% and R=0.88. Applying PLSR on the AGB-75 dataset using 10 PLS components, we observed MAPE=4.84% and R=0.81 for 75 individuals. Since locations, demography, physiological parameters, and patient conditions were different, the variations in the correlations (R) are not unexpected, though the sample sizes are very close to each other (the USA sample size=77 and Bangladeshi sample size=75). To investigate the performance of a model on the mixed datasets captured from both locations, we combined those four datasets: FDT−17, BTS−30, SCD−30, & AGB−75 totaling 152 observations. We employed the PLSR on this combined dataset using 2, 5, 7, and 10 PLS components where the value of R

Table 4.1: Summary of the MAPE and the correlation coeffecient (R) for the prediction model created using various PLS components and datasets.

Dataset	Apply PLSR using various PLS Components							
	2		5		7		10	
	MAPE	**R**	**MAPE**	**R**	**MAPE**	**R**	**MAPE**	**R**
FDT-17	17.12%	0.74	10.99%	0.86	7.97%	0.92	3.08%	0.98
BTS-30	9.64%	0.69	3.73%	0.96	2.19%	0.99	0.88%	0.99
SCD-30	11.69%	0.68	6.26%	0.92	4.12%	0.97	2.04%	0.99
AGB-75	8.33%	0.51	6.44%	0.68	6.07%	0.72	4.84%	0.81
FDT-17 & BTS-30	15.16%	0.67	10.73%	0.83	7.92%	0.89	6.46%	0.90
FDT-17, BTS-30, & SCD-30	16.38%	0.59	11.34%	0.80	9.62%	0.84	8.18%	0.88
FDT-17, BTS-30, SCD-30, & AGB-75	13.39%	0.50	10.68%	0.71	10.12%	0.74	8.99%	0.79

was calculated as 0.5, 0.71, 0.74, and 0.79 respectively.

Here, the correlation coefficient (R) was decreased from 0.81 to 0.79 where the prediction model on combined datasets of the USA (FDT-17, BTS-30, SCD-30) showed R=0.88 and the prediction model of AGB-75 gave R=0.81 individually. This decreased correlation coefficient (R) was likely seen for several reasons, including different patient physiological parameters and demographic variables. For example, the individuals in the USA were sickle cell patients, but the participants in the AGB-75 were healthy. The distribution of male and female subjects was not equal in the two locations. Skin color, the range of hemoglobin levels, perhaps the clinical methods to measure the hemoglobin levels from a blood sample, and weather/temperature variables also different in the two populations.

The linear correlation between the estimated and laboratory-measured hemoglobin levels for the combination of all datasets (152 observations) was not much different from the R-value for the datasets collected in the USA and the R-value for AGB-75

dataset individually. The reason is that we used 10-fold cross-validation (CV) in all of the hemoglobin prediction model development processes. We also standardized the input feature matrices before applying the PLSR on the dataset. Using this strategy, we calculated R=0.79 for 152 observations considering only 10 PLS components. This low number of PLS components imply the time-series data can be well modeled with a small number of principal components [89].

4.4 Conclusions

In this chapter, we have reported on investigations of the correlations between image pixel intensities-based hemoglobin levels and clinically measured hemoglobin values. We illustrated the histogram-based feature generation from each fingertip video, which was used in prediction model development. The estimated hemoglobin levels based on this model were compared with the subjects' clinical hemoglobin levels where we observed a strong linear correlation with lower (MAPE) errors. We also apply this approach on the combined datasets captured from the USA and Bangladeshi patients, where we found decreased linear correlation coefficients (R) likely consequent to patients' variable physiological parameters.

In this study, RGB histogram values provide strong correlations, but histogram-based features have some limitations. For example, multiple histogram values can be obtained from the same image with different exposure, white balance, and contrast levels. Also the creation of a RGB histogram is complex when compared to the creation of gray-scale image histograms. Further, RGB histogram may increase the computational time for image processing [90].

Since smartphones are equipped with high-resolution cameras which can generate large video files, we desire a solution to use these devices to reduce the data transmission load between a smartphone and a cloud computer. In the next chapter, we present a technique that we used to identify the region of interest (ROI) of an image for PPG signal processing. We reasoned that if we could find a location that provides a higher

PPG signal-to-noise ratio (SNR), this might help in reducing the data transmission by sending cropped data of the ROI data from a fingertip video rather than the full video.

Chapter 5

Identifying the Region of Interest in Videos

In our first clinical study (Chapter 3), we captured fingertip video data using a Google Nexus 4 smartphone, but several smartphone companies have recently unveiled smartphone camera sensors with the higher resolution (e.g., 48 megapixels). With higher smartphone camera resolution, a fingertip video becomes larger in memory-size, which would be challenging for image processing. To overcome this challenge, we investigated a method to minimize the data analysis area of an image frame to save computing resources and to reduce the size of video transmission process from a smartphone to a cloud server. In this chapter, we subdivided an image frame into an N×N block matrix. Then, we calculated the mean pixel intensities in each block of a video, generated time-series data for each block across the video frames, applied a machine learning algorithm on a group of blocks' averaged time-series data to build a prediction model, and compared the estimated hemoglobin levels with CHb levels to identify the important feature location. We analyzed the four datasets (`FDT-17`, `BTS-30`, `SCD-30`, and `AGB-75`) for ROI identification.

5.1 Related Work

In image-based research, identifying a region of interest (ROI) is essential to find a strong signal-to-noise ratio (SNR) signal from an image to reduce the computing and data transmission time. Different image locations have been studied seeking to capture the strongest PPG signal from video. For example, Jonathan et al. used 10×10 pixels from a central region of an image frame and averaged intensity values for PPG generation [91, 92]. Scully et al. computed a PPG signal by cropping a 50×50-pixel area from the green channel data and averaged the pixel intensities [40]. To estimate hemoglobin values, Edward et al. cropped half of the width and half the height from

the center of an image and averaged the intensity for each channel [6].

Other studies have shown that a PPG signal could be created in various ways: considering the entire image captured by a smartphone for pulse rate [93] and heart rate [94] measurement, circular area for contour analysis [95], and 50×50-pixel resolution image for heart rate and respiratory rate [96]. But cropping a specific ROI of an image increases the chance of losing important information. Optimal ROI is studied to seek clean PPG signals. A recent study explored the signal quality by the largest amplitude values for multiple smartphones to generate reliable and clean signals where multiple blocks were used to show the pixel intensity variations [96].

In our study, we investigated the whole image subdividing it into N×N block sizes of a video to identify the optimal ROI. Any number can be chosen for the value of N (e.g., 5, 10, 20, and 25) to subdivide an image into multiple blocks. To present our approach, we consider N=10 to create 100 blocks where each block has a specific number of red, green, and blue (RGB) pixels. The video processing methodology is presented below.

5.2 Methodology

For ROI area identification, we processed each video following these steps (Figure 5.1).

1. Extract image frames from each fingertip video (Figure 5.1 (a-c)).

2. Separate the red, green, and blue pixel intensities (Figure 5.1 (d-f)) for each frame.

3. Subdivide an image frame into a 10×10 block matrix (Figure 5.1 (g-h)) where each rectangular-shaped area of this (Figure 5.1 (h)) image is defined as a block.

4. Average red, green and blue pixel intensities of each block where each frame gives us 100 average (mean) values for red pixels, 100 averaged values for green

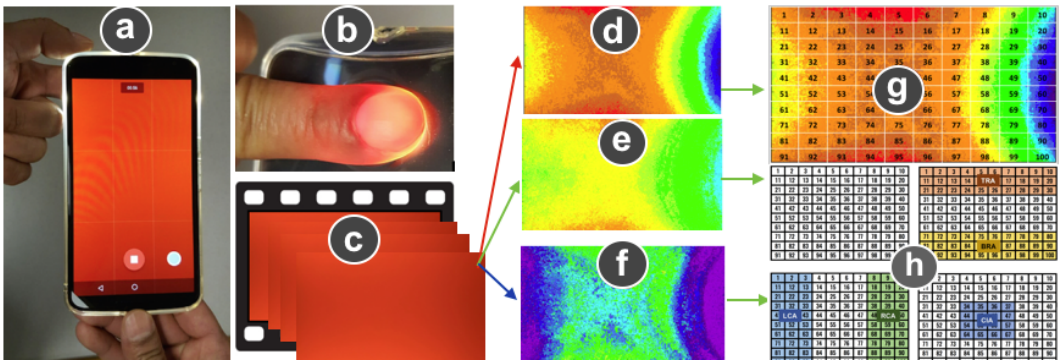

Figure 5.1: Fingertip video capture, video frame extraction, and subdivision of image frame to generate the input feature matrix systems. a) An index finger is put on the smartphone camera with the camera recording a 10-second video with a camera light on. b) The index finger covers both the camera lens and camera light. c) Three hundred frames are generated from each video. d-f) Each frame has red, green and blue (RGB) color pixels. The color maps of red, green, and blue color pixels of an image are presented in d, e, and f respectively. g) A frame is divided into a 10×10 block matrix. h) A group of blocks are considered to generate time-series signals and averaged to use as an input feature vector.

pixels, and 100 averaged values for blue pixels.

5. Generate time series data as input feature (Section 5.2.1).

6. Group multiple blocks together to identify ROI area (Section 5.2.2)

5.2.1 Time series data generation

For each color pixel, each block across 100 frames of a video would have 100 mean values (Figure 5.2). Plotting of these 100 mean values generates a time-series signal for one block across 100 frames of a fingertip video. For example, Figure 5.2 represents the average pixel intensity variation for block number 10 and 96 where each black dot presents a mean value of the respective block. By plotting 100 mean values of a single block of a video, we generated a time-series signal for that block. By calculating the mean values of 100 blocks across 100 frames, we generated 100 time-series signals for a fingertip video. These 100 time-series data were separated into five groups, and each group in this study was used as a feature vector where Partial Least Squares Regression

(PLSR) was applied to build a prediction model.

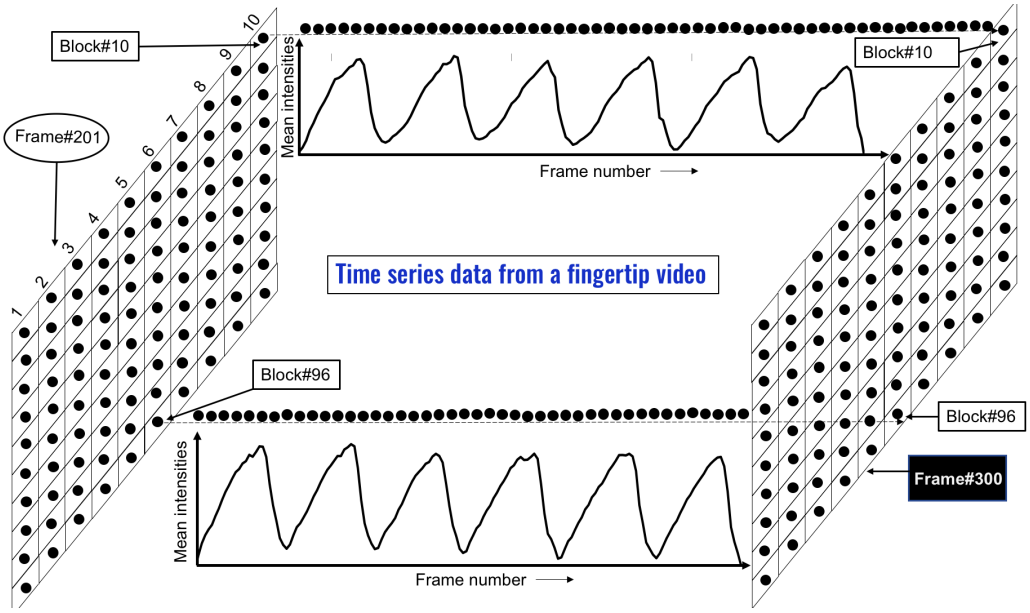

Figure 5.2: Time-series data is generated in each block averaging the the pixel intensities of the same block across 100 frames.

5.2.2 Grouping of multiple blocks

After subdividing an image into a 10×10 block matrix (Figure 5.3(a)), we defined each of the five groups using a unique name. The top three rows of blocks were grouped, which was named as top row area (TRA) (Figure 5.3(b)). We identified the bottom three rows of blocks as the bottom row area (BRA) (Figure 5.3(b)). Similarly, the left three columns and right three columns of the 10×10 block matrix were named as left column area (LCA) and right column area (RCA) in the following sections (Figure 5.3(c)). A 4×4 block area from the middle of the 10×10 block matrix was named as a central image area (CIA). Each group of blocks was used to generate the time-series signal as shown in Figure 5.2. Then, we averaged the values of those grouped time-series signals to create a single observation. Thus, we calculated five input feature matrices (`TRA`, `BRA`, `LCA`, `RCA`, and `CIA`) for each video. We employed the PLSR on each the five input feature matrices for different datasets. We compared the MAPE and the

correlation coefficient (R) among these five input feature matrices for each dataset. In exploring all of these five input feature matrices for different datasets, we investigated the location of the region of interest (ROI).

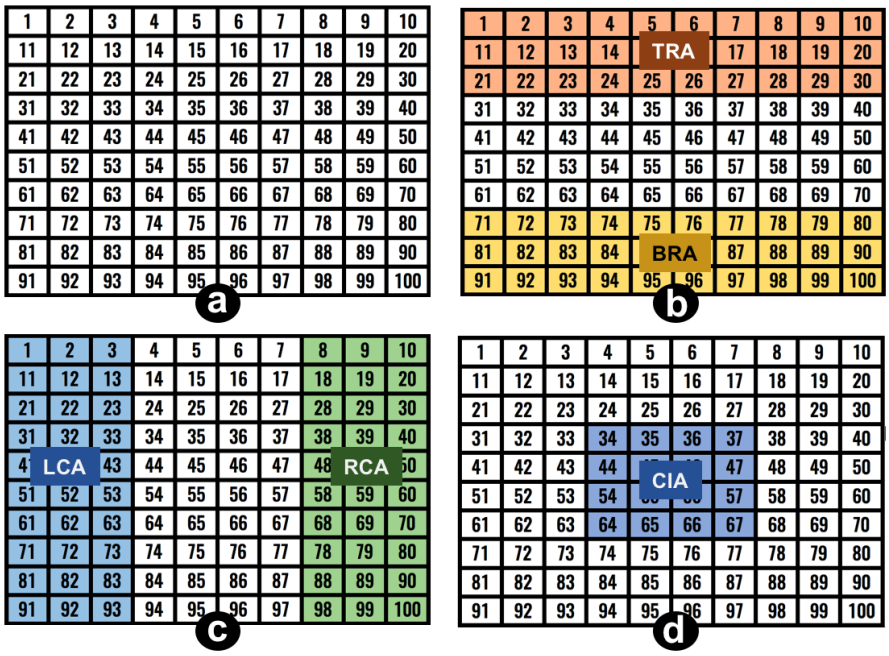

Figure 5.3: A single image is subdivided into a 10×10 block matrix. Again, a group of blocks are defined with different name based on their location a) A subdivided 10×10 block image b) Top (three) row area (TRA) and bottom (three) row area (BRA) is taken from the top and bottom of an image. c) Left (three) column area (LCA) and right (three) column area (RCA) are chosen from left and right side of an image. d) Central (4×4 blocks) image area (CIA) is selected from the middle of an image.

5.2.3 Dataset preparation

As previously remarked, we used frame numbers 201 to 300 (total 100) for our input features. The mean pixel value (red, green or blue pixel) of each block was considered to generate a time-series signal for red, green, and blue pixels separately.

For each fingertip video, we calculated five input feature vectors (observations) called TRA, BRA, LCA, RCA, and CIA based on five groups of blocks. For the $AGB - 75$ dataset, we created five subsets of input feature matrices for that dataset. As illustrated in Figure 5.3, we observed that each of TRA, BRA, LCA, and RCA were

comprised of 30 time-series signals and the CIA had 16 signals. To generate a single observation, we averaged 30 signals into a single time-series signal for the TRA, BRA, LCA, and RCA and we averaged 16 time-series signals for the CIA. Then, we applied the PLSR on each averaged subset where the dimension of the TRA, BRA, LCA, RCA, and CIA was 75×100. Afterward, we calculated the MAPE and R values for five subsets (TRA, BRA, LCA, RCA, and CIA). Later, we compared which subset provided comparatively better performance based on MAPE and R values. In Table 5.1, we present the ROI area name with R values (in parentheses) of five subsets of input feature matrices for each dataset.

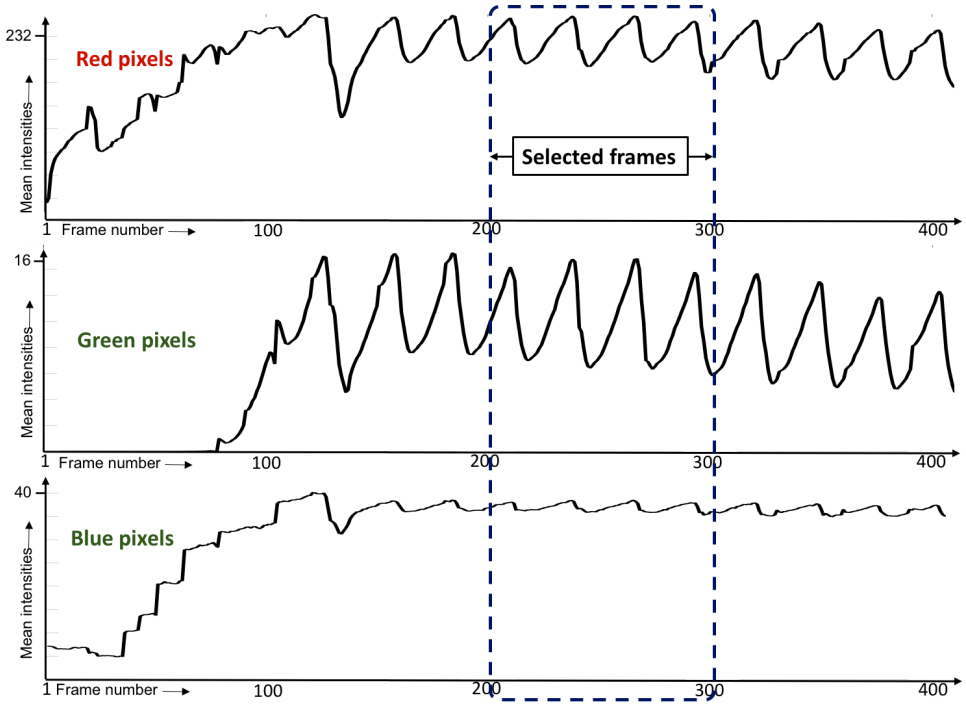

Figure 5.4: The time-series data are generated from the selected frames, which are from frame number 201 to 300.

5.3 Results and Analysis

We used 10-fold cross-validation in the PLSR algorithm to each dataset. In the `FDT-17` dataset, we generated TRA, BRA, LCA, RCA, and CIA feature vectors for

each video. For the FDT−17, we applied the PLSR with 2 PLS components to the TRA feature vector and calculated the correlation (R) value between the estimated hemoglobin and CHb levels. We also applied the PLSR with 2 PLS components in other BRA, LCA, RCA, and CIA subsets individually. Finally, we found five correlation coefficients (R) value where we found the highest R=0.54 for LCA using red pixel intensities. Thus, we can say that analyzing the red pixel intensities of 17 videos we found the LCA as an ROI since the calculated R from this LCA group provided the highest R-value. Considering green and blue pixel intensities of 17 videos, we observed that LCA and TRA were selected as the ROI area.

We also checked other datasets where each dataset was subdivided into five subregions (TRA, BRA, LCA, RCA, and CIA) as shown in Figure 5.3. For each dataset, we calculated the linear correlation (R) and selected the largest R among five groups. The group which was associated with the largest R is presented in Table 5.1 as the best ROI. We also combine all four datasets (Combined), which is comprised of 152 observations. In this case, the LCA is the ROI area for red pixel intensities, BRA is the ROI area for green pixel information, and RCA is the ROI area when we analyzed the blue pixels of 152 fingertip videos.

Investigating ROI area for each dataset, we saw that the LCA was found as the most frequently (six times) selected ROI area when we considered red, green, and blue pixel intensity-based ROI identification. Other ROI areas were also selected several times, which did not allow us to identify a single optimal ROI area. With these challenges, we checked the fingertip videos manually once again, where we observed that several videos were captured vertically, and the remaining videos were recorded horizontally. These two types of videos were recorded due to the auto orientation of the smartphone camera. Since the user did not turn off the auto orientation, the videos orientations were also changed. This may explain why we observed different ROI areas in different datasets.

Table 5.1: Region of interest (ROI) area identification analyzing five locations of an image (the largest R is given in the parentheses) for single as well as combined datasets captured under the first clinical study.

Dataset	**Comp.**	**Red**	**Green**	**Blue**
FDT-17	2	LCA (R=0.54)	LCA (R=0.74)	TRA (R=0.46)
SCD-30	5	LCA (R=0.77)	RCA (R=0.84)	RCA (R=0.76)
BTS-30	5	TRA (R=0.85)	TRA (R=0.95)	LCA (R=0.82)
AGB-75	10	TRA (R=0.81)	BRA (R=0.80)	RCA (R=0.79)
Combined	10	LCA (R=0.63)	BRA (R=0.62)	RCA (R=0.44)

Comp.=Number of PLS Components

5.4 Conclusion

We investigated five ROI areas of each video for multiple datasets. We used the PLSR on each dataset, which was created based on different ROI areas. In most cases, we identified LCA as the best ROI area when compared to the linear correlation coefficient (R) values of other ROI areas. Since LCA included fewer blocks of information, a faster computing and data transmission process is possible for hemoglobin level estimation. Since the auto-rotation option of Nexus 4 was not turned off, some videos were recorded with vertical shape. We surmised that a fingertip area closer to the camera light might have more pixel variations in the video than the other area locations. That is why, camera light on a fingertip location influence the investigation process of ROI area. In our second clinical study, we turned off this (auto orientation) option during the fingertip video recording.

Chapter 6

Theoretical Foundations and Protocol Design for Our Second Clinical Study

In the previous two chapters, we reported on the linear correlation coefficients between the estimated and CHb levels and investigated the region of interest (ROI) that might allow for processing and/or transmitting less video data. In preliminary analyses, we observed strong correlations, but not adequately close relationships for clinical use. For this reason, we investigated additional imaging under near-infrared light, which we reasoned might provide more information for the construction of more clinically accurate image-based hemoglobin determinations. In this process, we estimated the hemoglobin levels by using a chromatic analysis of the fingertip's blood where the absorption properties of blood were captured under different wavelengths of light. Therefore, it is possible to determine the level of hemoglobin in tissue using near-infrared transmittance [97].

Hemoglobin content measurement means the quantity of hemoglobin in a given volume of blood. For non-invasive measurement, optical properties of living tissue have been used for the calculation of the difference in absorbance properties of blood constituents. The absorbance properties can be measured in transmissive and reflective mode where various wavelengths of light can travel through living tissues. We can measure the optical absorbance changes in the transmitted and reflected light. The variation of this transmitted or reflected light depends on the shape, volume, refractive index of hemoglobin, and angular distribution of scattered light, which characterizes the absorption properties of blood and tissue [98]. Analyzing these changes in optical scattering properties in tissues, we can build a non-invasive solution for hemoglobin estimation.

To investigate blood volumetric changes non-invasively, we generated photoplethysmogram (PPG) signals from fingertip videos. In this chapter, we describe the study of pixel intensity changes for different hemoglobin levels, dual wavelength technique for hemoglobin assessment, a novel approach based on dual wavelength's PPG signal, devices, PPG issues, our data collection protocol and the characteristics of the patient population we recruited.

6.1 Study of blood coloration

According to the Beer-Lambert law, the absorption of light is proportional to the concentration of a medium and the path length, given by:

$$I_o = Ie^{-\alpha CD}, \tag{6.1}$$

where I_o is the output light intensity, I is the incident light intensity, α is the light absorption coefficient, C is the concentration of a blood component, and D is the light path. In our case, the finger has three different absorptions for a wavelength of light (λ) due to hemoglobin (Hb), plasma (P), and tissue (T). So, the light absorption (under the light wavelength λ) by a finger is

$$I_{o,\lambda} = Ie^{(\alpha_{Hb}[Hb]+\alpha_P[P]+\alpha_T[T])(-D)} \tag{6.2}$$

Since our goal is to measure the concentration of blood hemoglobin as compared to that of blood plasma, we need to remove the response of the tissue. In this study, we aim to generate PPG signal using fingertip video where the AC and DC values of a PPG signal are created in every heartbeat. The light response for AC and DC value of a PPG can be given as:

$$AC_\lambda = Ie^{(\alpha_{Hb}[Hb]+\alpha_P[P])(-d_1)+(\alpha_T[T])-(D_T)}, \tag{6.3}$$

$$DC_\lambda = Ie^{(\alpha_{Hb}[Hb]+\alpha_P[P])(-d_2)+(\alpha_T[T])(-D_T)}, \tag{6.4}$$

where d_1 is the path length for Hb and plasma during AC signal, d_2 is the path length for Hb and plasma during DC signal, $d = d_1 - d_2$, and D_T is the path length for tissue. We assume the tissue has a stable response (Section 1.6), a ratio of AC and DC magnitude removes the effect of tissue. Then, we can express the ratio between the AC and DC values:

$$\frac{AC_\lambda}{DC_\lambda} = e^{(\alpha_{Hb}[Hb]+\alpha_P[P])(-d)}, \tag{6.5}$$

where d is the path length that affects only the hemoglobin and plasma for λ wavelength of light. Taking the log of both sides of the equation, we can write:

$$ln\frac{AC_\lambda}{DC_\lambda} = \alpha_{Hb}[Hb]d + \alpha_P[P])(-d), \tag{6.6}$$

The empirically measured absorption coefficient for each wavelength of light could help us to solve the Equation 6.6. However, the system setup for fingertip video recording, lighting conditions, PPG generation from fingertip videos, and complex reflection properties of tissue compel us to use machine learned regression techniques to calculate the ratio of hemoglobin and plasma. For a reliable prediction model, we have used a dual wavelength strategy where one wavelength of light is hemoglobin sensitive, and the other one is plasma sensitive.

Our second clinical study is based on photoplethysmography where the relative magnitude of a PPG signal is measured for different wavelengths of light [99]. Since we generate a PPG signal from a fingertip video, we could extract several PPG features to capture nonlinear interactions [6].

6.2 Dual wavelength technique

Dual wavelength selection techniques are used in several studies to estimate blood constituents. The ratio of the responses captured by two different wavelengths of NIR

lights were applied in different reviews where the PPG signal was obtained using commercial PPG capturing devices [100]. Several PPG features have also been utilized for blood hemoglobin [101], skin blood supply assessment [102], oxygenation level [103], and glucose level [104] estimation. For example, Wang et al. built a mobile application called HemaApp where they used multiple NIR lights and recorded fingertip video from a finger pad area [6, 37]. In the HemaApp, the NIR LED and the smartphone camera were on the same side since they used reflection oximetry. In the first version of HemaApp, the authors used the ratio of AC and DC components under different wavelengths of light. Later, they changed the data analysis approaches and used the ratio of AC and DC components calculated from red, green, and blue pixel intensities. In the third version of HemaApp, the authors recommended that NIR-based response from tissue might provide potential information to better estimate hemoglobin level non-invasively.

In living tissues, hemoglobin and melanin absorb in the 400nm-650nm spectrum, and other proteins absorb light in the violet and ultraviolet regions. A dominant tissue chromophore is water, which absorbs photons strongly around the 1000nm wavelength of light. The spectrum range from 650nm to 1100nm is known as the tissue optical window or NIR region. In the NIR region, light absorption is lower than the other spectral areas for oxy-hemoglobin and deoxy-hemoglobin. That is why the light sources including 850nm, 940nm, and camera light are considered as hemoglobin responsive. On the other hand, 1070nm wavelength NIR LED light is selected as plasma sensitive.

The calculation of hemoglobin concentration depends on the quantity of hemoglobin as well as plasma volume, in which it is suspended. A change in the relationship between plasma and total hemoglobin volume might strongly influence the hemoglobin concentration in disease states. For example, anemia is common in diseases such as cancer [105] and chronic liver disease [106]. In general, reduced hemoglobin concentration has been considered for those causes, albeit a low hemoglobin level also be

found during hemoglobin synthesis where total hemoglobin is normal if blood plasma is disproportionately expanded. This can happen because of disease-related changes are managed by the global water balance in our body [107].

Plasma and serum are part of blood where plasma contains serum and clotting factors. About 55% of total blood volume is plasma where 91% of the plasma is water. The red blood cells are 42% of blood volume. We aim to measure the concentration of hemoglobin as compared to the concentration of plasma in the blood. Hemoglobin measurement in the clinical setting is currently restricted to blood tests where blood is drawn for a complete blood count (CBC). Information about red blood cells (RBC), white blood cells (WBC), and platelets are calculated electronically in the CBC test [107]. After the blood draws in the clinic, the blood sample is diluted using potassium ferricyanide and potassium cyanide to oxidizes the iron to form methemoglobin, which is finally converted to hemiglobincyanide (HiCN). Since HiCN has a solid color and an absorbance maximum at 540 nm, the absorbance of the diluted sample at 540 nm is compared with absorbance at the same wavelength of a standard HiCN solution. Then the equivalent hemoglobin concentration is calculated. Using this method, the measured hemoglobin level is referred to as the gold standard or clinically-measured hemoglobin level (CHb) [108].

The non-invasive hemoglobin estimation system, unlike invasive CHb test, is a chemical-free process. To understand the ratio of blood hemoglobin and plasma non-invasively, we must use the specialized light sources that allow us to receive their response non-invasively. Since PPG signals can contain the biological properties of hemoglobin and plasma as an optical characteristic, analyzing the ratio of two PPG (one PPG is from hemoglobin response light , and another PPG is from plasma responsive light source) signals' features would allow us to estimate the blood hemoglobin levels non-invasively.

For the PPG generation, we can apply transmission oximetry on a finger where

infrared light is sent from the dorsal to ventral pad area, and we can capture the transmitted light in a video using a smartphone from the ventral pad side. The changes in a video are the pulsation of arterial blood. We can thus extract the Hb aspects in the PPG signal extracted from that videos. In addition, PPG signals can be created using reflectance oximetry where both light source and smartphone camera are on the same side. A fingertip video can capture the optical variation where the light response is changed based on the pulsation of arterial blood. We can extract these responses in the PPG signal calculated from the fingertip videos. Based on this idea, we employed six NIR LED lights and two white LED lights in each NIR LED board. These light sources transmit from the dorsal to the ventral pad area of a finger. The lighting surface area has a vital role in light penetration into the living tissue. A small lighting surface can penetrate a small part of the living tissue, whereas the planar lighting surface allows us to comprehend the light at a deeper level [109, 110]. Besides, we also captured the response of a built-in camera light of a Google Pixel 2 smartphone (reflectance oximetry) capturing the fingertip video without any external light source (NIR LED-board).

6.3 Novel Approach

We used transmission and reflectance oximetry to capture the responses from blood volume changes using a set of NIR LED lights. We built LED-boards with different wavelengths of NIR LED lights. The first LED-board incorporated six NIR light sources with a wavelength of λ_H and two white LED lights. We selected 850nm, 940nm, and built-in camera light as hemoglobin responsive (λ_H) and insensitive to any other blood components. We chose the 1070nm wavelength of light as blood plasma responsive (λ_P) where other blood constituents have no response or negligible response. Figure 6.1 (a) illustrates the use of a LED-board built with 850nm NIR LEDs and two white LEDs lights. and fingertip video and this video is used to generate hemoglobin responsive PPG signal. In Figure 6.1 (b), the PPG signal captures plasma response from

a fingertip video using a LED-board built with 1070nm NIR LED and two white LED lights.

We designed and developed three unique light sources in this study. First, we put six 850nm NIR and two white LED lights as shown in Figure 6.1a where this light source is defined as L_{850} in the following section. Second and third embodiments were built using similar technique which are defined here as L_{940} and L_{1070}. The NIR and white light of the LED-board were always turned on while recording the fingertip video. The light beam of a LED-board crossed from the dorsal to the ventral pad area of a finger experiencing transmission, scattering, and absorption in the intervening tissue and bone. The light beam exiting from the ventral pad side of a finger was captured in a video by a smartphone. A similar approach was used for the light source L_{940} and L_{1070} to record the data from a finger. In addition, we recorded fingertip videos using the Google Pixel 2's built-in camera light, defined as L_{Pixel2}, where no LED-board was attached with the finger (reflectance oximetry). The PPG generated from this video is also considered as hemoglobin responsive PPG signal.

The value of each PPG signal captured under different light sources (L_{850}, L_{940}, L_{Pixel2} and L_{1070}) are normalized by using the PPG features. For example, the AC component is divided by the DC component to get a normalized feature. The PPG signal generated using the light source L_{850} is defined as PPG_{850} and the normalized PPG feature values calculated from PPG_{850} is defined as R_{850}. Similarly, we can generate the normalized PPG features of PPG_{940}, PPG_{Pixel2}, and PPG_{1070}. The normalized value of a PPG signal cancels out the effect of tissue that we discussed in Equation 6.6. By calculating the ratio of hemoglobin-responsive PPG features and plasma-responsive PPG features (e.g., ratio of R_{850} and R_{1070}), a relationship can be generated which provides the information on the light absorbed by both hemoglobin and plasma. The ratio of R_{850} and R_{1070} for each subjects' PPG signal correlates against the known clinically measured hemoglobin values (Equation 6.7 and Figure 6.2). From

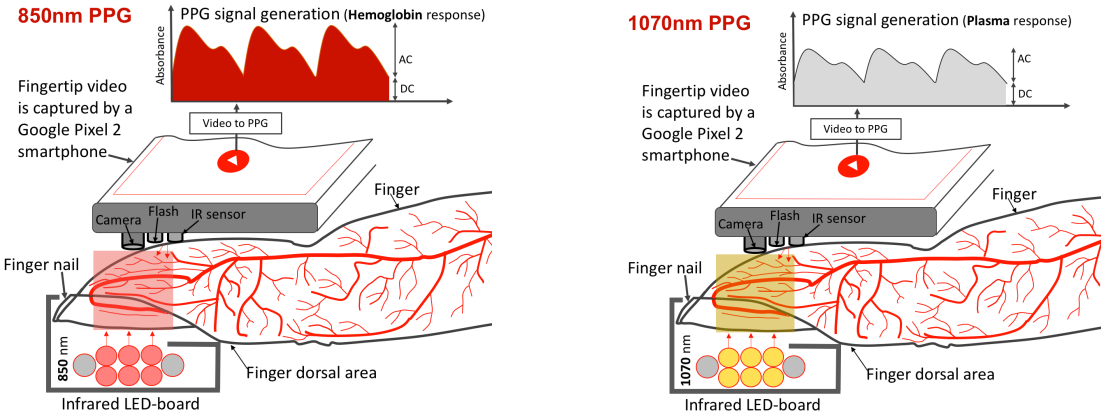

(a) Fingertip video is captured using 850nm NIR LED light board.

(b) Fingertip video is captured using 1070nm NIR LED light board.

Figure 6.1: A plot of captured light intensity recorded by a smartphone versus time (frame) where the graph is defined here as a PPG signal which is describing the modulation of light intensity by the changes in arterial blood volume with each heartbeat. a) Six 850nm near-infrared (NIR) LED lights are used to capture blood hemoglobin response. b) Six 1070nm near-infrared (NIR) LED lights are used to assess the blood plasma response.

this correlation, we can generate a mathematical model to estimate hemoglobin levels for future fingertip videos. As part of the PPG features, we consider systolic, diastolic, dicrotic notch peak values, relative augmentation of those peaks, area under the systolic peak and diastolic peak, a slope of each peak, and a relative timestamp value of the peak, etc. The calibration equation for a model can be given as,

$$HCb = K_1\frac{H_1}{P_1} + K_2\frac{H_2}{P_2} + K_3\frac{H_3}{P_3} + ... + K_n\frac{H_n}{P_n} \tag{6.7}$$

where CHb is the clinically measured hemoglobin levels, $K_1, K_2, ...K_n$ are the constant that should be calculated using machine learning algorithm, $H_1, H_2, ...H_n$ are the hemoglobin responsive PPG features, and $P_1, P_2, ...P_n$ are the plasma sensitive PPG features. We will analyze these ratios considering for other hemoglobin responsive PPG signals and compare the outcomes to identify the best hemoglobin responsive NIR light.

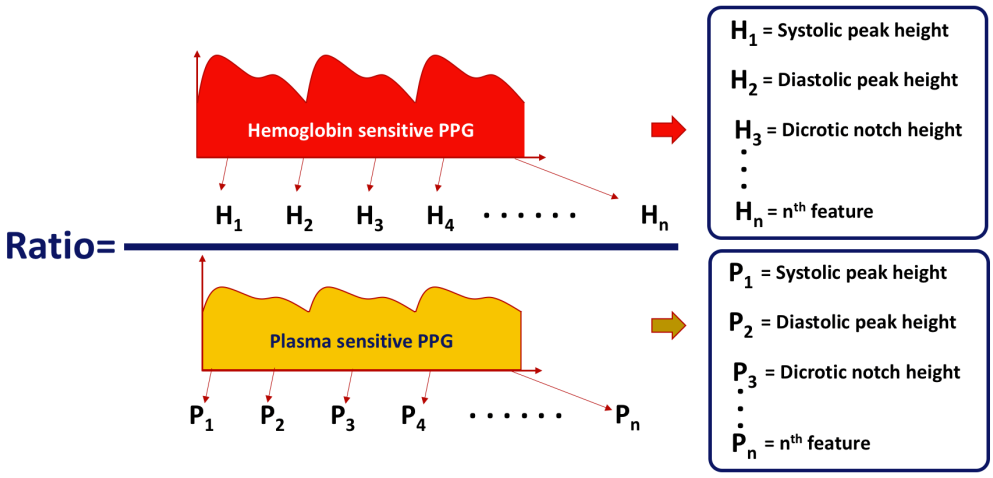

Figure 6.2: The ratio of two PPG signals captured under two different wavelengths of NIR.

6.4 Data Collection Processes Under Our Second Clinical Protocol and the Characteristics of This Second Study Population

The major goal of our second clinical protocol was to collect fingertip video data under multiple different lighting conditions. Other refinements from our first clinical study protocol included near-infrared LED light sources for fingertip video recording because the response of hemoglobin and plasma can be captured non-invasively using near-infrared light. This study was conducted on only a Bangladeshi patient population at the Amader Gram Breast Care Clinic in Khulna, Bangladesh. This research was approved by the Institutional Review Board (IRB) at Marquette University and by the Bangladesh Medical Research Council in Bangladesh.

Eligibility: Adults over age 18 and able to provide informed consent.

Inclusion Criteria: Volunteers must be in good health without any major life-threatening illness or acute illness and have clean and soft fingertips and have no nail polish or scrapes or damage to the skin on the fingertip.

Exclusion Criteria: Subjects who received a blood transfusion in the last three months were ineligible for this study.

6.4.1 Study design and procedures

- Step 1: A health assistant (HA) took the information about the subject. Then, the HA matched the inclusion criteria for the subject. If the person was eligible for the study and provided written informed consent, then the HA enrolled the subject for the data collection process. The listed subject was identified using a 4-digit ID number starting from 1001.

- Step 2: The HA stored the subject's ID, age, gender, and timestamps.

- Step 3: (a) The HA checked the NIR LED lights (whether it was on or off) before the data collection. (b) The HA used the primary camera of the smartphone for video recording where the patients were instructed to press gently and completely cover the camera using the ventral bed of the finger. In Figure 6.3, the orientation of a finger with a smartphone is presented where the smartphone is positioned vertically and the finger is put horizontally covering the camera and IR-sensor (Figure 6.3 (a)). The tip of the finger should cover the built-in IR sensor on the camera. The LED-board should put in such a way that the dorsal area of the fingertip faces NIR LED lights of the board (Figure 6.3 (b)). The subjects were instructed not to talk, move, or change finger position during the video recordings. (c) The HA then recorded a 10-second fingertip video using the smartphone under four lighting conditions:

  - The first video was captured using a Google Pixel 2 without any LED-board. The built-in infrared sensor of the smartphone was on for auto-focusing purpose since Android OS controlled the built-in IR sensor, and the smartphone camera light (known as flashlight) was turned on to illuminate the finger. This group of fingertip videos is named as $Videos_{Pixel2}$. This video was captured using reflective-mode pulse oximetry to compare

the hemoglobin prediction model's performance with the prediction model built using transmissive-mode pulse oximetery (two videos captured under 850nm and 940nm).

  - The second video was captured using a Google Pixel 2 and an 850nm LED-board where the LED-board IR and white light are on, but the smartphone camera light turned off. This group of these fingertip videos was named $Videos_{850}$.
  - The third video was captured using a Google Pixel 2 and a 940nm LED-board where the LED-board IR and white light was on, but the smartphone camera light turned off. This group of these fingertip videos was named $Videos_{940}$.
  - The fourth video was captured using a Google Pixel 2 and a 1070nm LED-board where the LED-board IR and white light are on, but the smartphone camera light turned off. This group of these fingertip videos was named $Videos_{1070}$.

- Step 4: After capturing fingertip videos, on the same visit, the subject provided a blood sample adequate for the determination of blood hemoglobin levels. These determinations were all made at a large volume diagnostic laboratory with standardized procedures.

- Step 5: The HA maintained the naming convention of each video captured by the smartphone and stored the blood test results in tabular format and the data were transmitted to Marquette University.

6.4.2 Data collection kit

The data collection kit included three LED-boards and a Google Pixel 2 smartphone as shown in Figure 6.3. The purpose of each item is illustrated in the following section.

1. **LED-board:** We built three LED-boards where each board had six similar infrared (IR) LED lights as shown in Figure 6.3 (b). One LED-board was built with six 850 nm NIR LED lights. The second and third LED-boards were developed with six NIR 940 nm and six NIR 1070 nm LED lights separately. Each LED-board had two extra white LED lights. A rechargeable battery powered each board and was put underneath the LED-board. The health assistant checked the LED-boards and the charge level of the battery before the data collection process. The rechargeable battery ran 2-3 days after one full charge.

2. **Google Pixel 2**: The Google Pixel 2 smartphone has multiple options to capture video. We use 60 frames per second (FPS) in the fingertip video recording process. We turned off the camera's auto rotate option so that all videos were recorded with a similar dimension. The Google Pixel 2 has a built-in 950nm infrared (IR) sensor which is always on by the Android operating system (OS).

6.4.3 PPG signal issues

In general, clean PPG signals are interrupted during the data collection process by finger movements, motion artifact, coughing, and gasp (Figure 6.4) [27].

We collected fingertip videos data from 212 subjects. Some patients' fingertip videos were not recorded properly or corrupted. Therefore, we could use only 167 subjects' data because of unclean PPG signal issues (Figure 6.4). The selected 167 persons' fingertip videos were chosen using the following criteria:

- The video had no issues such as random flickering and black shadow in the video.
- The video file was not corrupted, and had approximately the same memory size (a video produces about 50 MB (megabyte) file for 10-12 seconds of recording).
- A standard PPG signal has a systolic and a diastolic peak. The generated PPG signal from a video should follow a standard PPG signal (the video generated

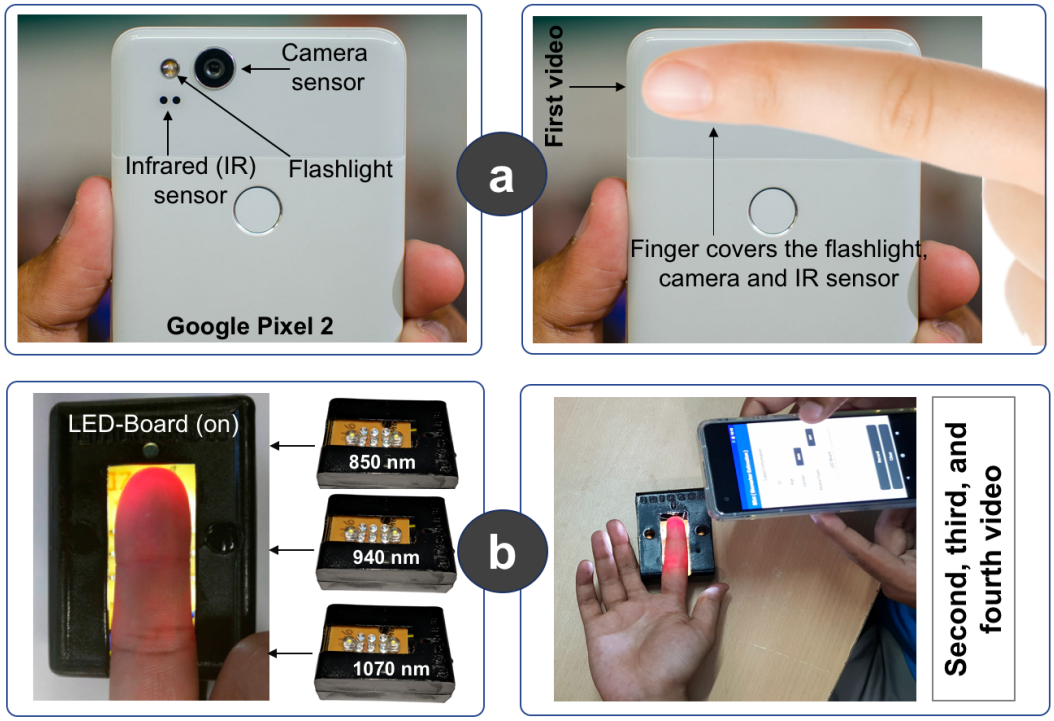

Figure 6.3: The fingertip video capturing modules. a) A fingertip video was recorded using a Google Pixel 2 where the video was captured without any LED-board. b) The rest of the (three) videos were recorded using the same Google Pixel 2 smartphone with an additional LED-board sequentially where three LED-boards were built with 850 nm, 940 nm, 1070 nm infrared (IR) LED lights.

PPG had both systolic and diastolic peak).

- Four videos of an individual satisfied the above mentioned criteria.
- The CHb level of the subject was available.

6.5 Patient Characteristics

We recruited 167 participants with usable data: 82 males and 85 females with an age range from 14 to 68 years and median age of 39 years. The maximum hemoglobin level was 13.0 $g\ dL^{-1}$, and the minimum hemoglobin level was 9.0 $g\ dL^{-1}$ with median hemoglobin level 11.2 $g\ dL^{-1}$. In this group, 22 individuals had high blood pressure, 35 subjects were diabetic, and 68 women were premenopausal.

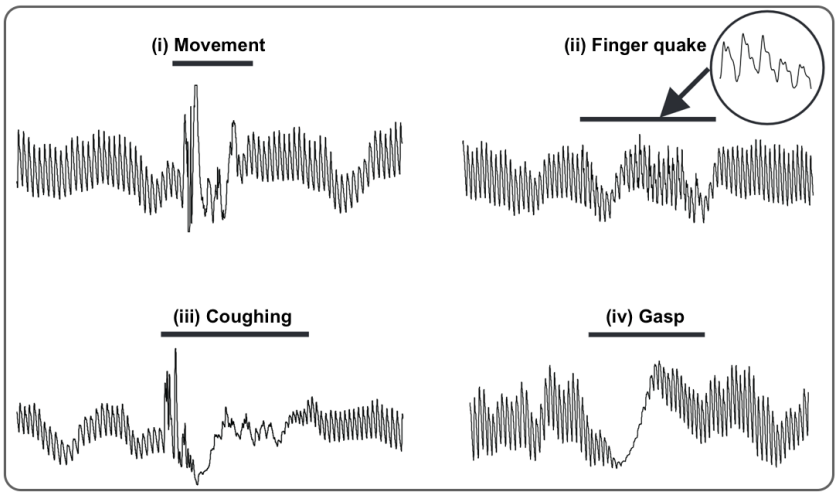

Figure 6.4: PPG signal issues due to the (i) body movement, (ii) finger quake, (iii) coughing and (iv) gasp (image is edited from [27]).

In Figure 6.5, the left-side of the figure shows a bar-chart for male subjects and the right-side presents similar information for female participants. Among 82 male individuals, only 16 subjects had a hemoglobin level higher than 12.5 $g\ dL^{-1}$. On the other hand, we had no female participants who had levels of hemoglobin above 12.5 $g\ dL^{-1}$. In general, the number of female subjects who had a lower level of hemoglobin is greater than that of male subjects.

6.6 Limitations

The current version of this study has a few limitations.

1. The user needs to change the LED-board to capture each fingertip video under a single wavelength of NIR LED light.

2. We should make a single LED-board with two sets of NIR LED-lights: hemoglobin responsive and plasma responsive NIR LED lights. Then, the end users do not need to change the LED-board for each video recording.

3. The LED-board should be easy-to-use.

4. A mobile application is necessary to indicate of finger movement and placement

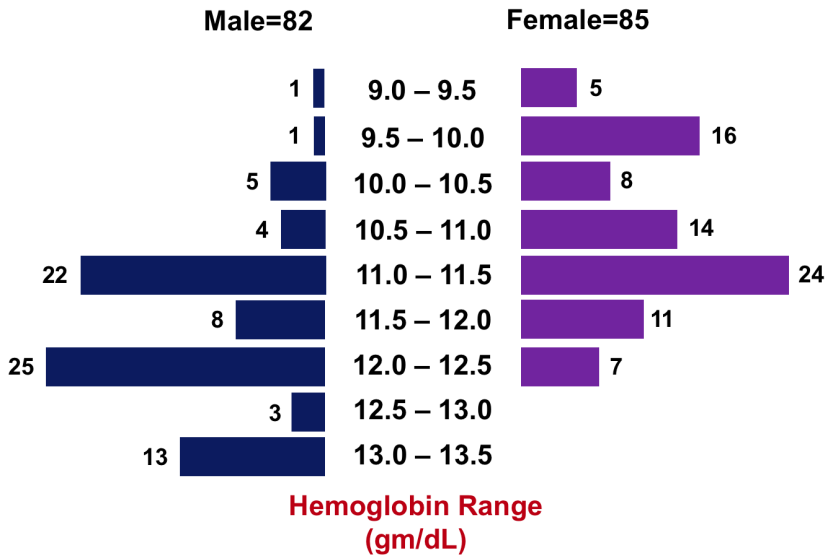

Figure 6.5: Hemoglobin level, age and gender information of 167 participants in the second clinical study at the AGB.

with data transmission functionalities to a cloud, receive the response from the cloud, and user-friendly interface.

Chapter 7

Prediction Model Development for Hemoglobin Assessment

In our second clinical study, described in chapter 6, we captured four fingertip videos ($Videos_{Pixel2}$, $Videos_{850}$, $Videos_{940}$, and $Videos_{1070}$) per person and secured usable data from 167 individuals. The Google Pixel 2 smartphone's primary camera captured each video with 1080×1920-pixel resolution. We used the following steps to process these fingertip videos.

7.1 Fingertip Video Processing

We extracted all frames from each fingertip video. Due to the potential for photo-bleaching, finger movement, and placement issues, we selected frames 201 to 400 for the data analysis. We subdivided each selected frame into a 10×10 block matrix where a single block contained 108×192 pixels of information (Figure 7.1). Each frame of the video had three two-dimensional pixel intensities arrays for each color: red, green, and blue (RGB). Since each frame had 100 blocks, a mean value was computed from each color pixel for each (108×192) block, which gives 100 mean values (Figure 7.1). During the pixel analysis, we observed that the red channel showed a stronger response under the NIR and white LED lights (LED-bard) a finding also reported in other studies [6]. Consequently, we considered only the red pixel intensity data to analyze our videos. In Figure 7.1, we represent 200 frames extracted from a fingertip video, which were subdivided into the 10×10 block matrix. Then, we generated a time-series signal (putting frame number on X-axis and averaged value of a block on Y-axis) from each of the blocks across 200 frames of a video (Figure 7.1).

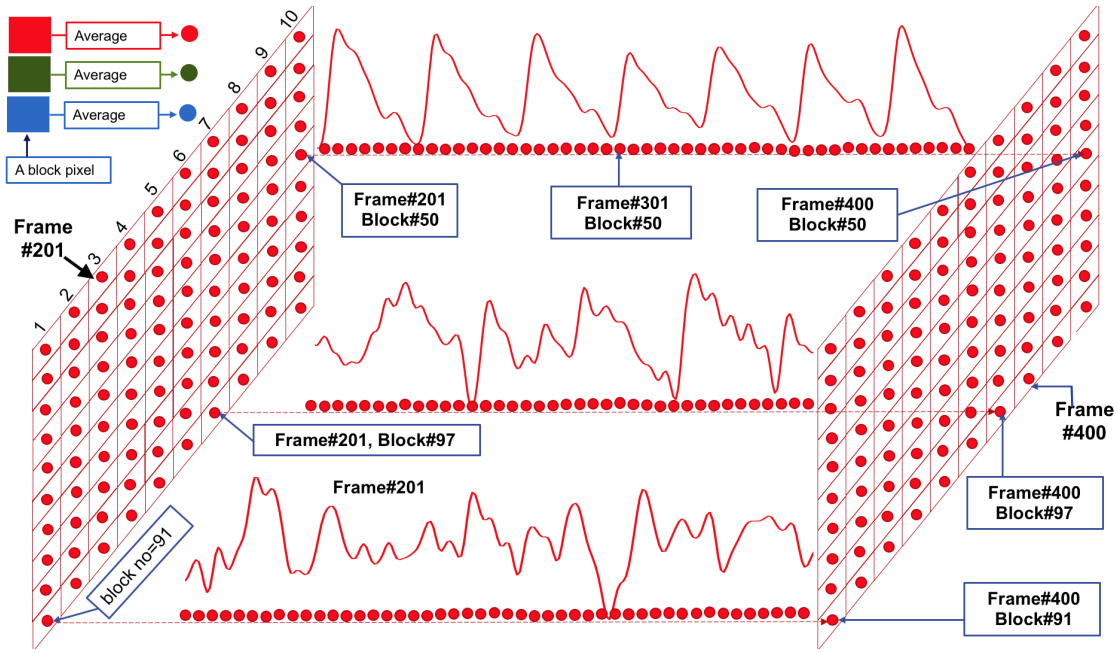

Figure 7.1: Subdivision of an image frame to generate multiple time-series signals.

7.1.1 PPG signal generation

In Figure 7.1, we represent three different time-series signals between the frame number 201 and 400 where the top signal was generated by block number 50, 91, and 97. We applied these following techniques on each time series signal for PPG signal generation:

- Apply a 2^{nd}-order Butterworth bandpass filter (0.66 Hz 8.33Hz) where a minimum cut off value was selected to discard the signal fluctuations due to breathing range from 0.2 to 0.3 Hz [6].

- Use the Nyquist frequency as half of the frame per second (FPS) (FPS/2), which is equivalent to 60/2=30.

- Select the filtered signal from the stable (with regular shape and cycle) part of the time-series and crop the signal as a PPG.

- Identify three PPG cycles which meet the inclusion criteria (e.g., each PPG cycle

has a systolic peak and a diastolic peak discussed in Section 6.4.3).

- If three continuous PPG cycles are not found, then select at least one cycle which has a systolic peak and a diastolic peak, replicate this selected cycle three times, and combine them to make a three-cycle PPG signal (Figure 7.2).
- Transfer this PPG signal (with three cycles) for the feature extraction process.

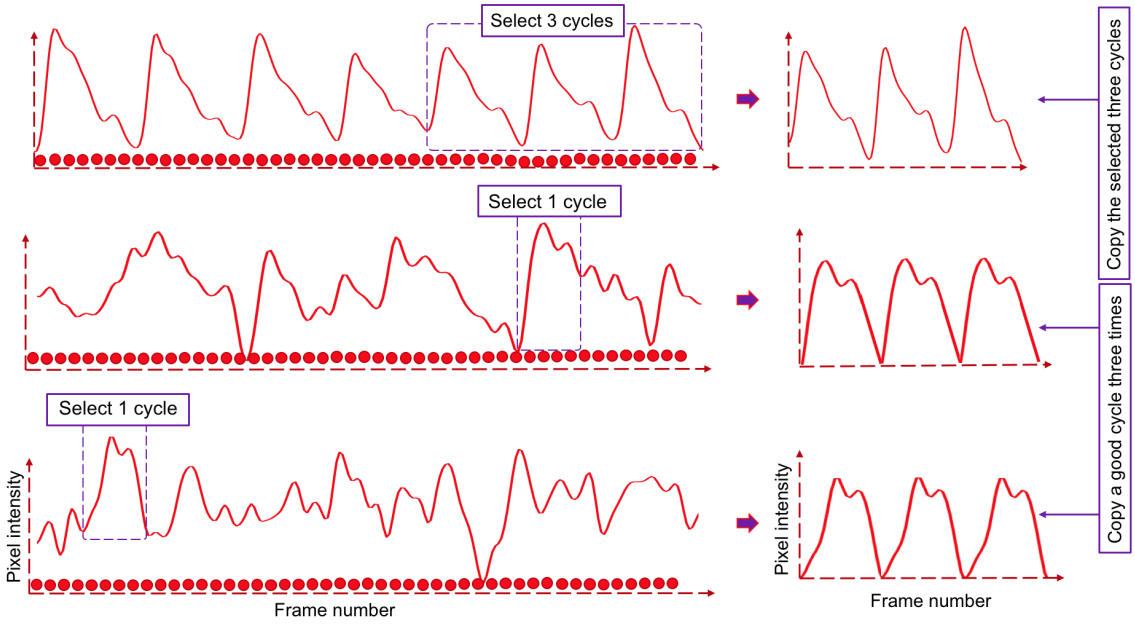

Figure 7.2: Photoplethysmogram (PPG) signal generation from a time-series signal.

To obtain the required PPG cycles without unwanted peaks and irregular cycles, we chose a specific area of a PPG signal using a semi-automated process where a Matlab code was used to represent several PPG signals of several (random) blocks. The Matlab code asked for a starting and an ending index number of a cycle that included a systolic and a diastolic peak in the time-series. We provided the index numbers of three PPG cycles if they were found consecutively; otherwise, we gave the input for one period. Three consecutive PPG cycles were stored together where a single PPG cycle was replicated three times to make an equal number of cycles for each block of a video. If a single cycle existed in multiple locations of a PPG signal, the cycle with a highest sys-

tolic peak was selected. If any block had no single PPG cycle that satisfied the selection criteria, we discarded that PPG signal without calculating its features (Figure 7.3).

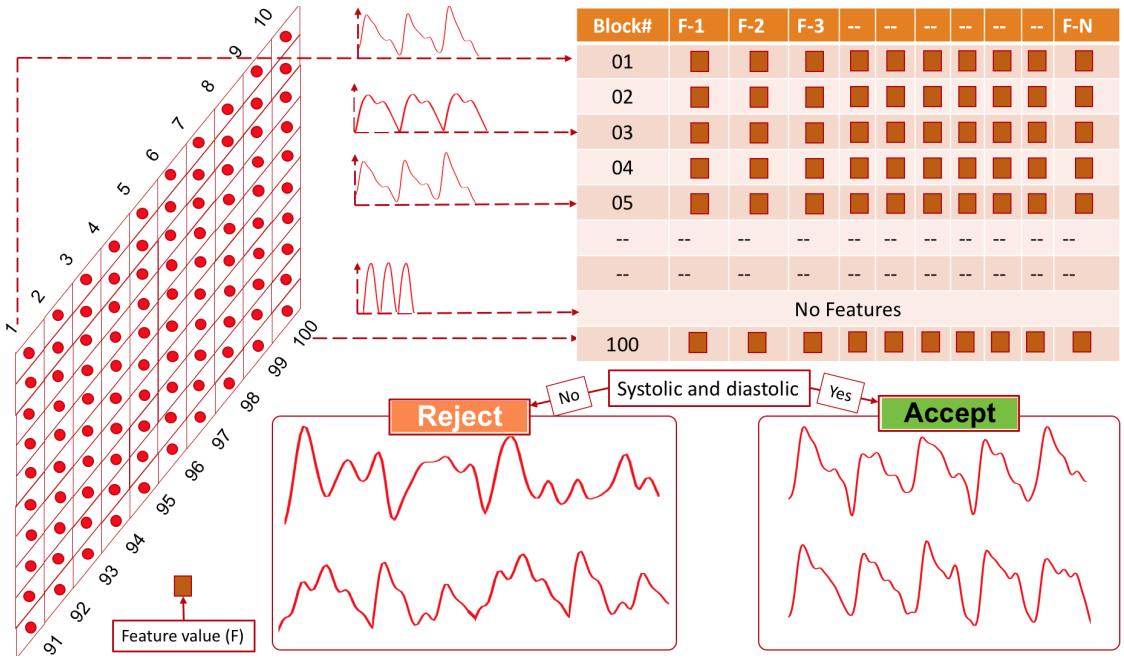

Figure 7.3: Feature generation from the Photoplethysmogram (PPG) signal generated in all blocks.

7.1.2 Regression technique

In our correlation development work (Chapter 4), we applied the Partial Least Squares Regression (PLSR), and we observed the PLSR worked better on a smaller sample size. However, it did not give us a global fit statistic for the generation of a prediction model [111]. In the PLSR, higher order PLS factors contained more detailed features for the regressors, which are correlated with the response vector (Y). Thus, a higher order of PLS components leads to a complicated prediction model. Again, a large number of PLS components cannot generalize a model well. Another critical problem with approximating latent variables is that the prediction model becomes inconsistent and biased since the predictive power changes with increasing sample size [112].

For dimensionality reduction, PLSR transfers data into latent variables to reduce

dimensionality, and then implement multiple linear regression on latent variables. This method does not perform well when predictions are required over an extensive range, where nonlinearity occurs. In that situation, a nonlinear regression model is highly relevant. Support Vector Machine Regression (SVR) is one of the popular nonlinear regression techniques [113]. SVR has several advantages over other regression algorithms. For example, SVR has a regularization parameter that helps to avoid the overfitting issue, which was one of the challenging parts of the PLSR. In addition, SVR uses the kernel where we can do the engineering of the kernel to characterize the problem. Since the computational complexity of SVR does not depend on the size of the input data, SVR provides excellent generalization features with higher prediction accuracy [114]. We trained our model using the SVR where Gaussian kernel was selected.

7.2 PPG Feature Generation

After generating the PPG signal from the smartphone-based fingertip videos, we calculated features from each PPG signal. In our case, we used three PPG cycles to evaluate the characteristics of each PPG signal derived from each block of a video (Figure 7.2). Previously, several studies used PPG features for determination of hemoglobin, glucose, blood oxygen saturation, heart rate, blood pressure [115], cardiac output [116], respiration, arterial disease, vascular aging (for assessing hypertension) [117], viscoelastic properties of blood vessels [118], the degree and length of vasodilatation, lower limb chronic venous insufficiency (CVI) [119], vasospastic (cold sensitivity condition), and autonomic function (migraine patients) [120].

Since a PPG signal reflects the blood movement from the heart to the fingertips through the blood vessels, the study of the characteristics parameter of a PPG signal may provide information on blood constituent levels. So, we investigated multiple features from the PPG signal (Figure 7.4) including the systolic and diastolic peak, PPG rise time, pulse transit time (PTT), pulse shape, and amplitude, etc. (Figure 7.4) [120].

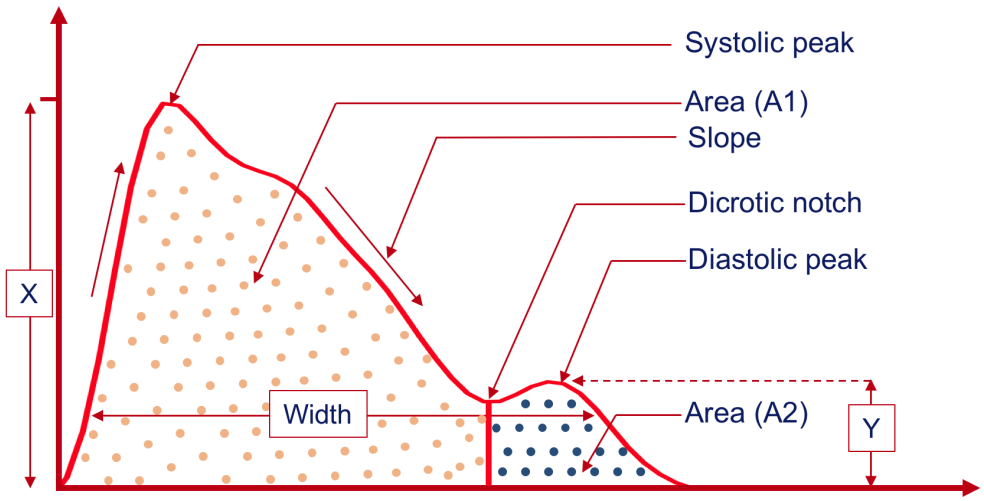

Figure 7.4: Multiple features collection from a Photoplethysmogram (PPG) signal.

Combining one or multiple PPG features, we produced different feature sets (datasets) where we employed SVR to create prediction models. Based on the predictive capacity of different models, we obtained ten features that provided the highest level of linear correlation. These ten features are presented (Figure 7.4 and Figure 7.5) in Table 7.1. A number of PPG features have been presented in the previous studies.

- Systolic peak (X): The systolic peak (X) is an indicator of the pulsatile changes in blood volume caused by arterial blood flow. The systolic peak is generated by the direct pressure wave coming from the left ventricle to the periphery of the body.
- Systolic peak (Y): The diastolic peak is found as a result of reflections of the pressure wave by arteries of the lower body [121]
- Dicrotic notch (Z): Dicrotic notch is a small downward deflection between systolic and diastolic point of a PPG cycle [122].
- Pulse Interval: The distance between the beginning and the end of the PPG waveform.
- Augmentation Index: The relationship between the contribution that the wave

reflection makes to the systolic arterial pressure, and the reflected wave coming from the periphery to the centre [120].

- First derivative of a PPG signal: PPG shows blood movement in the vessels. The first derivative of PPG gives the velocity of blood in the finger [123]. In Figure 7.5, a PPG sisgnal (top) and the respective first derivative of the signal are presented.

- Peak time: The ratio of a peak value and the sample rate is denoted as peak time.

Table 7.1: Ten selected features captured from a PPG signal to analyze the `AGB-167` dataset (Figure 7.4).

SL	Feature name
1	Systolic peak (X)
2	Diastolic peak (Y)
3	Dicrotic notch (Z)
4	Relative augmentation index 1: $\frac{X-Y}{X}$
5	Relative augmentation index 2: $\frac{Y-Z}{X}$
6	Time between systolic and diastolic peaks (T_1)
7	Ratio of two inflection point areas ($R_1 = \frac{A1}{A2}$)
8	Ratio of systolic peak time and pulse interval (R_2)
9	Ratio of dicrotic notch time and pulse interval (R_3)
10	First derivative of systolic peak (D_1) (Figure 7.5)

The systolic amplitude (X) indicates the pulsatile changes in blood volume resulted in arterial blood flow. If we measure the pulsatile changes, then a machine learning algorithm can correlate the pulsatile changes with blood constituent levels [124]. Delle et al. confirmed the inverse relationship between the middle cerebral artery peak systolic velocity and hemoglobin levels [125]. Aldrich presented a monitoring device for blood component concentrations that simultaneously measured light path and the absorbance of visible and/or infrared light under multiple wavelengths across the patient's different body site systolic and diastolic peaks. Analyzing different absorbance and light path lengths, the concentration of a particular blood component was inferred [126].

Diastolic peak information is important in the hemoglobin measurement process since the volume of venous and arterial blood in tissues remains constant during the diastolic phase. Thus, the light absorbance from both tissue and blood is stable. With the incoming arterial pulse in the systolic phase, the total light absorbance rises with the increase in arterial blood volume. We can measure the systolic increase by subtracting the diastolic baseline absorbance from the systolic peak absorbance [127]. The relative augmentation also allows us to capture these variations [6]. Inflection points can determine the minimum and maximum values of the PPG waveform [128]. To identify the location of a strong PPG signal of an image, the number of inflection points in the signal can be calculated [129]. According to current research on subjects' peripheral blood vessels, stress level on the vessel wall and elastic properties of the artery exponentially go down with an inflection point, and diameter exponentially goes up [130, 131]. Calculating the first and second derivatives of the PPG signals, we can study the informative inflection points more accurately. The change in blood volume can be tracked calculating the pulse interval, and the ratio of different peak arrival time [132]. For example, a ratio of pulse interval to its systolic amplitude can provide a measure of a property of a person's cardiovascular system.

Averaging the features

While we calculated the PPG features from 100 blocks of a video, we averaged these features to make one observation from one video. To build a model, we created 167 hemoglobin-responsive observations and a similar number of plasma-responsive observations. Figure 7.6 shows the concept of how each observation set was created.

Ratio of PPG features

We computed the ratio of features captured from two PPG signals under two different wavelengths of light (λ_H and λ_P). The ratio of two PPG signals' feature values can be

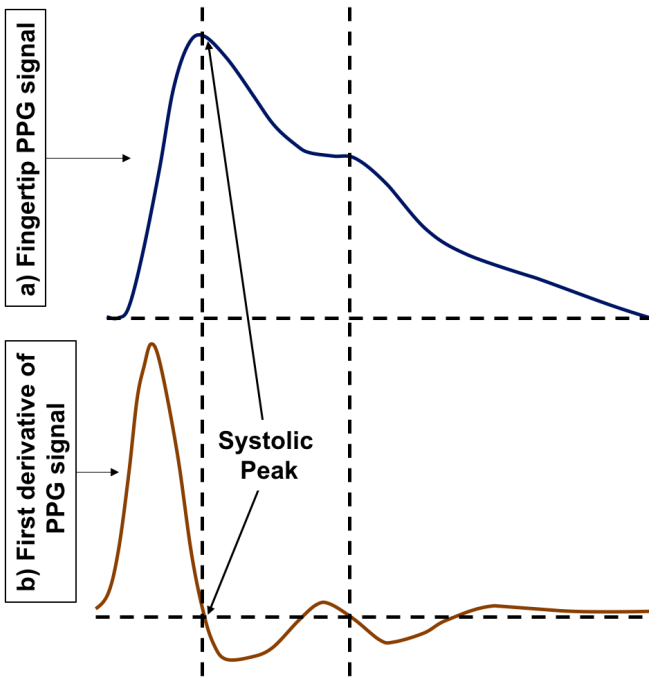

Figure 7.5: PPG signal a) Original b) first derivative of the original. The image is redrawn from [120].

presented as follows:

$$R_{1070}(850) = \frac{PPG_{850}}{PPG_{1070}} \tag{7.1}$$

The ratio of two PPG feature values means the individual ratio between each feature values. For example, we calculated the ratio of the systolic peak value under a 850nm NIR light and the systolic peak value under a 1070nm NIR. Similarly, we also measured the ratio of all other features that were applied to the SVR machine learning algorithm. The ratio of PPG signals' features are named as $R_{1070}(940)$, $R_{1070}(Pixel2)$ where

$$R_{1070}(940) = \frac{PPG_{940}}{PPG_{1070}} \tag{7.2}$$

$$R_{1070}(Pixel2) = \frac{PPG_{Pixel2}}{PPG_{1070}} \tag{7.3}$$

where PPG_{Pixel2}, PPG_{850} and PPG_{940} are hemoglobin responsive and PPG_{1070} is considered as plasma responsive PPG signal.

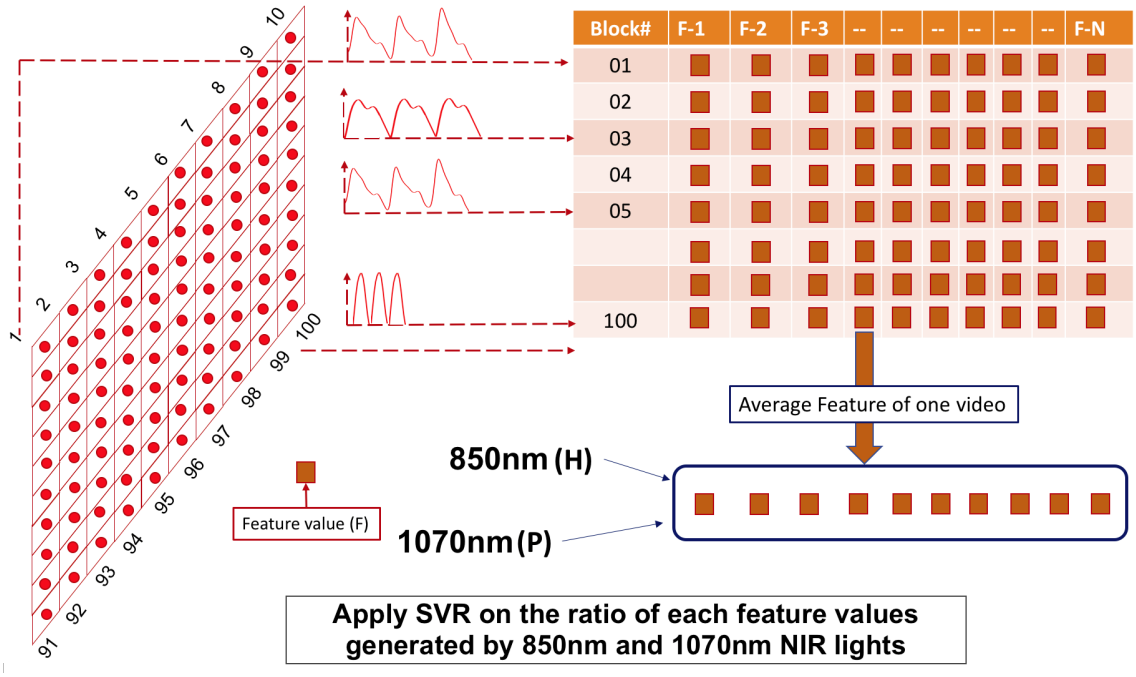

Figure 7.6: Features captured from 100 blocks are averaged for each video.

7.3 Results

In this data analysis, we employed the Support Vector Machine Regression (SVR) to build the hemoglobin prediction model using 10 PPG features. In this work, we applied SVR to three feature sets created from the $R_{1070}(850)$, $R_{1070}(940)$, and $R_{1070}(Pixel2)$.

7.3.1 Prediction models

Applying the SVR on the features generated from the ratio $R_{1070}(850)$ (Equation 7.1), $R_{1070}(940)$ (Equation 7.2), and $R_{1070}(Pixel2)$ (Equation 7.3) separately, we trained prediction models which are named as $Model_1$, $Model_2$, and $Model_3$ respectively. We tested those 167 subjects' features on the prediction model $Model_1$. Without separation of cases, the same total dataset was applied for testing purposes also. The regression line based on CHb levels and the estimated hemoglobin values using $Model_1$ are presented in Figure 7.7. In Figure Figure 7.7a, we observed that the Mean Absolute Percent-

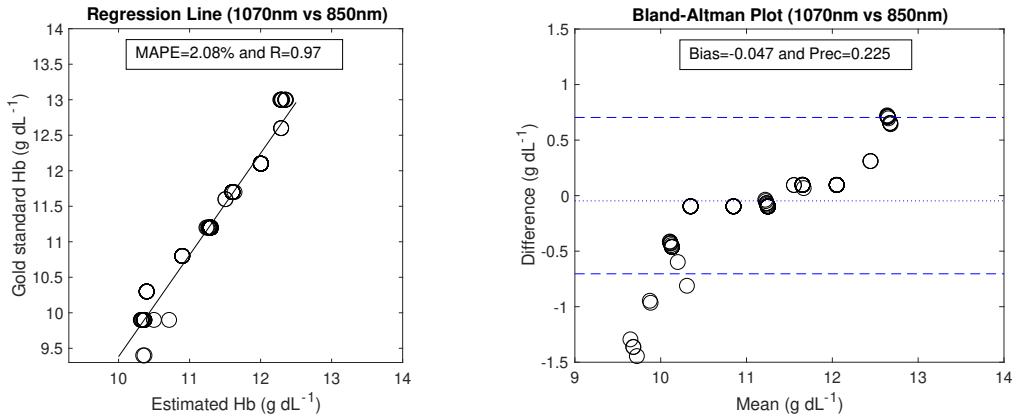

(a) Regression line. (b) The Bland-Altman plot.

Figure 7.7: Data analysis on the AGB−167 dataset using $R_{1070}(850)$ to estimate hemoglobin levels. a) The regression line based on the clinically measured hemoglobin levels and the estimated hemoglobin values using $Model_1$ b) The Bland-Altman plot is presented for 167 subjects' estimated hemoglobin levels using $Model_1$.

age Error (MAPE) was only 2.08% where the linear correlation coefficient (R) between clinically measured hemoglobin (CHb) levels and model predicted hemoglobin levels is 0.97. In Figure 7.7b, we present the Bland-Altman plot for those estimated hemoglobin levels where the bias and precision obtained were -0.047 and 0.225 respectively.

Using $Model_2$, we tested the features generated from the ratio $R_{1070}(940)$ on the prediction model. Figure 7.8 presents the regression line based on CHb levels and the estimated hemoglobin levels ($Model_2$). In Figure 7.8a, we observed that a Mean Absolute Percentage Error (MAPE) of 2.31% and the linear correlation coefficient (R) between CHb levels and model predicted hemoglobin levels was 0.96. We present the Bland-Altman plot in Figure 7.8b where the bias and precision were -0.034 and 0.251 respectively.

For $Model_3$, Figure 7.9a shows that the Mean Absolute Percentage Error (MAPE) is 2.26% and the linear correlation coefficient (R) between gold standard (clinically measured) hemoglobin levels and model predicted hemoglobin levels is 0.93. Figure 7.8b presents the Bland-Altman plot. Here, we the values of bias and precision were -0.039 and 0.246 respectively.

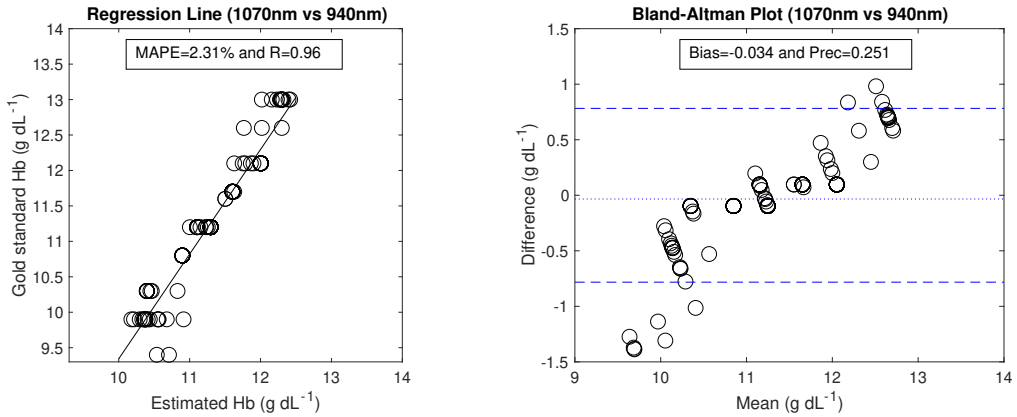

(a) Regression line. (b) The Bland-Altman plot.

Figure 7.8: Data analysis on the AGB−167 dataset using $R_{1070}(940)$ to estimate hemoglobin levels. a) The regression line based on the clinically measured hemoglobin levels and the estimated hemoglobin values using $Model_2$ b) The Bland-Altman plot is presented for 167 subjects' estimated hemoglobin levels using $Model_2$.

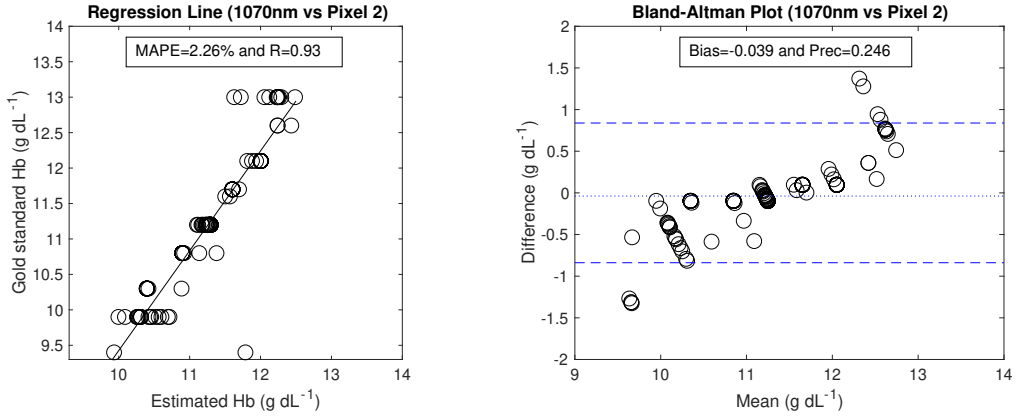

(a) Regression line. (b) The Bland-Altman plot.

Figure 7.9: Data analysis on the AGB−167 dataset using $R_{1070}(Pixel2)$ to estimate hemoglobin levels. a) The regression line based on the clinically measured hemoglobin levels and the estimated hemoglobin values using $Model_3$ b) The Bland-Altman plot is presented for 167 subjects' estimated hemoglobin levels using $Model_3$.

7.3.2 Training and testing sets

Analyzing three different datasets of 167 subjects, we observed that the features from the ratio $R_{1070}(850)$ showed a higher level of accuracy. Thus, we further investigated this dataset where we cross-validated the SVM regression model using 10-fold cross-validation. Here, we obtained the mean square error (MSE)=0.88. Afterwards, we investigated the PPG features ($R_{1070}(850)$) by subdividing the dataset into two sets: training and testing. We created these two datasets where the subjects were chosen with different levels of hemoglobin in each set. The training set was manually selected to include the full range of CHb. The training set included data from 133 individuals' data which comprised 80% of the 167 records. The testing set used the remaining data from 34 subjects. We applied SVR to train the prediction model using the training set, not taking into account the testing set. The created model was named $Model_T$, which was used to predict the estimated value for the training and testing dataset later. Using $Model_T$, the estimated hemoglobin values for the training set is presented in Figure 7.10a. For the training set, we found that the MAPE was 0.74% and R was 0.98. The bias and precision were -0.045 and 0.221 respectively (Figure 7.10b).

We also used the prediction model, $Model_T$ to predict the estimated value for the testing dataset. The estimated hemoglobin values for those 34 subjects is presented in Figure 7.11a. For the testing dataset, we found that the MAPE was 5.45% and R was 0.84. The bias and precision were -0.114 and 0.475 respectively (Figure 7.11b).

7.3.3 Region of interest (ROI)

In Chapter 5, we investigated five different locations (LCA, RCA, TRA, BRA, and CIA) of an image where a group of blocks generated each location's time-series signal. Similarly, we produced a PPG signal averaging the PPG signals from each block-group to build a hemoglobin prediction model in the second clinical study. For example,

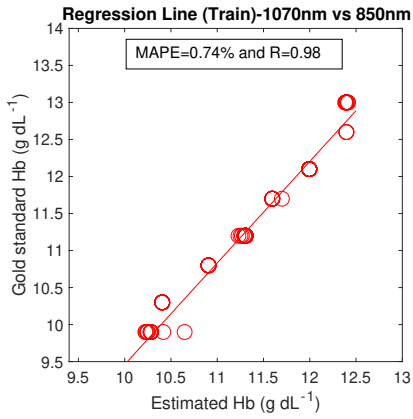

(a) Regression line.

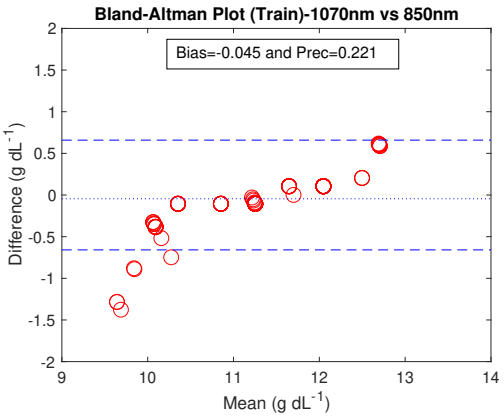

(b) The Bland-Altman plot.

Figure 7.10: Data analysis on the features of the training set generated from $R_{1070}(850)$ to estimate hemoglobin levels. a) The regression line of the training dataset based on the clinically measured hemoglobin levels and the estimated hemoglobin values using $Model_T$ b) The Bland-Altman plot is presented for the training set subjects' estimated hemoglobin levels using $Model_T$.

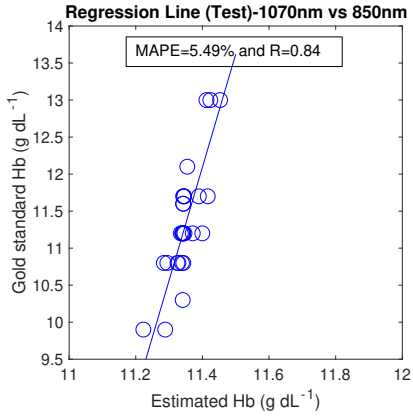

(a) Regression line.

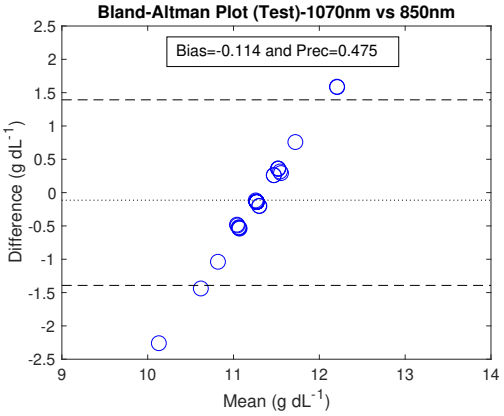

(b) The Bland-Altman plot.

Figure 7.11: Data analysis on the features of the testing set generated from $R_{1070}(850)$ to estimate hemoglobin levels. a) The regression line of the testing dataset based on the clinically measured hemoglobin levels and the estimated hemoglobin values using $Model_T$ b) The Bland-Altman plot is presented for the testing set subjects' estimated hemoglobin levels using $Model_T$.

LCA has 30 blocks including the block numbers 1, 2, 3, 11, 12, 13, 21, 22, 23, 31, 32, 33, 41, 42, 43, 51, 52, 53, 61, 62, 63, 71, 72, 73, 81, 82, 83, 91, 92, and 93. We averaged the PPG signal information for each group. Since the ratio of two PPG features generated from 850nm and 1070nm provided a strong linear correlation (R), we considered these two videos per person to investigate an ROI. Analyzing the ratio of two PPG features (under 850nm and 1070nm) from five locations, we observed that the PPG signals generated from the LCA provided the greatest R-value with minimum MAPE. However, the PPG signals generated from the RCA also showed better linear correlation. In Table 7.2, we present the performance of the PPG signals generated from other locations. Note that, we considered the red pixel intensities to generate a PPG signal since the PPG signals generated from green and blue pixel intensities have an irregular cycle and random peaks.

Table 7.2: Region of interest (ROI) identification analyzing five locations of an image considering the datasets captured under 850nm and 1070nm.

Location	**MAPE**	**R**
LCA	2.06%	0.96
RCA	2.18%	0.96
TRA	2.20%	0.95
BRA	2.20%	0.95
CIA	2.19%	0.95

7.4 Discussion

The photoplethysmogram (PPG) signal has been extensively studied over the past 15 years where multiple PPG features have been applied to build non-invasive solutions for hemoglobin assessment [6, 37, 99, 40]. However, these solutions have shown moderate performance with unreliable results due to complex data collection and analysis processes, with small sample sizes, and expensive additional devices. In this study, we used a regular smartphone and low-cost LED-boards (add-on) for the data collection,

applied image processing techniques for PPG signal generation and feature extraction, and analyzed 167 subjects' data for hemoglobin level assessment. We found that our prediction model outperforms the existing solutions: HemaApp (R=0.82) and Masimo Pronto 7 (R=0.81) [6].

7.4.1 PPG signal

PPG signals have been obtained by using PPG devices where the users are required to pay for this external device. In addition, they have to carry this item to use it remotely. For example, Ahmet et al. used an STM32F103xC ARM-based PPG data-acquisition card where the PPG signal was captured by a reflection sensor to estimate hemoglobin level non-invasively [101]. In this study, we developed the image processing techniques to generate PPG signal from a fingertip video captured by a smartphone. This solution provides a solution with twofold benefits: no additional cost or transport inconvenience.

In smartphone-based PPG signal generation, most of the solutions considered either the central region or a specific area of an image, which was averaged based on red, green, or blue channel pixel intensities. For example, HemaApp used the center section of an image where they cropped half the width and half the height of the image and averaged the intensity for each channel in the hemoglobin level estimation process [6]. For further examples, Scully et al. used 50×50 size image pixel intensities on green channel [40] and Jonathan took a central region with 10×10 pixels' mean intensity value for smartphone-based PPG generation [91]. We proposed to subdivide an image into a 10×10 image block and identify the best location for a strong PPG signal. We did not use any fixed location of an image since the best ROI might be changed from its original location based on finger position. Based on the ROI, we processed and transferred the minimum block area of an image, which reduces computing time and resources.

We generated PPG signals from green and blue pixel intensities, however we ob-

served several sharp spikes or zero values in these generated PPG signals that made them unreliable for feature extraction and prediction model development. Several studies have reported that the red pixel intensities have shown strong responses in the PPG signal generation process [6, 5].

Motion artifact, finger pressure on the smartphone camera and finger position are common challenges in smartphone-based PPG generation from fingertip videos. In our second clinical study, one health assistant recorded all fingertip videos considering standard finger pressure and position on the smartphone. To remove the finger movement, position, and pressure artifacts, we processed each time series signal using band-pass Butterworth filter. We used the Savitzky–Golay filter to PPG signal for the purpose of smoothing the data. In our second clinical study, the hemoglobin tests were performed in a single diagnostic center.

7.4.2 Hemoglobin level estimation

The PPG signal acquired by a fingertip video allowed us to build a model for predicting actual blood Hb levels. Here, we constructed a prediction model of Hb levels using the training dataset where we included 167 subjects' $R_{1070}(850)$ dataset. The linear correlation between the computed Hb content and the CHb levels shows an excellent R-value. From the Bland-Altman analysis, we compare the two Hb measurement methods where the 95% limits of agreement (LOA) exclude 12 out of 167 (7.18% outside the limits of agreement) with a bias of 0.04 g dL-1.

We applied the SVR on the remaining datasets. Figure 7.8a shows that the LOA includes 152 estimated Hb values with bias of 0.034 g dL-1, while the R value is equal to 0.96. For the $R_{1070}(Pixel2)$ dataset, Figure 7.9a shows that the LOA includes 154 estimated Hb values with bias of 0.039 g dL-1, while the R value is slightly reduced to 0.93. Even though the $R_{1070}(Pixel2)$ dataset results in a poorer performance, the correlation coefficient (R) is not much different from the other two cases, which sup-

ports the novel idea that we can estimate close to a clinically accepted hemoglobin level under two wavelengths of NIR LED light. The $Videos_{Pixel2}$ were captured without any LED-board. However, the Google Pixel 2 smartphone has a built-in infrared-red sensor (Figure 6.3), which may affect the captured fingertip video to enhance the correlation (R).

The PPG features of $R_{1070}(850)$ dataset shows the highest level of correlation with minimum MAPE and bias, which corroborate a reliable hemoglobin prediction model. For developing the hemoglobin quantification algorithm, we selected 133 individuals (80%) to use as a training dataset. To create a new testing dataset, we employed the rest of the individuals from the data group of 167. Since the sample size is relatively small, the testing dataset of only 34 individuals (20%) strengthens the validation of the non-invasive hemoglobin prediction model. The performance of ($Model_T$) on the training dataset is significantly better than other models where MAPE=0.74%, R=0.98, and LOA exclude 5 out of 134 (7.52% outside the limits of agreement) with a bias of 0.04 g dL-1. Even though the testing dataset with 34 observations results in a relatively poorer result (MAPE=5.49%, R=0.84, and bias=0.11 g dL-1.), testing results still supports the underlying idea that the fingertip-video-based PPG features can be used for accurately and precisely estimating Hb levels.

To make a comparison with PLSR, we computed prediction models applying PLSR on the dataset created by the $R_{1070}(850)$ where we use 10, 15, 20, and 25 PLS components and we obtained MAPE=5.75%, 5.70%, 5.65% and 5.50% and R=0.50, 0.51, 0.52, and 0.53 respectively. Since PLSR worked better on smaller sample sizes, we observed this effect on this new dataset of 167 subjects (`AGB-167`). In SVR, kernel function provides important support that has motivated its use in many studies. The Gaussian kernel (RBF) is known as the best kernel for its superior performance in several practical applications [133]. In this study, Gaussian kernel outperformed PLSR-based hemoglobin prediction models on the `AGB-167` dataset. In our second clinical

study, many women participating had high blood pressure, and or diabetes. Our prediction model may behave with less accuracy in these physiological situations.

For the prediction model to perform accurately on patients over a wide range of smartphone devices, demographic and physiological characteristics, the data training model should cover as wide a range of hemoglobin levels as possible [99]. It is essential for the prediction model that the data should be collected under different patient situations that might change the PPG signals and their features. Additional conditions such as temperature, physical fitness, interfering chemical agents–medicines may affect the hemoglobin prediction model.

In the first clinical study, we used Google Nexus 4 smartphone for the data collection process where the built-in camera light was turned on continuously during fingertip video recording. No additional lights were used for a fingertip video recording. In contrast, we used Google Pixel 2 smartphone for fingertip video recording and three different near-infrared LED light boards were used separately. We did not combine these two different protocols' datasets for the analysis purpose since these data sets have other differences.

7.4.3 Region of interest (ROI)

In the results section, we presented the ROIs where the PPG provided strong linear correlation coefficient (R) with minimum MAPE. We investigated the reason for better performance by the PPG signals generated in the LCA and RCA area. To understand the pixel intensities variations, we present 15 consecutive frames of a fingertip video using a colormap where the fingertip videos were captured under 850nm LED-board. In Figure 7.12, we show the colormap of 15 continuous frames where each frame contains the frame number in the middle of the colormap. The dotted area on the left side of each image in Figure 7.12 represents the LCA. Here, each frame has 10×10 block matrix where each block has averaged (red) pixel intensities. The color bar is presented

using blue color for the lowest value of a block and dark red color for the highest value of a block. Comparing these 15 colormaps, we observe that the highest color pixel variations were captured in the LCA where the PPG signals captured most of the PPG features. We also noticed that the blocks in RCA changed more than the remaining three locations for 15 frames. Later, we combined the PPG signals generated from LCA and RCA and analyzed the PPG features using the SVR algorithm where we observed the similar linear correlation (R=0.97) value that we calculated using all blocks PPG signals. Using this approach, we reduce the feature area of an image which might be helpful for the data transmission process between a smartphone and a cloud computer under low bandwidth internet.

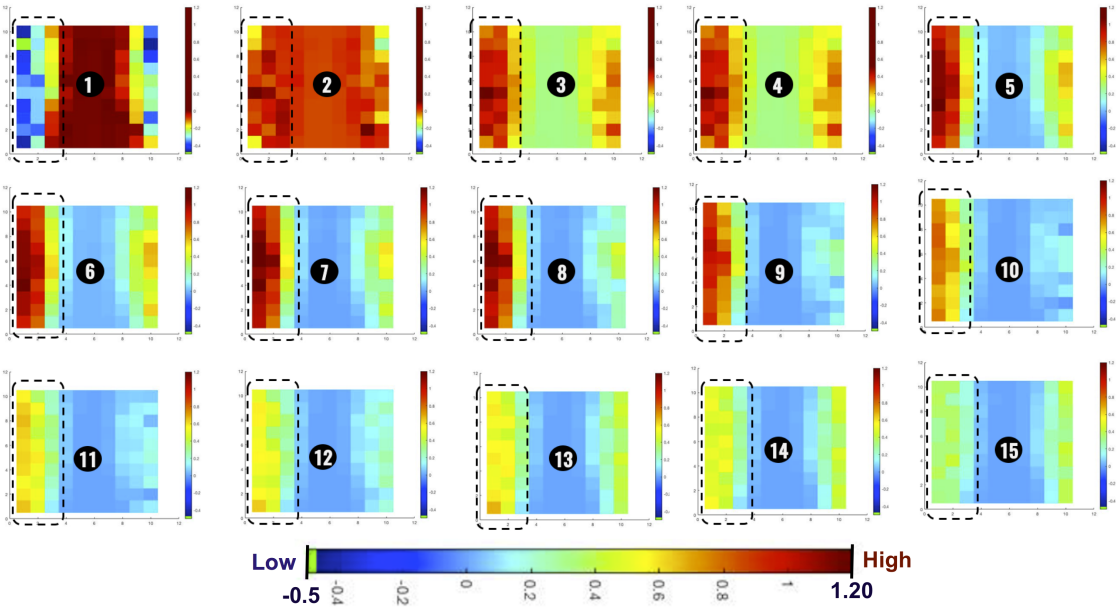

Figure 7.12: Features captured from 100 blocks are averaged for each video.

Although our novel image processing techniques provide a significantly better prediction model, we faced several challenges during the device development, data collection, and video processing. In the future, we recommend pursuing ideas in the following areas. First, we should explore using an LED-board with a different wavelength range of NIR LED lights. This may be important not only for stable fingertip video recording

but also for user protocol compliance. Second, a mobile application should be very user-friendly to ensure optimal end transmission capability, on-screen feedback with visual interpretation, cloud-based solution, and smartphone-based prediction model to support the users without internet access. Third, we need data collection from much larger and variable populations to build an optimally robust and clinically acceptable prediction model.

7.5 Conclusion

In this chapter, we have presented a non-invasive hemoglobin level assessment process using the PPG signal generated from a fingertip video, which was captured using a smartphone under near-infrared LED light. Analyzing the fingertip videos, we found a model using data from 850nm and 1070nm wavelength of NIR LED lights showed a significant correlation between the estimated and clinically measured hemoglobin level. In this study, we investigate the region of interest area which will help us to reduce the computing and data transmission time. This kind of smartphone-based non-invasive solution can improve health care services using existing infrastructure.

Chapter 8

Conclusions

In clinical settings, blood hemoglobin (Hb) assessment is a common and very clinically useful procedure. However, it is often challenging for many patients to have such testing. That is why the demand for noninvasive, real-time, and continual Hb measurements are increasing. To overcome the challenges, we did a first study to investigate the correlation between the computed hemoglobin using fingertip video pixel intensities and CHb level. To reduce the computing task, we studied the regions of interest in the fingertip video. In a second clinical study, we have collected more videos under different near infrared lighting conditions to capture blood volume changes using PPG features. We generated the PPG signal from fingertip videos captured by a smartphone, which provide the basic building blocks for prediction model development. This smartphone-based POC solution is a novel approach due to its key features including mobility, low-complexity, and affordability particularly in resource-limited or remote health care settings.

8.1 Principal Contributions and Findings

The principal contributions of the reported work are:

1. Development of a low-cost, reliable, portable, and user-friendly POC solution for hemoglobin assessment.

2. Design and implementation of a data collection protocol where a smartphone and NIR LED-boards are used.

3. Generation of block-wise PPG signal generation from a fingertip video captured by a smartphone.

4. Reduction of feature space using a ROI of a video data.

5. Identification of image processing techniques for PPG signal generation, which include video processing, image segmentation, filtering, and feature engineering.

6. Invention of a novel feature set generation from PPG signals to build a prediction model for hemoglobin assessment.

7. Provision of a hemoglobin assessment solution for a widely available device–a smartphone—without significant additional costs.

8. Development of a near clinically usable solution for noninvasive hemoglobin measurement.

The principal findings of the dissertation are:

1. It is possible to build a smartphone-based POC tool for hemoglobin assessment.

2. PPG generation is possible from a fingertip video applying image processing techniques.

3. Our proposed theoretical foundation for non-invasive hemoglobin estimation is able to generate feature matrices using the ratio of two different PPG signals' features.

4. Ourd prediction model outperform the existing non-invasive solutions for hemoglobin assessment: HemaApp and Masimo Pronto 7.

5. The model using the transmissive, illuminate at 850nm and 1070nm, appear to provide the best non-invasive measurement of Hb.

These contributions provide the basis for the development of a clinically accurate and widely applicable noninvasive tool, which achievement seems now possible as will be considered below.

8.2 Limitations of the Work Reported Here

Our approach relies on fingertip videos to create PPG features. The limitations of this approach are:

- We used two different near-infrared wavelengths of LED light in two different LED-boards and installed two white LED lights for the illumination of a fingertip. Such a data collection LED board is not perhaps an optimal design. Since two types of NIR LED lights were set up on two LED-boards, users need to change boards for each video. A better design will have the required NIR LED lights installed on a single board so that the user can record a video with a time lag between two videos (first one video –hemoglobin responsive and second one – plasma responsive).

- The investigated LED-board is a prototype. If the LED-board is not set up properly under the finger, the smartphone camera cannot be aligned with the LED-board. The captured video will have issues with lighting conditions. An operationally logical hardware package needs to be developed considering these and other issues.

- The mobile application is not developed for fingertip video recording with critical capabilities such as the identification of fingertip pressure level, and body movement.

- We collected data from 212 subjects in our second clinical study. These subjects did not provide laboratory hemoglobin levels covering the full range of such levels seen in patients—approximately 6 to 18 $g\ dL^{-1}$.

- A cloud computer-based solution is important for future validation purposes using crowedsourced fingertip video.

- We need image processing techniques to consider the video captured by any smartphone device.

8.3 Future Works

Near-infrared (NIR) spectroscopy is a promising technique for noninvasive Hb level estimation. We believe that a clinically accurate and acceptable model can be developed based on the work reported here if we can create acceptable signal-to-noise ratios and rigorous signal processing techniques, and analyze larger data sets from patients with the full range of hemoglobin levels seen in clinical practice. We suggest that pursuing the following strategies is likely to lead to definition of a more accurate and very acceptable clinical prediction model.

Low signal-to-noise ratios (SNR) of generated PPG signals influence the accuracy of prediction models [55]. PPG with reliable SNRs extracted from pulsatile arterial blood may reduce the relative error in PPG selection and feature extraction. Further, spectral properties of the NIR LED and the selective absorbance of some wavelengths in living tissue (fingertip) may lead to low transmitted intensities and decreased SNRs of PPG data. We can utilize laser diodes (LDs) as a light source in future work to improve the SNR. In addition, we can improve the PPG generation techniques. High-quality PPG signals are the key prerequisite for an improved hemoglobin prediction model [134]. We should explore building a PPG generation algorithm using the ratio of superimposition averaging template and pulse wave [135], optimized differential extraction method [134], dynamic spectrum method [136], and spectral difference coefficient and dynamic spectrum [137].

Because the pressure of the fingertip-pad on the smartphone camera and finger movement can alter the waveform of the PPG signal, a well-designed hardware system for securing the imaged finger needs to be developed [138, 139].

Noise and artifacts can be further reduced by using filters. For example, we can use

the moving average filter [140] and adaptive filters that work with a reference signal. The reference signals can be obtained from an additional transducer to identify finger movement [141]. Most of the physiological signals are non-stationary and change their properties over time. In this case, a wavelet transformation and the smoothed pseudo-Wigner–Ville distribution can be applied to improve the PPG signals [140]. The Wavelet transform has been used as a method of movement artifact reduction for PPG signals [142].

We have demonstrated a non-invasive solution for hemoglobin assessment where the dataset included hemoglobin levels from 9.0 to 13.0 $g\ dL^{-1}$ with most frequent (mode) Hb level 11.2 $g\ dL^{-1}$. The prediction model based on this dataset may be affected by algorithmic bias which made contribute to increased MAPE=2.08% (lowest MAPE) for the $R_{1070}(850)$ dataset. One way to remedy considered biases may be to train the prediction model using specific data from clinical populations with lowest and highest possible levels of hemoglobin. Taati et al. observed improved performance using this approach for their models adding various new faces from the older adults and dementia group [143]. Retraining their models with new images of older adults' faces improved their performance significantly (NRMSE $\leq 5\%$ and the accuracy moved from 72.0% to 90.2%).

We designed and implemented three NIR LED-light sources. In our clinical study, the researcher assistant changed each LED-board per fingertip video. A compact LED-board with multiple wavelengths of NIR LED can be built which may better standardize data from each separate light source.

Hemoglobin level estimations from capillary and venous blood, as done in our work, may differ. Conflicting results have been reported. Leppanen et al. found equivalent hemoglobin counts in fingertip compared to venous blood [144]. Two studies have reported no significant differences between finger-stick and venous samples [143]. Several studies have reported an overestimation of Hb levels by capillary, compared

with venous blood samples [145]. In contrast, Yang et al. found a significantly higher hemoglobin count (2.7%) in venous than in arterial blood [146]. These authors suggested that 2–3% of plasma in the arterial blood may come from supplemental tissue fluid. Since capillary blood has an arterial source, Hb levels may be higher than in venous blood [147]. Hemoconcentration in capillaries may cause this higher level of Hb [148]. Loop capillaries are the main source of blood from finger-pricks. With this technique, the Hb blood concentration changes with skin temperature, depth of skin penetration by the pick and dilution by extracellular tissue fluid due to skin pressure [149]. In summary, it is possible that in our work we are essentially assessing hemoglobin levels from the same individuals, at the same time, but in physiologically different samples-arteriolar/capillary and venous, but whether in usual clinical circumstances, these samples have different hemoglobin levels is unclear.

Based on the proposed solution, we propose a general conceptual framework which can be used for the assessment of other blood constituent levels. We describe the architecture of the framework here.

8.4 Concept: A General Framework for Non-invasive Smartphone-based Assessments of Blood Constituent Levels

The Hb system processing and analytic framework may be the basis for development of noninvasive POC tools for the assessment of multiple other blood constituents. The framework performs the hemoglobin level prediction in the cloud while relying on widely available consumer device (smartphone) to capture and transmit the data. In a broader concept framework, the user first inputs his or her credentials to record his or her fingertip video and submit a request to estimate the hemoglobin level. The full process is a non-invasive diagnosis process where the mobile application records the data collection device name, brand, version of the operating system (OS) along with other credentials. When the user submits a request, the system uses a prediction model algo-

rithm based on the particular smartphone. The calculated hemoglobin level is sent back to the user's display with some interpretation of the value using visualization tools such as cartoons, plots, and scores. The users can use this application on both mobile and desktop-based system using their credentials. The framework provides the user with this diagnosis (smartphone or desktop computer) device as a personalized POC tool.

Summarizing this concept: In our framework design process, the smartphone's camera sensor and a NIR LED-board act as a POC diagnostic tool. The key features of this framework include the following:

- The smartphone application is used to capture a 10-second fingertip video with the support of a built-in camera and an infrared (IR) LED-board.
- User authentication, video processing, feature extraction from each video is done in the cloud.
- The prediction model based on the user's credentials and mobile phone's technical specifications is deployed on the cloud.
- A parallel computing paradigm is activated if multiple requests arrive from several users to save the computation time.
- Security and privacy are maintained in data storage, transmission, and distribution.
- External software developers are allowed to participate in prediction model development, interface design and implementation, and run the code on any dataset without hampering the regular processing if user requests.

A traditional blood component estimation system receives the input sample from the user's data, preprocesses the data, extracts features, applies machine learning algorithm on the features, predicts the biomarker level, and returns the calculated result to the

users mobile or desktop application with a meaningful interpretation using numerical and graphical representation.

8.4.1 User interface:

A mobile application (app) with an appropriate acronym app name, can be available on the web to download and install. Multiple brands of smartphones can be supported. The specification of the mobile phone will be automatically stored in the local memory while installing the app. A user-friendly interface can be developed where the application will run on mobile and desktop systems. The user interface will allow the user to complete the registration process with minimum input and without cognitive demands. When the user completes the registration process, the user's credentials and the specification will be transferred to the cloud. A unique identification (ID) number (which is not human readable) will be created based on the user's information and the personal information which are encrypted before storing in the database. The ID number will be used to keep track of all the transmitted and distributed data for the verification purpose. The ID will be based on the user's registration time, age, gender, and smartphone's specification where a secure hash algorithm 1 (SHA-1) will be applied to generate a unique ID.

After the installation process, the user can capture a 10-second fingertip video using a smartphone and a NIR LED-board. The NIR LED-board should be made simple so that it is easy to attach to the finger. The index finger is preferable for capturing the video. If the index finger does not fulfill the criteria, then other fingers that are easy to put on the smartphone camera will be chosen for video recording. The mobile app can guide the user to put their fingers correctly on the camera using a green light indication. If the user places the finger on the smartphone camera with normal pressure, without any movement, and with correct position, then the green indicator light on the app will tell the user that the app is ready to start the video recording. We can also automate the

recording process when the green indicator light is on so that users do not need to put their finger on the video recording button. The app will turn off the recording after a 10-second duration and ask the user whether they are ready or not to send the data to the cloud. Based on the internet connection, the user can save the data or send the data immediately to the cloud for further processing and wait for the feedback. If the user's internet bandwidth is high, then the video will be transferred to the cloud. Otherwise, a selected number of frames will be transferred for slow internet connection.

The feedback of cloud computing will be presented numerically as well as with visuals. The interpretation of the result will be easy to understand for a minimally literate person. The result can be saved in or deleted from the local memory of the phone, but the result will be stored in the cloud permanently. The interface will allow the user to see the previous hemoglobin levels, and statistics based on the selected duration. The same smartphone can be used for different users where each user should log in with their credentials.

8.4.2 Cloud computing

In the cloud computing system, we can transfer the high computation processes from smartphones to the cloud [150]. Dedicated resources such as distributed file storage, multiple core computing system, and higher memory can be applied for the video and image processing task if needed in the cloud. Parallel computing allows us to use faster computing facilitates to handle millions of users' fingertip video [151]. The cloud computing architecture is shown in Figure 8.1 and is illustrated here step by step.

1. The user authentication process will confirm the validation of a user's credentials. If the authentication process fails, the user will get feedback from the cloud.

2. After the validation process is completed, the fingertip video is stored in temporary memory in the cloud and waits for the subsequent processing. The cloud

will preprocess the video first where the frames will be extracted and checked for further processing.

3. If the generated frames are not appropriate with the selection criteria, a negative acknowledgment will be sent to the user to send the video again. Otherwise, the user will receive a message regarding successful video recording and data transmission.

4. Based on the number of user requests, additional servers will be added in the cloud, the execution of each prediction algorithm will be tracked, and the prediction model will be updated.

5. When a user uses this application for the first time, the cloud system will request for a clinically measured hemoglobin value of that user. So, the user should provide several clinically measured hemoglobin values (3-5 times per month) to the cloud for calibration purpose.

6. After the preprocessing, the video will be transferred to a Job Manager where the manager assigns a video as a new job to a scheduler.

7. After receiving a job from a Job Manager, a Task Manager assigns the necessary resources to complete the job. In the cloud, the task manager can assign distributed file system and parallel computing facilities to accomplish the job efficiently.

8. The prediction models in the cloud are classified according to the user's race, age, gender, and other factors such as diseases, physiological features, etc. To build an area-based prediction model, we may keep the location information with the user's permission.

9. Feature engineering process will be performed by the research scientist implementing new ideas, editing existing data analysis policies, testing the developed

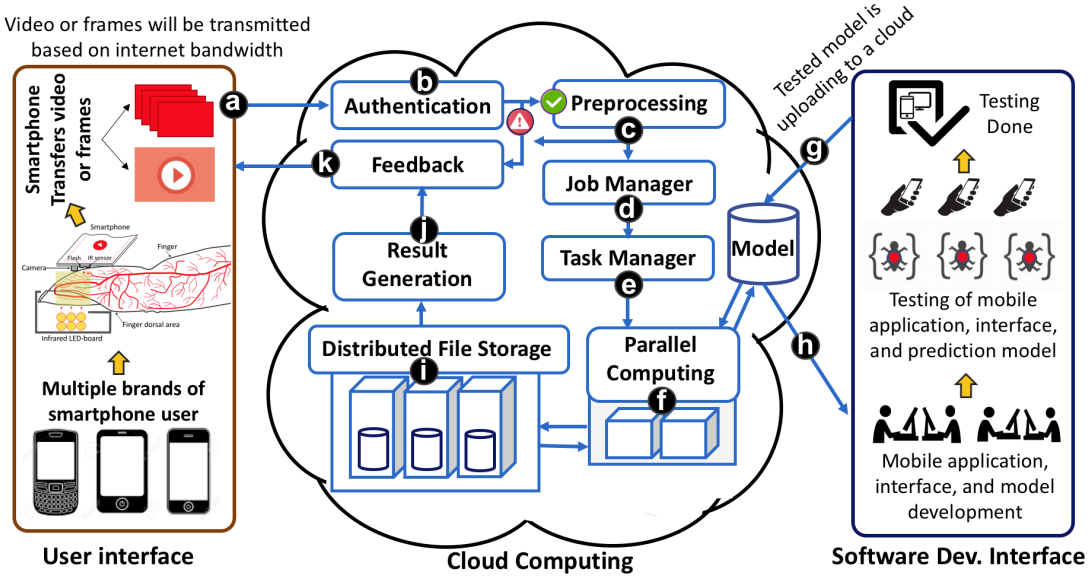

Figure 8.1: Framework blood constituent level estimation using a smartphone and infrared LED lights.

processes and uploading those facilities in the cloud.

10. In the cloud, a virtual machine will be installed to run the advanced algorithm and prediction model.

8.4.3 Software development interface

In the virtual machine of the cloud, the implemented algorithms will be deployed by the software developer. The updated mobile application and desktop-based applications can be made available on the app storage and web server. The development team will build a job manager that will manage the upcoming fingertip videos, put in the job queue, select the algorithm, and send to a task manager [152]. The task manager will be developed with several properties including scheduling task, task execution, managing task input-output queue management, and parallel resource allocation if needed.

Initially, the development interface can be built as a virtual machine on a desktop computer and run a similar type of virtual machine on the cloud which will make it easier for the programmer to deploy the code without any technical challenge. The freely

available Virtual Box can be used here, and the image processing tools and API can be made available [152]. A web interface will be developed to manage the algorithms, programming code, database, prediction model, a large number of users, software developers, crowdsourced fingertip videos, and accessibility. Several administrative and user levels will be created to keep control over the whole software system.

The developer team can download any model to test and edit the prediction model algorithms. Then the algorithm and software applications will be tested by other teams. The new or updated model can be uploaded to the cloud after the testing and validation processes as shown in Figure 8.1.

8.5 Published work

The published peer-reviewed journal, patent application, and articles based on this dissertation are listed here.

8.5.1 Peer Reviewed Articles

1. Hasan, M. K., Haque, M. M., Adib, R., Tumpa, J. F., Love, R. R., & Sheikh, I. A. (2018). Smarthelp: Smartphone-based hemoglobin level prediction using an artificial neural network. In *AMIA Annual Symposium Proceedings* (Vol. 2018, p. 535). American Medical Informatics Association.

2. Hasan, M. K., Love, R. R., & Sheikh, I. A. (2019). "Method and Apparatus for Non-invasive Hemoglobin Level Prediction", Provisional Patent Application No. 62/638,630 **Patent** Pending.

3. Hasan, M. K., Haque, M., Sakib, N., Love, R., & Ahamed, S. I. (2018). Smartphone-based human hemoglobin level measurement analyzing pixel intensity of a fingertip video on different color spaces. *Smart Health*, 5, 26-39.

4. Hasan, M. K., Sakib, N., Love, R. R., & Ahamed, S. I. (2017, October). RGB pixel analysis of fingertip video image captured from sickle cell patient with low

and high level of hemoglobin. In 2017 *IEEE 8th Annual Ubiquitous Computing, Electronics and Mobile Communication Conference (UEMCON)* (pp. 499-505). IEEE.

5. Hasan, M. K., Sakib, N., Field, J., Love, R. R., & Ahamed, S. I. (2017, July). A novel technique of noninvasive hemoglobin level measurement using hsv value of fingertip image. In 2017 *IEEE 41st Annual Computer Software and Applications Conference (COMPSAC)* (pp. 221-229). IEEE.

6. Ahsan, G. M., Gani, M. O., Hasan, M. K., Ahamed, S. I., Chu, W., Adibuzzaman, M., & Field, J. (2017, July). A novel real-time non-invasive hemoglobin level detection using video images from smartphone camera. In 2017 *IEEE 41st Annual Computer Software and Applications Conference (COMPSAC)* (Vol. 1, pp. 967-972). IEEE.

7. Hasan, M. K., Sakib, N., Love, R. R., & Ahamed, S. I. (2017, October). Analyzing the existing noninvasive hemoglobin measurement techniques. In 2017 *IEEE 8th Annual Ubiquitous Computing, Electronics and Mobile Communication Conference (UEMCON)* (pp. 442-448). IEEE.

8.5.2 Poster Presentation

The presented posters based on this dissertation are listed here.

1. **Md Kamrul Hasan**, Md Hasanul Aziz, Richard R. Love, Sheikh I. Ahamed. Smartphone-based Bioimaging for (Hemoglobin) Biomarker Estimation. Poster presented at the Forward Thinking Poster Session and Colloquy; 2018 Nov 27; Marquette University, Milwaukee, WI.

2. **Md Kamrul Hasan**, Richard R. Love, Sheikh I. Ahamed. NICE HELP: Non-Invasive Computational Evolution (NICE) for Hemoglobin Level Prediction (HELP).

Poster presented at the IEEE Conference on Biomedical and Health Informatics (BHI) 2018; 2018 March 4-7; Las Vegas, NV.

3. **Md Kamrul Hasan**, Anmol Paudel, Richard R. Love, Sheikh I. Ahamed. ProPar HELP: Programming in Parallel (ProPar) for Hemoglobin Level Prediction (HELP). Poster presented at the IEEE Conference on Biomedical and Health Informatics (BHI) 2018; 2018 March 4-7; Las Vegas, NV.

4. **Md Kamrul Hasan**, Jordan Trinka, Michelle A. Visbal Onufrak, Md Munirul Haque, Young L. Kim, Sheikh Iqbal Ahamed. Develop a Conversion Matrix Using Hyperspectral and RGB Data for Noninvasive Hemoglobin Level Measurement. Poster presented at the Forward Thinking Poster Session and Colloquy; 2017 Nov 28; Marquette University, Milwaukee, WI.

5. **Md Kamrul Hasan**, Nazmus Sakib, Joshua Field, Richard R. Love and Sheikh I. Ahamed: BILD (Big Image in Less Dimension): A Novel Technique for Image Feature Selection to Apply Partial Least Squares Algorithm. Poster presented at the 2017 IEEE Great Lakes Biomedical Conference (GLBC); 2017 April 06 - 07; Milwaukee, WI.

6. **Md Kamrul Hasan**n, Nazmus Sakib, Joshua Field, Richard R. Love and Sheikh I. Ahamed: A Novel Process To Extract Important Information From Invisible Video Captured by Smartphone. Poster presented at the 2017 IEEE Great Lakes Biomedical Conference (GLBC); 2017 April 06 - 07; Milwaukee, WI.

7. **Md Kamrul Hasan**, GM Tanimul Ahsan, Amit Kumar Saha, Sheikh I. Ahamed, Richard R. Love: Noninvasive Hemoglobin Level Measurement Using Spectroscopy. Poster presented at the 40th IEEE Computer Society International Conference on Computers, Software & Applications (COMPSAC); 2016 June 10-14; Atlanta, GA.

8. GM Tanimul Ahsan, **Md Kamrul Hasan**, Sheikh I. Ahamed. Non-invasively Hemoglobin Level Measurement Using a Smartphone. Poster presented at the Forward Thinking Poster Session and Colloquy; 2015 Dec 1; Marquette University, Milwaukee, WI.

9. GM Tanimul Ahsan, **Md Kamrul Hasan**, Duc Do, Mohammad Adibuzzaman, Sheikh I. Ahamed. Analysis of Mini Video Images from Cellphone Camera for Hemoglobin Level Assessment. Poster presented at Computational Sciences Symposium; 2015 April 21; Marquette University, Milwaukee, WI.

BIBLIOGRAPHY

[1] David J Weatherall. The inherited diseases of hemoglobin are an emerging global health burden. *Blood*, 115(22):4331–4336, 2010.

[2] Ann Chen Wu, Leann Lesperance, and H Bernstein. Screening for iron deficiency. *Policy Statement*, 2016.

[3] Chi Huu Hong Le. The prevalence of anemia and moderate-severe anemia in the us population (nhanes 2003-2012). *PloS one*, 11(11):e0166635, 2016.

[4] Kathryn L Hassell. Population estimates of sickle cell disease in the us. *American journal of preventive medicine*, 38(4):S512–S521, 2010.

[5] Nam Bui, Anh Nguyen, Phuc Nguyen, Hoang Truong, Ashwin Ashok, Thang Dinh, Robin Deterding, and Tam Vu. Pho2: Smartphone based blood oxygen level measurement systems using near-ir and red wave-guided light. In *Proceedings of the 15th ACM Conference on Embedded Network Sensor Systems*, page 26. ACM, 2017.

[6] Edward Jay Wang, William Li, Doug Hawkins, Terry Gernsheimer, Colette Norby-Slycord, and Shwetak N Patel. Hemaapp: noninvasive blood screening of hemoglobin using smartphone cameras. In *Proceedings of the 2016 ACM International Joint Conference on Pervasive and Ubiquitous Computing*, pages 593–604. ACM, 2016.

[7] cercacor.com. Hemoglobin, retrieved in 2018 from http://www.cercacor.com/ember-hemoglobin-accuracy.

[8] Biosense. biosense: adding value to life. retrieved in August 4, 2011 from http://sites.google.com/site/biosenseglobal/touchb.

[9] Tima Chansanchai. *Imagine Cup World Finals 2014 winner Eyenaemia receives $50,000 and a private session with Bill Gates*, retrieved in Aug 2014 from https://blogs.microsoft.com/firehose/2014/08/01/imagine-cup-world-finals-2014-winner-eyenaemia-receives-50000-and-a-private-session-with-bill-gates/.

[10] Website information. *Noninvasive Hemoglobin Monitor, SMART-Hb*, retrieved in Jan 2019 from http://tech4lifeenterprises.com/smart-hb/.

[11] Website information. *SpHb: Continuous SpHb provides real-time visibility to changes, or lack of changes, in hemoglobin between invasive blood samples*, retrieved in Jan 2019 from http://www.masimo.com/technology/co-oximetry/sphb/.

[12] Moon Jung Kim, Quehn Park, Myung Hee Kim, Jeong Won Shin, and Hyun Ok Kim. Comparison of the accuracy of noninvasive hemoglobin sensor (nbm-200) and portable hemoglobinometer (hemocue) with an automated hematology analyzer (lh500) in blood donor screening. *Annals of laboratory medicine*, 33(4):261–267, 2013.

[13] Press Releases. Sysmex launches new astrim fit product for noninvasive measurement of estimated hemoglobin levels, retrieved in 2014 from https://www.sysmex.co.jp/en/corporate/news/2014/140115.html.

[14] Robert G Mannino, David R Myers, Erika A Tyburski, Christina Caruso, Jeanne Boudreaux, Traci Leong, GD Clifford, and Wilbur A Lam. Smartphone app for non-invasive detection of anemia using only patient-sourced photos. *Nature communications*, 9, 2018.

[15] Michelle A Visbal-Onufrak, Md Munirul Haque, Martin C Were, Violet Naanyu, Sang Mok Park, Md Hasan, Mhawila A Mhawila, Kit Yee Yeung, Young L Kim, et al. Virtual hyperspectral imaging of eyelids-mhematology for blood hemoglobin analysis. *Mhawila A. and Yeung, Kit Yee and Kim, Young L., Virtual Hyperspectral Imaging of Eyelids-mHematology for Blood Hemoglobin Analysis (April 10, 2019)*, 2019.

[16] JS Rennie and DG MacDonald. Quantitative histological analysis of the epithelium of the ventral surface of hamster tongue in experimental iron deficiency. *Archives of oral Biology*, 27(5):393–397, 1982.

[17] Antonio Montresor, Marco Albonico, Nassor Khalfan, Rebecca J Stoltzfus, James M Tielsch, Hababu M Chwaya, and Lorenzo Savioli. Field trial of a haemoglobin colour scale: an effective tool to detect anaemia in preschool children. *Tropical Medicine & International Health*, 5(2):129–133, 2000.

[18] Kenneth A Walters and Majella E Lane. The human nail: Structure, properties, therapy and grooming. *Cosmetic Formulation: Principles and Practice*, page 77, 2019.

[19] Chia-Wei Sun and Ching-Cheng Chuang. Hemodynamics study based on near-infrared optical assessment. 2012.

[20] AD Edwards, C Richardson, P Van Der Zee, C Elwell, JS Wyatt, M Cope, DT Delpy, and EO Reynolds. Measurement of hemoglobin flow and blood flow by near-infrared spectroscopy. *Journal of Applied Physiology*, 75(4):1884–1889, 1993.

[21] Hailong Qiu, Meiling Tan, Tymish Ohulchanskyy, Jonathan Lovell, and Guanying Chen. Recent progress in upconversion photodynamic therapy. *Nanomaterials*, 8(5):344, 2018.

[22] AVJ Challoner. Photoelectric plethysmography for estimating cutaneous blood flow. *Non-invasive physiological measurements*, 1:125–151, 1979.

[23] Durmus Umutcan Uguz, Boudewijn Venema, Steffen Leonhardt, and Daniel Teichmann. Multifunctional photoplethysmography sensor design for respiratory and cardiovascular diagnosis. In *World Congress on Medical Physics and Biomedical Engineering 2018*, pages 905–909. Springer, 2019.

[24] JV Anderson. The accuracy of pulse oximetry in neonates: effects of fetal hemoglobin and bilirubin. *Journal of perinatology: official journal of the California Perinatal Association*, 7(4):323–323, 1987.

[25] Yitzhak Mendelson. Pulse oximetry: theory and applications for noninvasive monitoring. *Clinical chemistry*, 38(9):1601–1607, 1992.

[26] Toshiyo Tamura, Yuka Maeda, Masaki Sekine, and Masaki Yoshida. Wearable photoplethysmographic sensors—past and present. *Electronics*, 3(2):282–302, 2014.

[27] John Allen. Photoplethysmography and its application in clinical physiological measurement. *Physiological measurement*, 28(3):R1, 2007.

[28] Andrew M Smith, Michael C Mancini, and Shuming Nie. Bioimaging: second window for in vivo imaging. *Nature nanotechnology*, 4(11):710, 2009.

[29] Jia Zheng and Sijung Hu. The preliminary investigation of imaging photoplethysmographic system. In *Journal of Physics: Conference Series*, volume 85, page 012031. IoP Publishing, 2007.

[30] Deric P Jones. Medical electro-optics: measurements in the human microcirculation. *Physics in Technology*, 18(2):79, 1987.

[31] E Gardy and L Drabkin. Determination of the oxygen saturation of blood by a simplified technique applicable to standard equipment. *J Biol Chem*, 227:285, 1957.

[32] Meltem Izzetoglu, Scott C Bunce, Kurtulus Izzetoglu, Banu Onaral, and Kambiz Pourrezaei. Functional brain imaging using near-infrared technology. *IEEE Engineering in Medicine and Biology Magazine*, 26(4):38, 2007.

[33] Rifat Zaman, Chae Ho Cho, Konrad Hartmann-Vaccarezza, Tra Nguyen Phan, Gwonchan Yoon, and Jo Woon Chong. Novel fingertip image-based heart rate detection methods for a smartphone. *Sensors*, 17(2):358, 2017.

[34] Rong-Chao Peng, Xiao-Lin Zhou, Wan-Hua Lin, and Yuan-Ting Zhang. Extraction of heart rate variability from smartphone photoplethysmograms. *Computational and mathematical methods in medicine*, 2015, 2015.

[35] Md Kamrul Hasan, Munirul Haque, Nazmus Sakib, Richard Love, and Sheikh I Ahamed. Smartphone-based human hemoglobin level measurement analyzing pixel intensity of a fingertip video on different color spaces. *Smart Health*, 5:26–39, 2018.

[36] Ferdaus Kawsar, Md Kamrul Hasan, Tanvir Roushan, Sheikh Iqbal Ahamed, William C Chu, and Richard Love. Activity detection using time-delay embedding in multi-modal sensor system. In *International Conference on Smart Homes and Health Telematics*, pages 489–499. Springer, 2016.

[37] Edward Jay Wang, Junyi Zhu, William Li, Rajneil Rana, and Shwetak Patel. Hemaapp ir: noninvasive hemoglobin measurement using unmodified smartphone cameras and built-in leds. In *Proceedings of the 2017 ACM International Joint Conference on Pervasive and Ubiquitous Computing and Proceedings of the 2017 ACM International Symposium on Wearable Computers*, pages 305–308. ACM, 2017.

[38] Boon-Giin Lee and Wan-Young Chung. A smartphone-based driver safety monitoring system using data fusion. *Sensors*, 12(12):17536–17552, 2012.

[39] Anuradha Soni and Sandeep Kumar Jha. Smartphone based non-invasive salivary glucose biosensor. *Analytica chimica acta*, 996:54–63, 2017.

[40] Christopher G Scully, Jinseok Lee, Joseph Meyer, Alexander M Gorbach, Domhnull Granquist-Fraser, Yitzhak Mendelson, and Ki H Chon. Physiological parameter monitoring from optical recordings with a mobile phone. *IEEE Transactions on Biomedical Engineering*, 59(2):303–306, 2012.

[41] MD Anggraeni and A Fatoni. Non-invasive self-care anemia detection during pregnancy using a smartphone camera. In *IOP Conference Series: Materials Science and Engineering*, volume 172, page 012030. IOP Publishing, 2017.

[42] Sarthak Singhal, Prabhat Ralhan, and Nishtha Jatana. Smartphone-based colorimetric detection to measure blood glucose levels. In *Contemporary Computing (IC3), 2015 Eighth International Conference on*, pages 269–274. IEEE, 2015.

[43] Vishnu Dantu, Jagannadh Vempati, and Srinivasan Srivilliputhur. Non-invasive blood glucose monitor based on spectroscopy using a smartphone. In *Engineering in Medicine and Biology Society (EMBC), 2014 36th Annual International Conference of the IEEE*, pages 3695–3698. IEEE, 2014.

[44] Yuanyuan Wu, Anukul Boonloed, Neal Sleszynski, Myra Koesdjojo, Chadd Armstrong, Shay Bracha, and Vincent T Remcho. Clinical chemistry measurements with commercially available test slides on a smartphone platform: Colorimetric determination of glucose and urea. *Clinica Chimica Acta*, 448:133–138, 2015.

[45] Jasmine P Devadhasan, Hyunhee Oh, Cheol Soo Choi, and Sanghyo Kim. Whole blood glucose analysis based on smartphone camera module. *Journal of biomedical optics*, 20(11):117001, 2015.

[46] Vlad Oncescu, Matthew Mancuso, and David Erickson. Cholesterol testing on a smartphone. *Lab on a Chip*, 14(4):759–763, 2014.

[47] Hongying Zhu, Ikbal Sencan, Justin Wong, Stoyan Dimitrov, Derek Tseng, Keita Nagashima, and Aydogan Ozcan. Cost-effective and rapid blood analysis on a cell-phone. *Lab on a Chip*, 13(7):1282–1288, 2013.

[48] Perry Edwards, Chenji Zhang, Baigang Zhang, Xiangqian Hong, Vivek K Nagarajan, Bing Yu, and Zhiwen Liu. Smartphone based optical spectrometer for diffusive reflectance spectroscopic measurement of hemoglobin. *Scientific reports*, 7(1):12224, 2017.

[49] Dong-Sik Kim, Jae-Hoon Choi, Myung-Hyun Nam, Ji-Woon Yang, James Jungho Pak, and Sungkyu Seo. Led and cmos image sensor based hemoglobin concentration measurement technique. *Sensors and Actuators B: Chemical*, 157(1):103–109, 2011.

[50] Ken Ishihara, Kaoru Asano, and Yasunori Maekawa. Apparatus for measuring concentration of hemoglobin and method for the same, March 3 1998. US Patent 5,722,398.

[51] Mark J Rice, Robert H Sweat Jr, James M Rioux, William T Williams, and Wilson Routt. Non-invasive measurement of blood component using retinal imaging, October 23 2001. US Patent 6,305,804.

[52] Arkady S Abdurashitov, Vladislav V Lychagov, Olga A Sindeeva, Oxana V Semyachkina-Glushkovskaya, and Valery V Tuchin. Histogram analysis of laser speckle contrast image for cerebral blood flow monitoring. *Frontiers of Optoelectronics*, 8(2):187–194, 2015.

[53] Larry Kagemann, Alon Harris, Hak Sung Chung, David Evans, Scott Buck, and Bruce Martin. Heidelberg retinal flowmetry: factors affecting blood flow measurement. *British journal of ophthalmology*, 82(2):131–136, 1998.

[54] JH Ma, HS Kim, N-J Rim, S-H Kim, and K-G Cho. Differentiation among glioblastoma multiforme, solitary metastatic tumor, and lymphoma using whole-tumor histogram analysis of the normalized cerebral blood volume in enhancing and perienhancing lesions. *American Journal of Neuroradiology*, 31(9):1699–1706, 2010.

[55] Xiaoqing Yi, Gang Li, and Ling Lin. Noninvasive hemoglobin measurement using dynamic spectrum. *Review of Scientific Instruments*, 88(8):083109, 2017.

[56] Georg Hennig, Christian Homann, Ilknur Teksan, Uwe Hasbargen, Stephan Hasmüller, Lesca M Holdt, Nadia Khaled, Ronald Sroka, Thomas Stauch, Herbert Stepp, et al. Non-invasive detection of iron deficiency by fluorescence measurement of erythrocyte zinc protoporphyrin in the lip. *Nature communications*, 7:10776, 2016.

[57] J Lourdes Albina Nirupa and V Jagadeesh Kumar. Non-invasive measurement of hemoglobin content in blood. In *Medical Measurements and Applications (MeMeA), 2014 IEEE International Symposium on*, pages 1–5. IEEE, 2014.

[58] Haiquan Ding, Qipeng Lu, Hongzhi Gao, and Zhongqi Peng. Non-invasive prediction of hemoglobin levels by principal component and back propagation artificial neural network. *Biomedical optics express*, 5(4):1145–1152, 2014.

[59] Rolf H Bremmer, Annemarie Nadort, Ton G Van Leeuwen, Martin JC Van Gemert, and Maurice CG Aalders. Age estimation of blood stains by hemoglobin derivative determination using reflectance spectroscopy. *Forensic science international*, 206(1-3):166–171, 2011.

[60] U Timm, S Andruschenko, M Hinz, S Koball, G Leen, E Lewis, J Kraitl, and H Ewald. Optical sensor system for continuous non-invasive hemodynamic monitoring in real-time. In *Sensors Applications Symposium (SAS), 2011 IEEE*, pages 167–172. IEEE, 2011.

[61] Rihards Fuksis, Modris Greitans, O Nikisins, and Mihails Pudzs. Infrared imaging system for analysis of blood vessel structure. *Elektronika ir Elektrotechnika*, 97(1):45–48, 2010.

[62] Worapob Pothisarn, Weerapong Chewpraditkul, and Preecha P Yupapin. Noninvasive hemoglobin-measurement-based pulse oximetry. In *Optics in Health Care and Biomedical Optics: Diagnostics and Treatment*, volume 4916, pages 498–505. International Society for Optics and Photonics, 2002.

[63] Ba-Vinh Nguyen, Jean-Louis Vincent, Emmanuel Nowak, Michelle Coat, Nicolas Paleiron, Pierre Gouny, Mehdi Ould-Ahmed, Maité Guillouet, Charles Christian Arvieux, and Gildas Gueret. The accuracy of noninvasive hemoglobin measurement by multiwavelength pulse oximetry after cardiac surgery. *Anesthesia & Analgesia*, 113(5):1052–1057, 2011.

[64] Ulrich Timm, Helge Gewiss, Jens Kraitl, Kirstin Stuepmann, Michael Hinz, Sebastian Koball, and Hartmut Ewald. Novel multi wavelength sensor concept to detect total hemoglobin concentration, methemoglobin and oxygen saturation. In *SPIE BiOS*, pages 93320J–93320J. International Society for Optics and Photonics, 2015.

[65] Edward J Wang, William Li, Junyi Zhu, Rajneil Rana, and Shwetak N Patel. Noninvasive hemoglobin measurement using unmodified smartphone camera and white flash. In *Engineering in Medicine and Biology Society (EMBC), 2017*

39th Annual International Conference of the IEEE, pages 2333–2336. IEEE, 2017.

[66] Raditya Artha Rochmanto, Hasballah Zakaria, Ratih Devi Alviana, and Nurhalim Shahib. Non-invasive hemoglobin measurement for anemia diagnosis. In *Electrical Engineering, Computer Science and Informatics (EECSI), 2017 4th International Conference on*, pages 1–5. IEEE, 2017.

[67] Brinda Desai and Uttam Chaskar. Comparison of optical sensors for non-invasive hemoglobin measurement. In *Electrical, Electronics, and Optimization Techniques (ICEEOT), International Conference on*, pages 2211–2214. IEEE, 2016.

[68] Jens Kraitl, Ulrich Timm, Hartmut Ewald, and Elfed Lewis. Non-invasive sensor for an in vivo hemoglobin measurement. In *Sensors, 2011 IEEE*, pages 276–279. IEEE, 2011.

[69] Cmos sensor. retrieved in July 27, 2018 from https://whatis.techtarget.com/definition/CMOS-sensor.

[70] Dainis Jakovels and Janis Spigulis. Rgb imaging device for mapping and monitoring of hemoglobin distributionin skin. *Lithuanian Journal of Physics*, 52(1), 2012.

[71] Charge-coupled device (ccd). retrieved in July 27, 2018 from https://searchstorage.techtarget.com/definition/charge-coupled-device.

[72] Indium gallium arsenide. retrieved in July 27, 2018 from https://en.wikipedia.org/wiki/Indium_gallium_arsenide.

[73] Kye-jin Jeon and Gil-won Yoon. Method and apparatus for noninvasively monitoring hemoglobin concentration and oxygen saturation, March 30 2004. US Patent 6,714,805.

[74] K Ashoka Reddy, Boby George, and V Jagadeesh Kumar. Use of fourier series analysis for motion artifact reduction and data compression of photoplethysmographic signals. *IEEE Transactions on Instrumentation and Measurement*, 58(5):1706–1711, 2009.

[75] Ronald W Schafer. What is a savitzky-golay filter?[lecture notes]. *IEEE Signal processing magazine*, 28(4):111–117, 2011.

[76] Randall D Tobias et al. An introduction to partial least squares regression. In *Proceedings of the twentieth annual SAS users group international conference*, pages 1250–1257. SAS Institute Inc Cary, 1995.

[77] Debasish Basak, Srimanta Pal, and Dipak Chandra Patranabis. Support vector regression. *Neural Information Processing-Letters and Reviews*, 11(10):203–224, 2007.

[78] Mavuto M Mukaka. A guide to appropriate use of correlation coefficient in medical research. *Malawi Medical Journal*, 24(3):69–71, 2012.

[79] Davide Giavarina. Understanding bland altman analysis. *Biochemia medica: Biochemia medica*, 25(2):141–151, 2015.

[80] Mohammad Adibuzzaman. Computational approaches for monitoring of health parameters and their evaluation for application in clinical setting. 2015.

[81] Carole Tournier, Marine Devezeaux de Lavergne, Fred van de Velde, Markus Stieger, Christian Salles, and Dominique Bertrand. Investigation of oral gels breakdown using image analysis. *Food Hydrocolloids*, 63:67–76, 2017.

[82] Ishan Barman, Chae-Ryon Kong, Gajendra P Singh, and Ramachandra R Dasari. Effect of photobleaching on calibration model development in biological raman spectroscopy. *Journal of biomedical optics*, 16(1):011004, 2011.

[83] Anne-Laure Boulesteix and Korbinian Strimmer. Partial least squares: a versatile tool for the analysis of high-dimensional genomic data. *Briefings in bioinformatics*, 8(1):32–44, 2006.

[84] Susmita Datta. Exploring relationships in gene expressions: a partial least squares approach. *Gene expression*, 9(6):249–255, 2001.

[85] LP Bras and JC Menezes. Dealing with gene expression missing data. *IEE Proceedings-Systems Biology*, 153(3):105–119, 2006.

[86] Monica Clementi, Sergio Clementi, Gabriele Cruciani, Manuel Pastor, Andrew M Davis, and Darren R Flower. Robust multivariate statistics and the prediction of protein secondary structure content. *Protein engineering*, 10(7):747–749, 1997.

[87] Titin Agustin Nengsih, Frédéric Bertrand, Myriam Maumy-Bertrand, and Nicolas Meyer. Determining the number of components in pls regression on incomplete data. *arXiv preprint arXiv:1810.08104*, 2018.

[88] Susanne Wiklund, David Nilsson, Lennart Eriksson, Michael Sjöström, Svante Wold, and Klaas Faber. A randomization test for pls component selection. *Journal of Chemometrics: A Journal of the Chemometrics Society*, 21(10-11):427–439, 2007.

[89] John W McMurdy, Gregory D Jay, Selim Suner, Flor Trespalacios, and Gregory P Crawford. Diffuse reflectance spectra of the palpebral conjunctiva and its utility as a noninvasive indicator of total hemoglobin. *Journal of biomedical optics*, 11(1):014019, 2006.

[90] V Rajinikanth and MS Couceiro. Rgb histogram based color image segmentation using firefly algorithm. *Procedia Computer Science*, 46:1449–1457, 2015.

[91] E Jonathan and Martin Leahy. Investigating a smartphone imaging unit for photoplethysmography. *Physiological measurement*, 31(11):N79, 2010.

[92] Enock Jonathan and Martin J Leahy. Cellular phone-based photoplethysmographic imaging. *Journal of biophotonics*, 4(5):293–296, 2011.

[93] Sarah Ali Siddiqui, Yuan Zhang, Zhiquan Feng, and Anton Kos. A pulse rate estimation algorithm using ppg and smartphone camera. *Journal of medical systems*, 40(5):126, 2016.

[94] Zhilin Zhang et al. Photoplethysmography-based heart rate monitoring in physical activities via joint sparse spectrum reconstruction. *IEEE Trans. Biomed. Engineering*, 62(8):1902–1910, 2015.

[95] Sandrine C Millasseau, James M Ritter, Kenji Takazawa, and Philip J Chowienczyk. Contour analysis of the photoplethysmographic pulse measured at the finger. *Journal of hypertension*, 24(8):1449–1456, 2006.

[96] Yunyoung Nam and Yun-Cheol Nam. Photoplethysmography signal analysis for optimal region-of-interest determination in video imaging on a built-in smartphone under different conditions. *Sensors*, 17(10):2385, 2017.

[97] M Rendell, E Anderson, W Schlueter, J Mailliard, D Honigs, and R Rosenthal. Determination of hemoglobin levels in the finger using near infrared spectroscopy. *Clinical & Laboratory Haematology*, 25(2):93–97, 2003.

[98] Daniel Yim, Gladimir VG Baranoski, BW Kimmel, Tenn F Chen, and Erik Miranda. A cell-based light interaction model for human blood. In *Computer Graphics Forum*, volume 31, pages 845–854. Wiley Online Library, 2012.

[99] Yitzhak Mendelson, Robert A Peura, and Hannu Harjunmaa. Method and apparatus for monitoring blood analytes noninvasively by pulsatile photoplethysmography, August 11 1992. US Patent 5,137,023.

[100] Sun Kook Yoo. Photoplethysmography (ppg) device and the method thereof, February 26 2008. US Patent 7,336,982.

[101] A Reşit Kavsaoğlu, Kemal Polat, and M Hariharan. Non-invasive prediction of hemoglobin level using machine learning techniques with the ppg signal's characteristics features. *Applied Soft Computing*, 37:983–991, 2015.

[102] Dainis Jakovels, Uldis Rubins, and Janis Spigulis. Lasca and ppg imaging for non-contact assessment of skin blood supply. In *Medical Imaging 2013: Physics of Medical Imaging*, volume 8668, page 866849. International Society for Optics and Photonics, 2013.

[103] Bethany R Knorr-Chung, Susan P McGrath, and George T Blike. Identifying airway obstructions using photoplethysmography (ppg). *Journal of clinical monitoring and computing*, 22(2):95–101, 2008.

[104] Swathi Ramasahayam, Sri Haindavi Koppuravuri, Lavanya Arora, and Shubhajit Roy Chowdhury. Noninvasive blood glucose sensing using near infra-red spectroscopy and artificial neural networks based on inverse delayed function model of neuron. *Journal of medical systems*, 39(1):166, 2015.

[105] Kevin Knight, Sally Wade, and Lodovico Balducci. Prevalence and outcomes of anemia in cancer: a systematic review of the literature. *The American journal of medicine*, 116(7):11–26, 2004.

[106] Rosario Gonzalez-Casas, E Anthony Jones, and Ricardo Moreno-Otero. Spectrum of anemia associated with chronic liver disease. *World journal of gastroenterology: WJG*, 15(37):4653, 2009.

[107] James M Otto, James OM Plumb, Eleri Clissold, Shriya B Kumar, Denis J Wakeham, Walter Schmidt, Michael PW Grocott, Toby Richards, and Hugh E Montgomery. Hemoglobin concentration, total hemoglobin mass and plasma volume in patients: implications for anemia. *haematologica*, 102(9):1477–1485, 2017.

[108] Hemoglobin and its measurement. retrieved in April 20, 2019 from https://acutecaretesting.org/en/articles/hemoglobin-and-its-measurement.

[109] Marleen Keijzer, Steven L Jacques, Scott A Prahl, and Ashley J Welch. Light distributions in artery tissue: Monte carlo simulations for finite-diameter laser beams. *Lasers in surgery and medicine*, 9(2):148–154, 1989.

[110] Lisa Carroll and Tatyana R Humphreys. Laser-tissue interactions. *Clinics in dermatology*, 24(1):2–7, 2006.

[111] Joshua D Shackman. The use of partial least squares path modeling and generalized structured component analysis in international business research: A literature review. *International Journal of Management*, 30(3):78–86, 2013.

[112] Mikko Rönkkö, Cameron N McIntosh, John Antonakis, and Jeffrey R Edwards. Partial least squares path modeling: Time for some serious second thoughts. *Journal of Operations Management*, 47:9–27, 2016.

[113] Chenhao Cui and Tom Fearn. Comparison of partial least squares regression, least squares support vector machines, and gaussian process regression for a near infrared calibration. *Journal of Near Infrared Spectroscopy*, 25(1):5–14, 2017.

[114] Mariette Awad and Rahul Khanna. Support vector regression. In *Efficient Learning Machines*, pages 67–80. Springer, 2015.

[115] D Th Ubbink. Toe blood pressure measurements in patients suspected of leg ischaemia: a new laser doppler device compared with photoplethysmography. *European journal of vascular and endovascular surgery*, 27(6):629–634, 2004.

[116] Christian Butter, Christoph Stellbrink, Andres Belalcazar, Don Villalta, Michael Schlegl, Anil Sinha, Francisca Cuesta, and Craig Reister. Cardiac resynchronization therapy optimization by finger plethysmography. *Heart Rhythm*, 1(5):568–575, 2004.

[117] Elmo Mannarino, Leonella Pasqualini, Marina Menna, Giorgio Maragoni, and Ugo Orlandi. Effects of physical training on peripheral vascular disease: a controlled study. *Angiology*, 40(1):5–10, 1989.

[118] ML Evans and LA Geddes. An assessment of blood vessel vasoactivity using photoplethysmography. *Medical instrumentation*, 22(1):29–32, 1988.

[119] Diana Rimaud, Christian Boissier, and Paul Calmels. Evaluation of the effects of compression stockings using venous plethysmography in persons with spinal cord injury. *The journal of spinal cord medicine*, 31(2):202–207, 2008.

[120] Mohamed Elgendi. On the analysis of fingertip photoplethysmogram signals. *Current cardiology reviews*, 8(1):14–25, 2012.

[121] Daniel McDuff, Sarah Gontarek, and Rosalind W Picard. Remote detection of photoplethysmographic systolic and diastolic peaks using a digital camera. *IEEE Transactions on Biomedical Engineering*, 61(12):2948–2954, 2014.

[122] Sanjeev Nara, Manvinder Kaur, and Kundan Lal Verma. Novel notch detection algorithm for detection of dicrotic notch in ppg signals. *International Journal of Computer Applications*, 86(17):36–39, 2014.

[123] Sobhan Salari Shahrbabaki, Beena Ahmed, Thomas Penzel, and Dean Cvetkovic. Photoplethysmography derivatives and pulse transit time in overnight blood pressure monitoring. In *2016 38th Annual International Conference of the IEEE Engineering in Medicine and Biology Society (EMBC)*, pages 2855–2858. IEEE, 2016.

[124] CP Chua and C Heneghan. Continuous blood pressure monitoring using ecg and finger photoplethysmogram. In *2006 International Conference of the IEEE Engineering in Medicine and Biology Society*, pages 5117–5120. IEEE, 2006.

[125] L Delle Chiaie, G Buck, D Grab, and R Terinde. Prediction of fetal anemia with doppler measurement of the middle cerebral artery peak systolic velocity in pregnancies complicated by maternal blood group alloimmunization or parvovirus b19 infection. *Ultrasound in Obstetrics and Gynecology*, 18(3):232–236, 2001.

[126] Thomas K Aldrich. Non-invasive blood component analyzer, September 2 2003. US Patent 6,615,064.

[127] David A Benaron, William E Benitz, Ronald L Ariagno, and David K Stevenson. Noninvasive methods for estimating in vivo oxygenation. *Clinical pediatrics*, 31(5):258–273, 1992.

[128] Ronald J Flower, Robert W Olsen, Michael A Van Ells, and Ralph Flatau. Apparatus and method for measuring blood constituents, September 5 1989. US Patent 4,863,265.

[129] Kenneth Humphreys, Charles Markham, and Tomás E Ward. A cmos camera-based system for clinical photoplethysmographic applications. In *Opto-Ireland 2005: Imaging and Vision*, volume 5823, pages 88–96. International Society for Optics and Photonics, 2005.

[130] Y Tardy, JJ Meister, F Perret, HR Brunner, and M Arditi. Non-invasive estimate of the mechanical properties of peripheral arteries from ultrasonic and photoplethysmographic measurements. *Clinical Physics and Physiological Measurement*, 12(1):39, 1991.

[131] Chungkeun Lee, Hang Sik Shin, and Myoungho Lee. Relations between ac-dc components and optical path length in photoplethysmography. *Journal of biomedical optics*, 16(7):077012, 2011.

[132] CCY Poon, XF Teng, YM Wong, C Zhang, and YT Zhang. Changes in the photoplethysmogram waveform after exercise. In *2004 2nd IEEE/EMBS International Summer School on Medical Devices and Biosensors*, pages 115–118. IEEE, 2004.

[133] Wei Zhang, Su-Yan Tang, Yi-Fan Zhu, and Wei-Ping Wang. Comparative studies of support vector regression between reproducing kernel and gaussian kernel. *World Academy of Science, Engineering and Technology*, 65:933–941, 2010.

[134] Wei Tang, Qiang Chen, Wenjuan Yan, Guoquan He, and Ling Lin. Express: An optimizing dynamic spectrum differential extraction method for noninvasive blood component analysis. *Applied spectroscopy*, page 0003702818815508, 2018.

[135] Gang LI, Chan XIONG, Ling LIN, Bao-ju ZHANG, Ying TONG, et al. Single-trial estimation of dynamic spectrum. *Spectroscopy and Spectral Analysis*, 31(7):1857–1861, 2011.

[136] Gang Li, Sijia Xu, Mei Zhou, Qirui Zhang, and Ling Lin. Noninvasive hemoglobin measurement based on optimizing dynamic spectrum method. *Spectroscopy Letters*, 50(3):164–170, 2017.

[137] Ximeng Feng, Gang Li, Haixia Yu, Shaohui Wang, Xiaoqing Yi, and Ling Lin. Wavelength selection for portable noninvasive blood component measurement system based on spectral difference coefficient and dynamic spectrum.

Spectrochimica Acta Part A: Molecular and Biomolecular Spectroscopy, 193:40–46, 2018.

[138] Serge Bobbia, Richard Macwan, Yannick Benezeth, Alamin Mansouri, and Julien Dubois. Unsupervised skin tissue segmentation for remote photoplethysmography. *Pattern Recognition Letters*, 2017.

[139] Ralph WCGR Wijshoff, Massimo Mischi, and Ronald M Aarts. Reduction of periodic motion artifacts in photoplethysmography. *IEEE Transactions on Biomedical Engineering*, 64(1):196–207, 2017.

[140] M Raghu Ram, K Venu Madhav, E Hari Krishna, Nagarjuna Reddy Komalla, and K Ashoka Reddy. A novel approach for motion artifact reduction in ppg signals based on as-lms adaptive filter. *IEEE Transactions on Instrumentation and Measurement*, 61(5):1445–1457, 2012.

[141] KW Chan and YT Zhang. Adaptive reduction of motion artifact from photoplethysmographic recordings using a variable step-size lms filter. In *SENSORS, 2002 IEEE*, volume 2, pages 1343–1346. IEEE, 2002.

[142] M Raghuram, K Venu Madhav, E Hari Krishna, Nagarjuna Reddy Komalla, Kosaraju Sivani, and K Ashoka Reddy. Dual-tree complex wavelet transform for motion artifact reduction of ppg signals. In *2012 IEEE international symposium on medical measurements and applications proceedings*, pages 1–4. IEEE, 2012.

[143] Babak Taati, Shun Zhao, Ahmed B Ashraf, Azin Asgarian, M Erin Browne, Kenneth M Prkachin, Alex Mihailidis, and Thomas Hadjistavropoulos. Algorithmic bias in clinical populations–evaluating and improving facial analysis technology in older adults with dementia. *IEEE Access*, 2019.

[144] E Leppänen. Experimental basis of standardized specimen collection: the effect of the site of venipuncture on the blood picture, the white blood cell differential count, and the serum albumin concentration. *European journal of haematology*, 41(5):445–448, 1988.

[145] DG Ross, AC Gilfillan, DE Houston, and WAL Heaton. Evaluation of hemoglobin screening methods in prospective blood donors. *Vox sanguinis*, 50(2):78–80, 1986.

[146] Z-W Yang, S-H Yang, L Chen, J Qu, J Zhu, and Z Tang. Comparison of blood counts in venous, fingertip and arterial blood and their measurement variation. *Clinical & Laboratory Haematology*, 23(3):155–159, 2001.

[147] Hartmut Radtke, Gülnur Polat, Ulrich Kalus, Abdulgabar Salama, and Holger Kiesewetter. Hemoglobin screening in prospective blood donors: comparison of different blood samples and different quantitative methods. *Transfusion and Apheresis Science*, 33(1):31–35, 2005.

[148] E Schalk, MU Heim, M Koenigsmann, and K Jentsch-Ullrich. Use of capillary blood count parameters in adults. *Vox sanguinis*, 93(4):348–353, 2007.

[149] Rajendra Chaudhary, Anju Dubey, and Atul Sonker. Techniques used for the screening of hemoglobin levels in blood donors: current insights and future directions. *Journal of blood medicine*, 8:75, 2017.

[150] Peter Mell, Tim Grance, et al. The nist definition of cloud computing. 2011.

[151] Milos Stojmenovic. Mobile cloud computing for biometric applications. In *2012 15th International Conference on Network-Based Information Systems*, pages 654–659. IEEE, 2012.

[152] Veeru Talreja, Terry Ferrett, Matthew C Valenti, and Arun Ross. Biometrics-as-a-service: A framework to promote innovative biometric recognition in the cloud. In *2018 IEEE International Conference on Consumer Electronics (ICCE)*, pages 1–6. IEEE, 2018.